Two-photon processes in highly charged ions

Dipl.-Phys. Thorsten Jahrsetz

Dissertation

submitted to the

Combined Faculties of the Natural Sciences and Mathematics

of the Ruperto-Carola-University of Heidelberg, Germany

for the degree of

Doctor of Natural Sciences

Put forward by

Dipl. Phys. Thorsten Jahrsetz

born in: Leimen, Germany

Oral examination: 5.03.2015

Two-photon processes in highly charged ions

Reviewers:

Priv.-Doz. Dr. Andrey Surzhykov
Priv.-Doz. Dr. Zoltán Harman

Abstract

Two-photon processes are atomic processes in which an atom interacts simultaneously with two photons. Such processes describe a wide range of phenomena, such as two-photon decay and elastic or inelastic scattering of photons. In recent years two-photon processes involving highly charged heavy ions have become an active area of research. Such studies do not only consider the total transition or scattering rates but also their angular and polarization dependence. To support such examinations in this thesis I present a theoretical framework to describe these properties in all two-photon processes with bound initial and final states and involving heavy H-like or He-like ions. I demonstrate how this framework can be used in some detailed studies of different two-photon processes. Specifically a detailed analysis of two-photon decay of H-like and He-like ions in strong external electromagnetic fields shows the importance of considering the effect of such fields for the physics of such systems. Furthermore I studied the elastic Rayleigh as well as inelastic Raman scattering by heavy H-like ions. I found a number of previously unobserved phenomena in the angular and polarization dependence of the scattering cross-sections that do not only allow to study interesting details of the electronic structure of the ion but might also be useful for the measurement of weak physical effects in such systems.

Zusammenfassung

Zweiphotonprozesse sind atomare Prozesse, in denen ein Atom gleichzeitig mit zwei Photonen wechselwirkt. Solche Prozesse beschreiben eine Vielzahl an Phänomenen, wie z.B. den Zweiphotonenzerfall und elastische oder inelastische Photonenstreuung. In den letzten Jahren sind Zweiphotonprozesse in hochgeladenen Ionen ein aktives Forschungsgebiet geworden. Neue Studien beschäftigen sich nicht nur mit den Absolutwerten der Übergangsraten oder Wirkungsquerschnitten, sondern auch mit ihrer Winkel- und Polarisationsabgängigkeit. Um derartige Studien zu unterstützen, stelle ich in dieser Dissertation ein Verfahren vor, mit dem solche Eigenschaften für alle Zweiphotonenprozesse mit gebundenen Anfangs- und Endzuständen in schweren wasserstoff- und heliumähnlichen Ionen berechnet werden können. Es wird dargestellt, wie dieses Verfahren für detaillierte Studien verschiedener Zweiphotonenprozesse angewandt werden kann. Insbesondere wurde eine Analyse von dem Zweiphotonzerfall angeregter Ionen in starken elektrischen Feldern durchgeführt, bei der sich die Bedeutung solcher Felder in diesen Systemen zeigte. Neben diesen Zweiphotonenstudien untersuchte elastischer Rayleigh und inelastischer Raman Streuung an schweren wasserstoffähnlichen Ionen. Dabei wurden eine Reihe neuer Phänomene beobachtet, die einen tiefen Einblick in die elektronische Struktur von schweren Ionen ermöglichen und eventuell Anwendung in der Messung schwacher physikalischer Effekte finden könnten.

Publications

As part of my PhD studies I contributed to the following publications:

- T. Jahrsetz and A. Surzhykov, "Two-photon transitions in few-electron ions in the presence of static electric fields ", Phys. Scr. T156, 014069 (2013)
- A. Surzhykov, V. A. Yerokhin, T. Jahrsetz, P. Amaro, Th. Stöhlker, and S. Fritzsche, "Polarization correlations in the elastic Rayleigh scattering of photons by hydrogenlike ions", Phys. Rev. A 88, 062515 (2013)
- T. Jahrsetz, S. Fritzsche, and A. Surzhykov, "Inelastic Raman scattering of light by hydrogenlike ions", Phys. Rev. A 89, 042501 (2014)

Contents

1 Introduction

Since the beginning of quantum physics the study of atoms and ions has been of central importance for this field. Analyzing radiative transitions or the scattering of light and electrons by atoms and ions has given vital impulses for the development of non-relativistic and relativistic quantum mechanics and even, through the Lamb shift, for the development of quantum field theory. While in the early- and mid-20th century these efforts were mostly focused on light neutral ions, in the last decades new experimental techniques such as EBITs and heavy ion storage rings, e.g. at the GSI in Darmstadt, made it possible to perform experiments with highly charged heavy ions. In such systems a number of relativistic, higher multipole, quantum electrodynamic and even parity non-conservation effects are enhanced and can be studied in detail e.g. [1, 2, 3].

One of the areas of heavy ion research of particular interest are radiative processes involving two photons, the so-called two-photon processes. These two-photon processes consist of very diverse phenomena, like the internal transition of an ion by simultaneous absorption or emission of two-photons and elastic and inelastic photon scattering. All of these processes have in common that they can be theoretically described by means of second-order perturbation theory. In this thesis I consider such processes in which the electrons of the ions are in a bound states both before and after the interaction with the photons. A schematic description of most of these processes is shown in Fig. 1.1. In the figure we have on the one hand two-photon transitions (top row), on the other hand photon scattering processes (bottom row). For such bound two-photon processes in hydrogen-like (H-like) and helium-like (He-like) ions a common fully relativistic theoretical model was developed. This model allows a precise description not only of total cross-sections and transition rates, but also an analysis of their dependence on the angles and polarizations of the participating photons. The fully relativistic approach makes it possible to perform advanced studies on different two-photon processes in highly charged ions with a special emphasis on relativistic and higher multipole effects. I used this method to examine a number of specific phenomena in different two-photon processes in detail.

In order to develop the physics concepts for such an approach, the basic ideas of a relativistic description of H-like ions by means of the Dirac equation are introduced in chapter 2. Using a so-called independent particle model (IPM) these results can also be utilized to characterize heavy He-like ions.
Next in chapter 3, the interaction of the bound electrons with external electromagnetic fields is discussed using a perturbative approach. With this approach the absorption and emission of photons by bound electrons are described by means of time-dependent perturbation theory. The two-photon processes arise as second-order effects. The properties of two-photon processes, transition rates (for two-photon decay) and cross-sections (for photon scattering and enhanced two-photon decay) can be traced back second-order transition or scattering amplitudes. Additionally, in chapter 3 the effects of static electric fields on the states of the

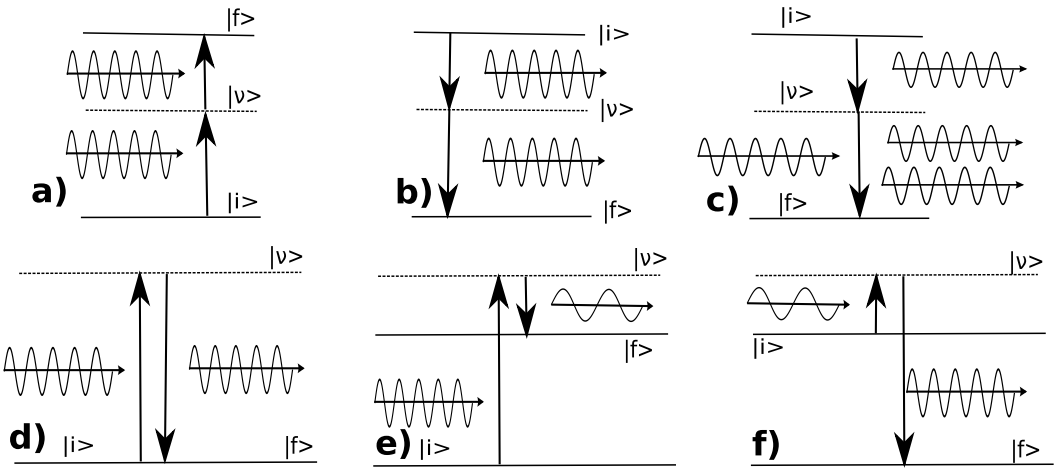

Fig. 1.1: Schematic description of different two-photon processes with a bound initial state $|i\rangle$ and a final state $|f\rangle$ via a so-called virtual intermediate state $|\nu\rangle$. The Graph shows two-photon absorption (a), two-photon emission (b), so-called enhanced two-photon emission in which one of the photons is emitted in an induced transition process (c), elastic Rayleigh scattering (d), and Stokes (e) as well as anti-Stokes (f) Raman scattering.

ion are briefly examined using the non-degenerate time-independent perturbation theory. To be able to analyze different two-photon processes in detail, a framework for the evaluation of the non-trivial two-photon transition or scattering amplitude is presented in chapter 4. For this thesis a well-known approach [4, 5, 6] is used in which the angular dependent parts of the amplitude are separated from the radial integrations by means of the Wigner-Eckart theorem. With this method it is possible to trace the complex radial integrations that appear in the evaluation of the transition or scattering amplitudes of all two-photon processes back to the so-called reduced matrix elements of the two-photon absorption process. In the second part of chapter 4, I present in detail an analytic approach to evaluate such reduced matrix elements based on the Sturmian representation of the Dirac-Coulomb Greens function. Furthermore, the limitations of such a procedure and some methods to overcome these limitations are briefly discussed.

In the following two chapters I show how the theoretical methods developed in chapter 3 and 4 can be applied in the description of various two-photon processes by discussing the original research on specific phenomena in different two-photon processes I worked on during my PhD studies. First, in chapter 5, the influence of external electric fields on two-photon transitions (Graph a,b,c in Fig. 1.1) is examined. In the absence of such fields these transitions, in which two-photons are simultaneously emitted or absorbed, have been actively studied for many years both in theory [4, 7, 8, 9] as well as in experiment, e.g. [10]. In recent years two-photon decay in highly charged heavy ion ions has sparked a lot of interest as a tool to study, relativistic, higher multipole, or even parity non-conservation effects [3, 4, 9, 10, 11]. For such measurements a high level of control over the two-photon process would be of great benefit. One method to influence two-photon transitions is the use of external electric fields. For the measurement of parity non-conservation effects, it was e.g. proposed [3, 11] to utilize strong polarized lasers in the optical regime to measure the weak coupling of electrons and the nucleus in He-like Uranium. Prior to my research it was

not clear how the electric fields of such (low frequency) lasers would influence two-photon processes. To examine this question, I present in the first part of chapter 5, as an extension of the research I performed for my diploma thesis [12], a detailed analysis on the influence of static external electric fields on the two-photon decay (Graph b in Fig. 1.1) of excited H-like and He-like ions. Apart from exploring the side effects of such fields that determine the feasibility of laser-based experimental schemes like in [3], this study allows to gain some general information how two-photon processes are influenced by external perturbations of the system.
Additional to such static fields, I briefly explore the effect of dynamic fields on the two-photon decay. In such fields an exotic two-photon decay process appears, in which one of the emitted photons is stimulated by the external field, c.p. Graph c in Fig. 1.1. This so-called singly stimulated or enhanced two-photon decay has previously been studied only in (light) neutral atoms e.g. [13, 14]. In the second half of the chapter I analyze the behavior of this process and examine the possibility of measuring such an effect in heavier H-like ions.

On top of these examinations of two-photon decay processes in chapter 6 the elastic (Graph d in Fig. 1.1) and inelastic scattering (Graph e,f in Fig. 1.1) of photons by H-like ions is studied. In the first part of chapter 6 I present new results from a research project on polarization effects in elastic scattering by H-like ions. Such so-called Rayleigh scattering processes were studied extensively, but mostly for neutral targets [15, 16, 17, 18, 19, 20]. In these studies the energy dependence of the total cross-section and the angular distribution of the scattered photons was examined for a wide range of targets. Furthermore, the polarization dependence of the cross-section for elastic scattering by neutral hydrogen [21] was also analyzed. For the scattering of x-ray photons on highly charged ions, however, no satisfying polarization sensitive study was performed. My collaborators and me closed this gap with our analysis and examined the role of higher multipoles and relativistic effects on such elastic scattering in detail. It is shown how a selection of specific scattering conditions can be used to enhance the visibility of small physical effects by suppressing the leading order contributions.

In the second part of chapter 6 I consider inelastic scattering of photons by H-like ions accompanied by an excitation of the target, c.p. Graph e in Fig. 1.1. Such so-called (Stokes) Raman scattering has been extensively studied for a number of targets, such as solid-state systems or molecules. In the context of atomic physics this inelastic process was mostly examined on light neutral atoms and optical to mid-UV photons [14, 22, 23, 24, 25, 26]. Furthermore, in recent years experiments on heavy neutral atoms have been performed. In the experiments x-rays with energies close to the ionization energy of one of the electrons of the atom are used to measure so-called Resonant Raman scattering [27, 28]. However, the scattering of lower energy x-rays by heavy few-electron ions so far has been only preliminarily studied [29]. In my research I performed a more thorough examination by analyzing the energy- and Z-dependence of total and angular-differential cross-sections of inelastic Raman scattering by H-like ions, as well as the state of the ions after the inelastic scattering. Special attention is payed to the role of relativistic and higher multipole effects that appear in scattering by high-Z ions.

In the last chapter, I recapitulate and shortly discuss the results of these studies on the two-photon processes. A few additional ideas for further research on two-photon processes are mentioned as well.

Unit system and notation Unless otherwise stated, all formulas in this thesis use the so-called "relativistic" or "natural" unit system: $c = m_e = \hbar = 1$, i.e. the speed of light, the mass of the electron and the reduced Plank constant are set to 1.
In this unit system length is given in units of the reduced Compton wave length $\frac{\lambda_c}{2\pi} = \frac{\hbar}{m_e c}$. The time unit is connected to this length unit by the speed of light and given in units of $\frac{\lambda_c}{2\pi c}$. The energy is given in units of the rest mass of the electron $m_e c^2$.
Finally it is important to know the unit of charge in this system. It is given by $e/\sqrt{\alpha_S} = \sqrt{4\pi\epsilon_0\hbar c}$, where e is the elementary charge, ϵ_0 the electric field constant and $\alpha_S = \frac{e^2}{4\pi\epsilon_0\hbar c} \approx \frac{1}{137}$ the well-known Sommerfeld fine structure constant. To avoid confusion of this fine structure constant with the Dirac matrices a notation with the subscript S is introduced.

Furthermore, it is important to note that vectors are written as bold letters, e.g. $\mathbf{a}$. The related regular letters represent the length of vector, e.g. $a = \sqrt{\mathbf{a} \cdot \mathbf{a}}$, and the direction of the vector is described by the set of angles, e.g. Ω_a.

2 Heavy few-electron ions in relativistic Dirac theory

The description of atoms and ions is one of the most successful application of quantum theory. While non-relativistic theories are sufficient as first step, especially for light ions (c.p. [30]), a more detailed analysis reveals the importance of a fully relativistic description [31]. In such a description a number of specific relativistic effects appear, e.g. there is a fine structure in the spectrum of the bound energy levels. These effects become very prominent in heavy atoms and especially in highly charged heavy ions and such systems, must thus be described by means of a relativistic theory. In order to describe this kind of few-electron ions, I here recapitulate relativistic quantum theory based on of the Dirac equation. Within this theory I present analytic solutions for the bound states of H-like ions with an infinitely heavy nucleus. Finally, these one-electron solutions are used to construct good approximations of the states of He-like high-Z ions by means of an independent particle model.

2.1 The Dirac equation

In a relativistic quantum theory the equation of motion can only contain operators in which derivations with respect to space and time appear in the same order. Apart from the second order Klein-Gordon equation, which describes the propagation of particles without an intrinsic angular momentum or spin, for spin-$1/2$ fermions there exists a relativistic theory linear both in space- and time-derivations, the so-called Dirac equation [32]:

$$i\partial_t\psi(\mathbf{r},t) = \left(m_0\beta + \boldsymbol{\alpha}(\mathbf{p} - q\mathbf{A}) + q\Phi\right)\psi(\mathbf{r},t). \tag{2.1}$$

Here m_0 is the mass of the fermion, q its charge, and we have an electromagnetic field with the scaler potential Φ and the vector potential $\mathbf{A}$. Furthermore, the relativistic momentum operator is given by $\mathbf{p} = -i\boldsymbol{\alpha}\nabla$ and the 4x4 dimensional Dirac matrices $\beta = \begin{pmatrix} 1 & 0 \\ 0 & -1 \end{pmatrix}$ and $\boldsymbol{\alpha} = \begin{pmatrix} 0 & \boldsymbol{\sigma} \\ \boldsymbol{\sigma} & 0 \end{pmatrix}$ are introduced. In this definition $\boldsymbol{\sigma} = (\sigma_x, \sigma_y, \sigma_z)$ is a vector of Pauli matrices and the 1 are 2x2-unit matrices.
In the Dirac theory the states $\psi(\mathbf{r},t)$ of the system are not one-dimensional objects but four-dimensional sets of wavefunctions, the so-called spinors:

$$\psi(\mathbf{r},t) = \begin{pmatrix} \psi_1(\mathbf{r},t) \\ \psi_2(\mathbf{r},t) \\ \psi_3(\mathbf{r},t) \\ \psi_4(\mathbf{r},t) \end{pmatrix}. \tag{2.2}$$

On top of a spacial probability distribution these spinors automatically contain information on the intrinsic angular momentum or spin of spin-$1/2$ fermions, like electrons. It is common to split the 4-dimensional spinor (2.2) into two two-dimensional two-component spinors, e.g. $F(\mathbf{r},t), G(\mathbf{r},t)$:

$$\psi(\mathbf{r},t) = \begin{pmatrix} F(\mathbf{r},t) \\ G(\mathbf{r},t) \end{pmatrix}. \tag{2.3}$$

In most systems, e.g. systems with positive eigenenergies, the F two-component spinor has a larger absolute value than the G two-component spinor. For that reason $F(\mathbf{r},t)$ is often called the large part and $G(\mathbf{r},t)$ the small part of the spinor. The relative size of $G(\mathbf{r},t)$ is a good measure of the role of relativistic effects for the system. In the non-relativistic limit it usually vanishes.

The combination of operators on the right side of Eq. (2.1) are usually called the Hamilton operator H of the system. Such Hamilton operators contain all important information to describe a quantum-system.
If the Hamilton operator of a system is not explicitly time-dependent, determining the solution of the Dirac equation (2.1) can be greatly simplified. For such a system the spinor is split into a trivial time-dependent part and a time-independent part.

$$\psi(\mathbf{r},t) = \psi(\mathbf{r}) \cdot e^{-iEt}, \tag{2.4}$$

with E the energy eigenstate of the system. The time-independent part satisfies the so-called time-independent Dirac equation

$$E\psi(\mathbf{r}) = H\psi(\mathbf{r}) = \left(m_0\beta + \boldsymbol{\alpha}(\mathbf{p} - q\mathbf{A}) + q\Phi\right)\psi(\mathbf{r}). \tag{2.5}$$

This time-independent Dirac equation not only has solutions with positive energy eigenvalues, but (interestingly) there exist also negative energy eigenstates. When the Dirac equation was first derived, it was not clear what the meaning of these negative solution was and why there should be any stable state that does not decay into lower-lying negative energy states. Nowadays the common interpretation e.g. [32] uses Pauli's exclusion principle and assumes that in general all negative energy states are already occupied. Additional positive energy states correspond to the usual states of e.g. the electrons. If an electromagnetic field is used to excite one of the negative energy states into the positive continuum, the remaining hole behaves like an antifermion, e.g. like a positron. In the relativistic calculations of this thesis not only the solutions with positive, but also with negative energy will play an important role.

2.2 H-like ions in Dirac theory

H-like ions consist of a single electron, with mass $m_e = 1$, moving in the electric field of a nucleus. This nucleus consist of one or multiple nucleons, which are about 2000 times as heavy as an electron, and is thus much heavier than the electron. We can therefore assume in a good approximation that the nucleus is infinitely heavy and that its position is identical with the center of mass of the system. In such an infinitely heavy nucleus approximation an analytic solution for H-like ions can be found within the relativistic Dirac theory. Further

effects that arise from the finite mass of the nucleus, e.g. so-called isotope shifts and nuclear recoil effects, can be considered as small perturbations (c.p. [33]) but play no further role in this text.
In the approximation of an infinitely heavy nucleus H-like ions can be described by the following time-independent Dirac equation:

$$E\psi(\mathbf{r}) = \left(\beta + \boldsymbol{\alpha}\mathbf{p} - \frac{Z\alpha_S}{r}\right)\psi(\mathbf{r}). \tag{2.6}$$

Here we introduced the central potential $\frac{\alpha_S Z}{r}$ of a point-like nucleus with the distance from the origin r, an atomic number (or somewhat imprecise nuclear charge) Z, and the Sommerfeld fine structure constant α_S that was mentioned in the introduction of the unit system. This equation has been solved explicitly e.g. by Rose [31] and Drake [34]. Because of the importance of the solution for the present work I will briefly recapitulate the calculation and present some common interpretation of the solution.

It can be seen from (2.6) that the potential $V(r) = -\frac{Z\alpha_S}{r}$ of the nucleus and thus also the Hamiltonian have a spherical symmetry. We can therefore choose a spherical coordinate system. In such a system the solutions $\psi(\mathbf{r})$ can be split into angular and radial parts that can be determined separately.

$$\psi(\mathbf{r}) = \begin{pmatrix} g(r)\chi_\kappa^m(\Omega_\mathbf{r}) \\ if(r)\chi_{-\kappa}^m(\Omega_\mathbf{r}) \end{pmatrix}. \tag{2.7}$$

For convenience I here introduce the radial parts $g(r)$ for the large part and $f(r)$ for the small part of the spinor and the angular two-component spinors $\chi_\kappa^m(\Omega_\mathbf{r})$, with $\Omega_\mathbf{r}$ a spherical angle defined by the direction of $\mathbf{r}$.

In order to separate the angular dependent parts from the radial parts of the Dirac equation (2.6) the following operator is introduced, c.p. [31]:

$$K = \beta(\boldsymbol{\sigma}\mathbf{L} + 1), \tag{2.8}$$

with $\mathbf{L}$ the common non-relativistic orbital angular momentum operator.
This operator allows us to split the momentum operator in Eq. (2.6) into different parts that act on radial and an angular part of the spinor (2.7):

$$\boldsymbol{\alpha}\mathbf{p} = i\alpha_r\left(-\frac{\partial}{\partial r} + \frac{\beta K}{r} - \frac{1}{r}\right). \tag{2.9}$$

As this momentum operator is the only part of the Hamiltonian in (2.6) that depends on the angular parts of the spinor (2.7), these angular parts $\chi_\kappa^m(\Omega_\mathbf{r})$ are eigenstates of the K operator with the eigenvalues $\kappa \in \{\cdots, -2, -1, 1, 2, 3, \cdots\}$ and m the projections of the total angular momentum of the system on the quantization axis. κ is connected to the orbital and total angular momentum of the states and will be discussed in a moment. To explicitly construct the eigenstates of the K operator, we need on the one hand the spherical harmonics $Y_{lm_l}(\Omega)$, c.p. [35], which are eigenvectors of the non-relativistic orbital angular momentum operator $\mathbf{L}$ and depend on the orbital angular momentum l of the bound electron and its projection m_l. On the other hand we need eigenstates of the non-relativistic spin projection operator $S_z = \frac{\sigma_z}{2}$, c.p. [31]. With m_s the eigenvalues for the projection of the

spin on the quantization axis these eigenstates are given by: $\xi_{1/2}^{+1/2} = \begin{pmatrix} 1 \\ 0 \end{pmatrix}$ and $\xi_{1/2}^{-1/2} = \begin{pmatrix} 0 \\ 1 \end{pmatrix}$.
By coupling these two components by means of so-called Clebsch-Gordan coefficients [35, 36] we get the eigenstates of K:

$$\chi_\kappa^m(\Omega_\mathbf{r}) = \sum_{m_l, m_s} \langle l m_l, 1/2 m_s \mid jm \rangle \, Y_{l m_l}(\Omega_\mathbf{r}) \xi_{1/2}^{m_s}, \tag{2.10}$$

with j the total angular momentum of the state.
The eigenvalue κ of the K operator is connected to the total angular momentum j and the orbital angular momentum l of a state by the following relations:

$$|\kappa| = j + 1/2, \tag{2.11}$$

$$\kappa = \begin{cases} -l-1 & for\ j = l + 1/2 \\ l & for\ j = l - 1/2 \end{cases}. \tag{2.12}$$

It is interesting to compare the angular parts of the large and small part of the system. From Eq. (2.7) we see that the κ of the large and small angular parts have the same absolute value but a different sign. Thus, while the total angular momentum of these parts is the same, their orbital momenta differ. The projection m is the same for the large and the small part of the spinor.

To evaluate the radial parts of the two-component spinors, we insert Eq. (2.7) into (2.6) and get a set of differential equations for $f(r)$ and $g(r)$:

$$\frac{\partial f(r)}{\partial r} = \frac{\kappa - 1}{r} f(r) - \left(E + \frac{Z\alpha_S}{r} - 1 \right) g(r), \tag{2.13}$$

$$\frac{\partial f(r)}{\partial r} = \left(E + \frac{Z\alpha_S}{r} - 1 \right) f(r) - \frac{\kappa + 1}{r} g(r). \tag{2.14}$$

The evaluation of the solution to this system of equation is lengthy [31] and does not lead to any insights that are significant for this text. Therefore only the main results are presented here. The solutions for both $f(r)$ and $g(r)$ consist of an exponential term and a power series whose prefactors are defined by a recursion relation. In order to have bound solutions the power series can have only a finite number of non-zero summands and the recursion relation must lead to vanishing elements. This condition defines bound solutions with discrete energies given by:

$$E_{n,\kappa} = \left(1 + \left(\frac{Z\alpha_S}{n - |\kappa| + \sqrt{\kappa^2 - (Z\alpha_S)^2}} \right)^2 \right)^{-1/2}. \tag{2.15}$$

With these discrete eigenvalues and the recursion relation the radial parts of the two-component spinors can be determined and are given by:

$$\begin{aligned} g(r) =& N e^{-\beta_n^\kappa r} (\beta_n^\kappa)^{\gamma_\kappa - 1} \sum_{k=0}^{n-|\kappa|} c_{\kappa;k}^+(\beta_n^\kappa), \\ f(r) =& N e^{-\beta_n^\kappa r} (\beta_n^\kappa)^{\gamma_\kappa - 1} \sum_{k=0}^{n-|\kappa|} c_{\kappa;k}^-(\beta_n^\kappa), \end{aligned} \tag{2.16}$$

with the constants

$$N = \frac{2\gamma_\kappa(\beta_n^\kappa)^2}{\Gamma(2\gamma_\kappa+1)}\sqrt{\frac{\Gamma(2\gamma_\kappa+n-|\kappa|+1)}{\beta_n^\kappa(n-|\kappa|)!\left[Z\alpha_S/\beta_n^\kappa-\kappa)^2+(n-|\kappa|)(2\gamma_\kappa+n-|\kappa|)\right]}}, \tag{2.17}$$

$$\begin{aligned} c^\pm_{\kappa;k} =& (1\pm\sqrt{1-(\beta_n^\kappa)^2})^{1/2}\frac{\Gamma(-n+|\kappa|+k)\Gamma(2\gamma_\kappa+1)2^k}{\Gamma(-n+|\kappa|)k!\Gamma(2\gamma_\kappa+1+k)} \\ & \times\left[(k-n+|\kappa|)\pm(Z\alpha_S/\beta_n^\kappa-\kappa)\right]. \end{aligned} \tag{2.18}$$

Here we use the abbreviations $\beta_n^\kappa = \frac{Z\alpha_S}{\sqrt{(n-|\kappa|+\gamma_\kappa)^2+(Z\alpha_S)^2}}$ and $\gamma_\kappa = \sqrt{\kappa^2-(Z\alpha_S)^2}$ c.p. [31].

In these solutions specific states are determined by the quantum numbers n, κ, m where n depicts the principal quantum number. It is common to use the orbital and total angular momentum instead of κ and specify such states in the form nl_j where instead of l we use the spectroscopic notation $s: l=0;\ p: l=1;\ d: l=2;$ ..., e.g. we have $1s_{1/2}$ or $2p_{3/2}$ states.

In order to later determine what kind of transitions between these states are possible, it is useful to discuss the behavior of the spinors under spacial inversion, the so-called parity of the state. The parity of the H-like spinors originates from the spherical harmonics in Eq. (2.10) and is determined by the orbital angular momentum of the (large part of the) state and is, c.p. [31]:

$$P(|njlm\rangle) = (-1)^{l+1}, \tag{2.19}$$

i.e. for $s, d, ...$ states it 1 and for $p, f, ...$ states it is -1. I will later use the parity to determine selection rules for specific multipole contributions to electromagnetic transitions between bound states.

2.2.1 A closer look at relativistic hydrogen-like states

The relativistic solution (2.7) and (2.16) and (2.15) can not be easily understood. In order to introduce the concepts needed for a meaningful discussion of the results of this thesis, I therefore discuss their behavior in more detail.
As a first step I inspect the energy levels of the states from Eq. (2.15) in more detail. These energy levels (2.15) consist of the rest mass of the electron and the binding energy of the atom or ion. For the discussion the only interest lies in the (negative) binding energy $E_{n,\kappa;b} = E_{n,\kappa} - 1$.

As a first approximation I omit the κ dependence of $E_{n,\kappa;b}$, i.e. remove the square roots that contain κ in Eq. (2.15) and expand the resulting expressions for small values of $Z\alpha_S$. We get the well-known non-relativistic approximation of the binding energy c.p.[30]

$$E_{n;nr} = -\frac{(Z\alpha_S)^2}{2n^2}. \tag{2.20}$$

On this level of approximation the energy of the states depends mainly on the principal quantum number n and quite strongly on the nuclear charge Z of the ions. We have a $\sim Z^2$ scaling of the binding energy of the ions, i.e. the non-relativistic ground state binding energy goes from $-13.6eV$ in neutral hydrogen to $115keV$ (relativistic $132keV$) in U^{91+}

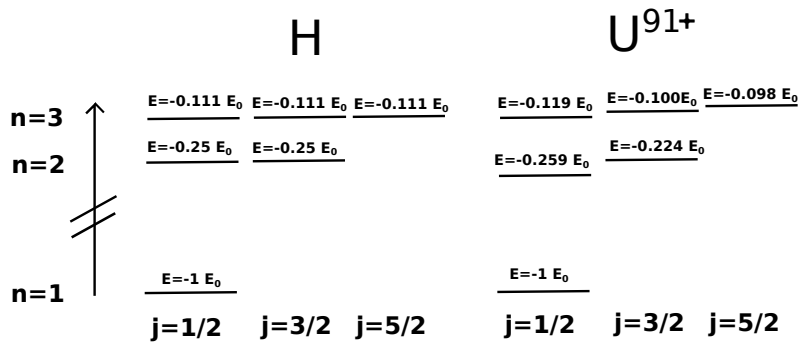

Fig. 2.1: Binding energies of different states of H-like ions in units of the ground state binding energy for neutral hydrogen ($E_0 = 13.61eV$) and U^{91+} ($E_0 = 132.3keV$).

On a more precise level the binding energy depends not only on the principal quantum number n and the nuclear charge Z, but also on the total angular momentum j, which can be found in the form of κ in (2.15). To illustrate such higher order effects, I show in Fig. 2.1 the binding energies for neutral hydrogen and U^{91+} as a function of the ground state binding energy. We see from Fig. 2.1 that, although the effect of j on the energy levels is smaller than the effect of n, especially in high-Z ions, states with the same n but different total angular momenta j have sizable different energy levels. This effect is known as the fine-structure splitting of the energy levels. The fine structure splitting is a relativistic effect and largest for states with small principal quantum number n.

In chapter 5 I will include even more precise values of the binding energy that go beyond the relativistic theory described here. On this level the energies of H-like states are influenced by the so-called Lamb shift, which is a quantum electrodynamic effect. More specifically, it is mainly caused by the self energy of the electron and the polarization of the vacuum. On top of a simple shift of all energy levels it causes differences between the energies of states with the same n and j but different orbital angular momenta l e.g. between the $2s_{1/2}$ and $2p_{1/2}$ states. While this effect is very small in light ions, e.g. the energy difference between the $2s_{1/2}$ and $2p_{1/2}$ states in neutral Hydrogen is $4.37 \cdot 10^{-6}$eV [37], it scales with Z^4 and for U^{91+} can reach up to $75eV$ [38]. As the evaluation of the Lamb shift [37] is complex and beyond the scope of this text, I will here only use the above mentioned results. It should be mentioned that in some sources some non-QED effects like nuclear recoil or for multi-electron systems the electron-electron interaction are also included in the Lamb shift [33].
Apart from the Lamb shift effects that arise from the finite lifetime of the states need to be considered. Due to the uncertainty principle such finite lifetimes lead to finite line widths in the spectrum of the ion. In our context such line widths are included as imaginary parts of the binding energies of the states.

The bound states of an electron (2.7) are even less easy to understand than their energies. It is therefore very useful to briefly discuss some properties of the states of the ion from simpler non-relativistic models.
The simplest model of an hydrogen-like ion is the quasi classical Bohr model, in which the states are described as classical orbits around the nucleus that correspond to standing

deBroglie waves (c.p. chapter 2.4 in [32]). In this model the states are on discrete orbits with the radius:

$$r_n = \frac{n^2}{Z\alpha_S}. \tag{2.21}$$

For the ground state ($n = 1$) this radius corresponds to the most probable distance of the electron, also for more sophisticated models, c.p. [30]. We see from the equation that this ground state radius shrinks for larger Z and for U^{91+} is smaller than the size of the nucleus. This small radius enhances interactions, e.g. the Z_0 mediated weak interaction between the electron and the nucleus, and makes studying of such systems very interesting.
Bohr's model also defines a quasi-classical velocity of the electron which is in the ground state:

$$v = Z\alpha_S. \tag{2.22}$$

We see that for high nuclear charges this quasi-classical speed approaches the speed of light ($c = 1$) and relativistic effects become important. In our Dirac states such an effect is visible in the small part of the spinor (2.7). For relativistic speeds, i.e. in high-Z ions, the small part reaches a similar size as the large part.
From this discussion we therefore expect that in highly charged heavy ions effects related to both the strong field as well the relativistic "speeds" become important. Such effects play a sizable role in my results.

Apart from the bound states I discussed here the Eq. (2.6) also has a continuum of solutions with positive as well as negative energies. For the two-photon processes here discussed all of these states need to be considered.

2.3 He-like ions in the independent particle model

The states of multi-electron ions, e.g. He-like ions, are defined as solutions of a two-particle Dirac equation. For such systems a Hamiltonian needs to be constructed in which each electron is described by a separate set of coordinates, e.g. for He-like ions the Dirac equation is:

$$E\psi_{He}(\mathbf{r_1}, \mathbf{r_2}) = \left(\beta + \boldsymbol{\alpha}\mathbf{p}_1 + \boldsymbol{\alpha}\mathbf{p}_2 - \frac{Z\alpha_S}{r_1} - \frac{Z\alpha_S}{r_2} + \frac{\alpha_S}{|\mathbf{r_1} - \mathbf{r_2}|}\right)\psi_{He}(\mathbf{r_1}, \mathbf{r_2}). \tag{2.23}$$

In highly charged heavy ions the $\frac{\alpha_S}{|\mathbf{r_1}-\mathbf{r_2}|}$ electron-electron interaction term in Eq. (2.23) is small in comparison to the interaction potentials of the electrons with the nucleus. Therefore, as a good approximation we can in such systems neglect this electron-electron interaction term and greatly simplify the evaluation of the states ψ_{He}. In this so-called independent particle model, c.p. [39, 40, 41, 42], the two particle equation (2.23) can be separated into two identical one-particle equations that look like Eq. (2.6). The two-electron spinor $\psi_{He}^{(N,P,J,M)}(\mathbf{r_1}, \mathbf{r_2})$ can thus be expressed in terms of the solutions of Eq. (2.6), i.e. in terms of the spinors $\psi_H^{(n_i,j_i,l_i,m_i)}(\mathbf{r})$ for H-like ions from Eq. (2.7). As the two electrons of the He-like ion are indistinguishable fermions, the resulting equation has to be properly

antisymmetrized. Within the independent particle model spinor for He-like states can be written in the following way:

$$\psi_{He}^{(N,P,J,M)}(\mathbf{r_1},\mathbf{r_2}) = \sum_{m_1\ m_2} \langle j_1 m_1, j_2 m_2 \mid JM\rangle \times\big(\psi_H^{(n_1,l_1,j_1,m_1)}(\mathbf{r_1})\psi_H^{(n_2,l_2,j_2,m_2)}(\mathbf{r_2}) -\psi_H^{(n_1,l_1,j_1,m_1)}(\mathbf{r_2})\psi_H^{(n_2,l_2,j_2,m_2)}(\mathbf{r_1})\big). \tag{2.24}$$

Here the large N, P, J, M are the main quantum number for the He-like state, which will be more closely defined in a moment, the parity, the total angular momentum, and the magnetic quantum number of the He-like state. Additionally we need the total spin of such systems S. The $n_{1,2}, l_{1,2}, j_{1,2}, m_{1,2}, s = 1/2$ are the quantum numbers of the constituent H-like states.
In this equation the angular momenta of the H-like states are coupled to the angular momenta of the He-like state by means of Clebsch-Gordan coefficients. Such a coupling of angular momenta is only non-zero if the participating angular momenta and their projections fulfill the following triangle rules: $|j_1 - j_2| \leq J \leq |j_1 + j_2|$, $|l_1 - l_2| \leq L \leq |l_1 + l_2|$, $|s_1 - s_2| \leq S \leq |s_1 + s_2|$ and $M = m_1 + m_2$.
It can be see from Eq. (2.24) that the parity of the He-like state can be defined as the product of the parities of the constituent H-like states, i.e. with Eq. (2.19) we have $P = (-1)^{l_1+l_2}$.

In such a simple model the binding energies of the He-like states, defined as the binding energies of the individual electrons, usually differ considerably from measured values. A simple way to improve the quality of the spinors is to reintroduce a part of the electron-electron interaction as an average shielding of the nuclear charge Z. In a simple approximation such shielding can be described by replacing the nuclear charge Z in the constituent H-like spinors with an effective charge Z_{eff} The effective charge Z_{eff} is estimated by comparing the binding energies evaluated by Eq. (2.15) with more complex calculations [33]. In a number of atomic processes involving highly charged heavy ions this approach has proven itself to be a useful method to obtain highly precise results, e.g. [41].

In the next chapters I will use the IPM wavefunctions (2.24) to evaluate transition properties of He-like ions. One of the electrons will from now on be considered a so-called spectator electron in the $1s_{1/2}$ ground state, which only contributes to the process by means of the coupling of the angular momenta (2.24). All other parts of the calculation will be performed on the other "acting" electron. For He-like states in which one electron is in the ground state there exists a special spectroscopic notation. In this situation the principal quantum number of the active electron can be used as the "principal" quantum number N of the He-like state. With such a quantum number the He-like state can be uniquely defined by their quantum numbers N, P, J, M. I will characterize He-like states by these quantum numbers written in the form $N^{2J+1}L_S$. In analogy to the notation of H-like states, I define a spectroscopic notation in which L is determined by both the total angular momentum J and the parity P of the state, i.e. we have $L = S$ for $J = 0, 1$ and $P = 1$, $L = P$ for $J = 0, 1, 2$ and $P = -1$, $L = D$ for $J = 2, 3$ and $P = 1$ (and so on). In this notation we have e.g. $1s_{1/2}2s_{1/2} : 2^1S_0$ and $1s_{1/2}2p_{1/2} : 2^3P_1$ or shorter 2^1S_0 and 2^3P_1 states in which the spectator electron is in the $1s_{1/2}$ state and the interacting electron is in the $2s_{1/2}$ or $2p_{1/2}$ state.

3 Ions and electromagnetic fields

Electromagnetism is the dominant force in atomic physics. It is not only responsible for the binding of electrons to the nucleus, but also for the interaction of atoms and ions with their environment. Of special importance is the interaction between photons and atoms or ions, which is the origin of transitions between different states of the ions, especially the two-photon processes studied in this thesis. These processes are facilitated by absorption or emission of one or multiple photons. In the first part of this chapter I show how such processes can be described in a perturbative way by means of an effective electron-photon interaction operator that can be derived using a simplified approach to quantum electrodynamics. Specific photon-ions interaction processes are then described using time-dependent perturbation theory. In this approach the two-photon processes can be studied by means of the second-order of the time-dependent perturbation series.

On top of the electromagnetic transitions caused by the interaction of the atoms or ions with dynamic electromagnetic fields, static external electric fields can lead to changes to the bound states of the system. To estimate the effects of such electric fields, in the second part of this chapter I briefly analyze the influence of static electric fields on the states of the ions, using the non-degenerate time-independent perturbation theory.

3.1 Time-dependent perturbation theory and photon-ion interaction

3.1.1 The electron-photon interaction operator

Electromagnetic transitions are facilitated by emission or absorption of photons. Such photons enter the relativistic theoretical description as a vector potential in Eq. (2.1).
To describe all electron-photon interactions including the spontaneous decay of excited states, a photon-electron interaction operator is most clearly derived by means of a simplified approach to quantum electrodynamic (QED) as shown in [32, 43]. This approach starts with a quantization of the electromagnetic field in which we assume that all physics happens in a finite but large volume V. The calculation is best performed in the well-known Coulomb gauge of the electromagnetic field, i.e. the scalar potential vanishes and we have $\Phi = 0$. Such a gauge fixing only introduces a unitary factor to the states I presented in chapter 2. Observables are not influenced by this factor, thus the states can be used in conjunction with the effective operator I will derive now, c.p. chapter 4.1 in [30].

As a first step we consider a Fourier decomposition of the vector potential into plane waves:

$$\mathbf{A} = \sum_{\lambda} \sum_{\mathbf{k}} \left[\mathbf{u}_\lambda b_{\mathbf{k}\lambda} e^{i(kr - \omega_{\mathbf{k}} t)} + \mathbf{u}_\lambda b^\dagger_{\mathbf{k}\lambda} e^{-i(\mathbf{k}\mathbf{r} - \omega_{\mathbf{k}} t)} \right], \tag{3.1}$$

with $\mathbf{u}_\lambda$ the polarization vectors for circular polarized photons with helicity $\lambda = \pm 1$, $\mathbf{k}$ the wave vectors of the photons, and $\omega_{\mathbf{k}}$ their frequencies. The $b_{\mathbf{k}\lambda}$ are for now just non-commutative Fourier components of the vector potential.

Using this decomposition the well-known total energy E_{EM} of the EM field can be written as:

$$E_{EM} = \int_V d^3\mathbf{r} \frac{1}{2}(E^2 + B^2) = \sum_{\mathbf{k}\lambda} V k^2 (b_{\mathbf{k}\lambda} b^\dagger_{\mathbf{k}\lambda} + b^\dagger_{\mathbf{k}\lambda} b_{\mathbf{k}\lambda}) = \sum_{\mathbf{k}\lambda} \frac{1}{2}(p^2_{\mathbf{k}\lambda} + \omega^2_{\mathbf{k}} q^2_{\mathbf{k}\lambda}), \tag{3.2}$$

with $q_{\mathbf{k}\lambda} = \sqrt{V}(b_{\mathbf{k}\lambda} + b^\dagger_{\mathbf{k}\lambda})$ and $p_{\mathbf{k}\lambda} = -i\sqrt{V}\omega_{\mathbf{k}}(b_{\mathbf{k}\lambda} - b^\dagger_{\mathbf{k}\lambda})$.

In the last expression of Eq. (3.2) we can see a decomposition of the energy into so-called eigenmodes of the electromagnetic field. The contribution of each eigenmode has the form of an harmonic oscillator. In analogy to the harmonic oscillator, I quantize the electromagnetic field by introducing commutation relations between $p_{\mathbf{k}\lambda}$ and $q_{\mathbf{k}\lambda}$:

$$[p_{\mathbf{k}\lambda}, q_{\mathbf{k}'\lambda'}] = -i\delta_{\mathbf{k},\mathbf{k}'}\delta_{\lambda\lambda'}. \tag{3.3}$$

In the new quantized context the $b_{\mathbf{k}\lambda}$ and $b^\dagger_{\mathbf{k}\lambda}$ can be considered annihilation and creation operators of a specific mode. They satisfy the following commutation relation:

$$\left[b_{\mathbf{k}\lambda}, b^\dagger_{\mathbf{k}\lambda'} \right] = \frac{1}{2\omega_{\mathbf{k}} V} \delta_{\mathbf{k},\mathbf{k}'}\delta_{\lambda,\lambda'}. \tag{3.4}$$

The creation and annihilation operators allows us to define the excitation or photon number operators:

$$\hat{n}_{\mathbf{k}\lambda} = b^\dagger_{\mathbf{k}\lambda} b_{\mathbf{k}\lambda}. \tag{3.5}$$

The eigenvalues of these operators specify the excitation $n_{\mathbf{k}\lambda}$ of, or the number of photons in, the mode with $\mathbf{k}, \lambda$.
For example, the photon number $n_{\mathbf{k}\lambda}$ for plane monochromatic circular polarized electromagnetic waves (with λ the helicity of the photons) can be expressed in terms of the angular frequency $\omega = |\mathbf{k}|$ and intensity $I = E_{EM}/V \cdot c$, with $c = 1$ the speed of light:

$$n = \frac{VI}{\omega}. \tag{3.6}$$

With the help of the eigenvalues of the number operators (3.5) the energy of the electromagnetic field in a given state is:

$$E_{EM} = \sum_{\mathbf{k}\lambda} \omega_{\mathbf{k}} \left(n_{\mathbf{k}\lambda} + \frac{1}{2} \right). \tag{3.7}$$

We now use the definition of the energy of the electromagnetic(EM) field (3.7) in terms of the photon numbers $n_{\mathbf{k}\lambda}$ to derive an effective model for the interaction of a single electron with photons. For this model we need the the numerical size of the contribution of each creation or annihilation operator to the vector potential $\mathbf{A}$. I introduce here the well-known

bra-ket notation to describe a transition between abstract states. The absolute value of a transition matrix element between a state of the electromagnetic field with $n_{\mathbf{k}\lambda}+1$ photons in the $\mathbf{k},\lambda$ mode and $\langle n_{\mathbf{k}\lambda}|$ (with only $n_{\mathbf{k}\lambda}$ photons) by means of the operator $b_{\mathbf{k}\lambda}$ and a similar element for $b^\dagger_{\mathbf{k}\lambda}$ is:

$$|\langle n_{\mathbf{k}\lambda}\,|b_{\mathbf{k}\lambda}|\,n_{\mathbf{k}\lambda}+1\rangle| = \left|\left\langle n_{\mathbf{k}\lambda}+1\,\middle|\,b^\dagger_{\mathbf{k}\lambda}\,\middle|\,n_{\mathbf{k}\lambda}\right\rangle\right| = \sqrt{\frac{n_{\mathbf{k}\lambda}+1}{2\omega_{\mathbf{k}}V}}. \tag{3.8}$$

With the constants (3.8) it is now possible to construct an effective interaction Hamiltonian for the emission or absorption of a photon. For example, if we assume that initially the electromagnetic field is defined by the photon numbers $n_{\mathbf{k}\lambda}$, we can insert the vector potential (3.1) with these constants in (2.1) and get:

$$\begin{aligned} H_{ph} =& \sqrt{\alpha_S}\boldsymbol{\alpha}\mathbf{A} \\ =& \sum_\lambda \int d^3k \sqrt{\alpha_S}\left(\sqrt{\frac{n_{\mathbf{k}\lambda}}{2\omega_{\mathbf{k}}V}}\boldsymbol{\alpha}\mathbf{u}_\lambda b_{\mathbf{k}\lambda}e^{i(\mathbf{kr}-\omega_{\mathbf{k}}t)} + \sqrt{\frac{n_{\mathbf{k}\lambda}+1}{2\omega_{\mathbf{k}}V}}\boldsymbol{\alpha}\mathbf{u}^*_\lambda b^\dagger_{\mathbf{k}\lambda}e^{-i(\mathbf{kr}-\omega_{\mathbf{k}}t)}\right). \end{aligned} \tag{3.9}$$

For convenience, we here consider the limit of a huge but finite volume V and replace the sum $\sum_{\mathbf{k}}$ with an integral $\int d^3\mathbf{k}$. Furthermore, we reintroduce the Dirac matrices $\boldsymbol{\alpha}$ from chapter 2 and the Sommerfeld fine structure constant α_S from chapter 1.

The interaction Hamiltonian (3.9) models the absorption (first term) of photons from the EM-field and the (spontaneous and induced) emission (second term) of photons to the EM-field on the level of regular relativistic quantum physics. In the second term the emission is spontaneous if there are initially no photons, i.e. $n_{\mathbf{k},\lambda}=0$ in (3.9). If we have $n_{\mathbf{k},\lambda}>0$ for a $\mathbf{k},\lambda$, the emission in the mode $\mathbf{k},\lambda$ is enhanced and there is additionally so-called induced emission.
The operator (3.9) does not specify which helicity λ the absorbed or emitted photons have. For absorption or induced emission specific polarizations can be selected by defining appropriate initial photon numbers $n_{\mathbf{k}\lambda}$. However, if we are interested in the polarization properties of a spontaneously emitted photon, we have to consider single summands of $\sum_\lambda$ in Eq. (3.9).

For practical use in the upcoming calculations it is convenient to split the interaction Hamiltonian (3.9) into on the one hand the constant prefactors and the time-dependent parts and on the other hand the so-called photon absorption operator:

$$R^1_\lambda(\mathbf{k}) = \boldsymbol{\alpha}\mathbf{u}_\lambda e^{i\mathbf{kr}}, \tag{3.10}$$

as well as the similar so-called photon emission operator:

$$R^{1\,\dagger}_\lambda(\mathbf{k}) = \boldsymbol{\alpha}\mathbf{u}^*_\lambda e^{-i\mathbf{kr}}. \tag{3.11}$$

Multipole expansion of the photon absorption operator

In their current representation the photon absorption (3.10) and emission (3.11) operators are impractical for calculations of atomic processes. They contain an exponential term which makes evaluations of useful properties very hard. A more convenient representation can be obtained by performing a multipole expansion of these interaction operators.
A common expansion, c.p. [42], for circular polarized photons with helicity $\lambda = \pm 1$ can be obtained by first assuming that the photon propagates along the quantization axis and expanding the exponential term in terms of spherical harmonics, c.p. [35]. Subsequently the propagation direction of the photon can be generalized to any propagation direction $\Omega_{\mathbf{k}}$ of the photon by means of so-called Wigner rotation matrices $D^L_{M\lambda}(\Omega_{\mathbf{k}})$. In this approach the absorption operator can be written in the form:

$$R^1_\lambda(\mathbf{k}) = \sqrt{2\pi} \sum_{p,L,M} \sqrt{2L+1} i^L (i\lambda)^p \boldsymbol{\alpha} \mathbf{a}^{(p)}_{LM} D^L_{M\lambda}(\Omega_{\mathbf{k}}), \tag{3.12}$$

where L is the multipole order and p distinguishes so-called "electric" (p=1) transition, which foremost lead to changes of the shape of the atomic orbital, from so-called "magnetic" (p=0) transitions that are connected to changes of the angular momentum of the ion, most importantly to changes in the direction of the spin. The multipole component $\mathbf{a}^{(p)}_{LM}$ has been derived e.g. in [44] and is:

$$\mathbf{a}^{(p)}_{LM} = \sum_\Lambda j_\Lambda(kr) \mathbf{Y}^\Lambda_{LM}(\Omega_{\mathbf{r}}) \xi^{(p)}_{L\Lambda}, \tag{3.13}$$

where $j_L(kr)$ is the spherical Bessel function. The $\mathbf{Y}^J_{LM}(\Omega_{\mathbf{r}}) = \sum_{m,\lambda} \langle Lm, 1\lambda \mid JM \rangle Y_{Lm}(\Omega_{\mathbf{r}}) \mathbf{u}_\lambda$ are the so-called vector spherical harmonics [45] with $Y_{LM}(\Omega \mathbf{r})$ the regular spherical harmonics and we have the parameter:

$$\xi^{(p)}_{L\Lambda} = \delta_{p,0}\delta_{L,\Lambda} + \delta_{p,1} \left(\delta_{L-1,\Lambda} \sqrt{\frac{L+1}{2L+1}} - \delta_{L+1,\Lambda} \sqrt{\frac{L}{2L+1}} \right). \tag{3.14}$$

We see from Eq. (3.12) that the multipole expansion of the absorption operator is a sum of the multipole components $\mathbf{a}^{(p)}_{LM}$ with some prefactors. These components are commonly called magnetic multipole components for $p = 0$ and electric multipole components for $p = 1$. Furthermore, the different multipole orders L are called "dipole" for $L = 1$, "quadrupole" for $L = 2$, and so on. Thus we have e.g. electric dipole or magnetic quadrupole contributions. Quite often these contributions are abbreviated by writing E for electric and M for magnetic transitions followed by the multipole order, e.g. E1,M1,E2,... .

If we consider transitions between two states of an ion, especially between bound states as in this thesis, the contributions from the lower order multipole components to a transition amplitude of any kind are usually bigger than the higher order contributions. It is possible to estimate the relative size of these contributions by comparing the size of different multipole components of the interaction operator at typical photon energies and typical atomic length scales. For transitions between bound states typical photon energies are in the order of magnitude of the binding energy of the electron (2.20), i.e. $k_s \sim E_s \sim (Z\alpha_S)^2$. The electron on the other hand is here in the ground state or a low excited state, thus a typical length

scale is given by the quasi-classical electron radius (2.21), i.e. $r_s \sim \frac{1}{Z\alpha_S}$ we discussed in chapter 2.

When we later consider transitions between bound states of an atom or ion, the size of contributions from different multipoles of the interaction operator (3.12) is mostly determined by the multipole component $\mathbf{a}_{LM}^{(p)}$. These multipole components are up to some prefactors defined by the spherical Bessel functions $j_\Lambda(k_s r_s)$ with $\Lambda = L$ for magnetic transitions and $\Lambda = L \pm 1$ for electric transitions, c.p. Eq. (3.13). At the typical length scales and the energies I introduced, especially for small Z, the argument of the spherical Bessel function $k_s \cdot r_s$ is small. For such small arguments spherical Bessel functions can be approximated by a polynomial, i.e. we have $j_n(x) \sim x^n$ for $x \to 0$ c.p. [46]. Additional to this Z-dependence from the Bessel function, the Dirac matrix in the absorption or emission operator (3.10) contributes another factor $Z\alpha_S$, as it has a similar structure as an relativistic velocity operator (c.p. e.g. Chapter 12 in [32]) and the quasi-classical electron speed in the ground state (2.22) has such a $Z\alpha_S$ scaling. In leading order the electric multipole contributions thus scale like $(Z\alpha_S)^L$ and the magnetic multipole contributions scale like $(Z\alpha_S)^{L+1}$, i.e. in comparison to electric dipole transition amplitudes, magnetic dipole transition amplitudes and electric quadrupole transition amplitudes are suppressed by $Z\alpha_S$. The higher multipole contributions are therefore suppressed in light atoms or ions and mostly become important for atomic physics processes in highly charged heavy ions. In an analog way we can see that for high photon energies, which can be found e.g. in scattering experiments, the higher multipole contributions also play an important role. On top of such processes involving high energy photons the next order contributions become very important if the lowest order transitions are forbidden by so-called selection rules.

Such selection rules originate partially from parity considerations. It is therefore useful to take a look at the parity of the multipole components and their role in the transition. From the definitions of the multipole components (3.13) and vector spherical harmonics as well as the well-known parity of the spherical harmonics [35] we see that the parity of the components is:

$$P(\mathbf{a}_{LM}^{(p)}) = (-1)^{L+p+1}, \tag{3.15}$$

e.g. the E1 component has parity -1 and the M1 component has parity $+1$.

In transitions between atomic states by means of electromagnetic radiation the parity must be conserved [30, 32, 43]. Thus the parity of the final states must be equal to the product of the parity of the initial state of the transition and the parity of the multipole component. Multipole components with parity -1 can thus only contribute to transitions between states of opposite parities and $+1$ party components only to transitions between states of the same parity.
By using the parities of the states (2.19) from chapter 2 we can thus decide which specific multipole contributions p, L play a role in a single photon transition between an initial state with an orbital angular momentum l_a and a final state with an angular momentum l_b. We have a non-zero contribution if the following condition is met:

$$(-1)^{l_a - l_b + L + p + 1} = 1. \tag{3.16}$$

A similar selection rule also exists for transitions involving ions with more than one electron.

Linear polarized photons and two-electron ions

Up till now we only considered the emission or absorption of circular polarized light by single electron systems. With little effort the interaction operators can be generalized to describe the emission or absorption of linear polarized light and transitions in multi-electron systems.

First to include linear polarized photons, we take a detailed look at interaction Hamiltonian (3.9) . In this operator there is a sum over the helicities of the photons $\lambda = \pm 1$. As I mentioned before, specific helicities can be selected (for absorption and stimulated emission) by specifying initial photon occupation numbers $n_{\mathbf{k}\lambda}$. For spontaneously emitted photons such a polarization can be selected by only considering one of the summands of the helicity sum of the emission part of Eq. (3.9). To generalize this method to be able to describe linear polarized photons, their linear polarization vector $\boldsymbol{\epsilon}_i$ is expanded in terms of the circular polarization vectors $\mathbf{u}_\lambda$.

$$\boldsymbol{\epsilon}_i = \sum_\lambda \epsilon_i^\lambda \mathbf{u}_\lambda, \tag{3.17}$$

where the polarization expansion parameters ϵ_i^λ are introduced.
If $\boldsymbol{\epsilon}_i$ describes linear polarized light tilted by some angle δ_i with respect to a fixed plane (e.g. in photon scattering it could be the scattering plane) the parameters are given by, c.p. [35]:

$$\epsilon_i^\lambda = \frac{-\lambda}{\sqrt{2}} e^{i\lambda\delta_i}. \tag{3.18}$$

These polarization expansion parameters allow to describe the interaction of an ion with linear polarized light in a similar way as we described the interaction with circular polarized light. For example, we can define a photon number for the absorption (and stimulated emission) of linear polarized light with the polarization vector $\boldsymbol{\epsilon}_i$:

$$n_{\mathbf{k}\boldsymbol{\epsilon}_i} = \sum_\lambda \epsilon_i^\lambda n_{\mathbf{k}\lambda}. \tag{3.19}$$

Similarly we can introduce such parameters to allow to describe spontaneous emission of $\boldsymbol{\epsilon}_i$ polarized photons.
Both these cases can be used to define an interaction Hamiltonian for polarized light:

$$\begin{aligned} H_{ph}(\boldsymbol{\epsilon}_i) = \sum_\lambda \int d^3k \sqrt{\alpha_S} \Big(& \sqrt{\frac{n_{\mathbf{k}\lambda}}{2\omega_{\mathbf{k}} V}} \epsilon_i^\lambda \boldsymbol{\alpha} \mathbf{u}_\lambda b_{\mathbf{k}\lambda} e^{i(\mathbf{kr}-\omega_{\mathbf{k}}t)} \\ & + \sqrt{\frac{n_{\mathbf{k}\lambda}+1}{2\omega_{\mathbf{k}} V}} \epsilon_i^{\lambda\,*} \boldsymbol{\alpha} \mathbf{u}_\lambda^* b_{\mathbf{k}\lambda}^\dagger e^{-i(\mathbf{kr}-\omega_{\mathbf{k}}t)} \Big). \end{aligned} \tag{3.20}$$

This Hamiltonian has a very similar structure as the original interaction Hamiltonian (for circular polarized light) (3.9). Like in Eq. (3.9) we can therefore separate Eq. (3.20) into so-

called photon emission and absorption operators with which all important calculations can be performed and some prefactors. In such a separation the polarization expansion coefficients show up as separate linear coefficients. It is possible to ignore these coefficients and as a first step perform the calculations of transition matrix elements for absorption or emission of circular polarized photons Eq. (3.9). Afterwards the polarization expansion coefficients can be reintroduced in the last step to evaluate the transition or scattering amplitudes for linear polarized photons from transition amplitudes for circular polarized photons. In such a procedure the polarization of absorbed photons is included by the parameters ϵ_i^λ while for the emission is included by means of the complex conjugated parameters $\epsilon_i^{\lambda\,*}$. We will use this approach in chapter 6 to describe the scattering of linear polarized photons.

To describe the emission or absorption of photons by two-electron ions we have to include the interaction of the electromagnetic field with both electrons. Each of these electrons has a separate set of spacial coordinates $\mathbf{r}_i$ and independent spinor components. Since the electrons are indistinguishable, the interaction operator is simply the sum of single electron interaction operators for these coordinates:

$$\begin{aligned} H_{ph}^{He} = &\sum_{a=1}^{2}\sum_{\lambda}\int d^3k\sqrt{\alpha_S}\Big(\sqrt{\frac{n_{\mathbf{k}\lambda}}{2\omega_{\mathbf{k}}V}}\boldsymbol{\alpha}_a\mathbf{u}_\lambda b_{\mathbf{k}\lambda}e^{i(\mathbf{k}\mathbf{r}_a-\omega_{\mathbf{k}}t)} \\ &+\sqrt{\frac{n_{\mathbf{k}\lambda}+1}{2\omega_{\mathbf{k}}V}}\boldsymbol{\alpha}_a\mathbf{u}_\lambda^* b_{\mathbf{k}\lambda}^\dagger e^{-i(\mathbf{k}\mathbf{r}_a-\omega_{\mathbf{k}}t)}\Big). \end{aligned} \tag{3.21}$$

Here the $\boldsymbol{\alpha}_a$ are Dirac matrices that operate on the spinor components of the electron a.

In analogy to the one-electron case we can also define emission and absorption operators for two-electron ions. Such operators are given by:

$$R_\lambda^2(\mathbf{k}) = \sum_{a=1}^{2}\boldsymbol{\alpha}_a\mathbf{u}_\lambda e^{i\mathbf{k}\mathbf{r}_a}, \tag{3.22}$$

and

$$R_\lambda^{2\,\dagger}(\mathbf{k}) = \sum_{a=1}^{n}\boldsymbol{\alpha}_a\mathbf{u}_\lambda^* e^{-i\mathbf{k}\mathbf{r}_a}. \tag{3.23}$$

As these operators have the same structure as Eq. (3.10) and Eq. (3.11), most of the derivations can be performed in complete analogy to the one-electron interactions and these operators for He-like systems can be expanded in terms of similar multipole components as the operators for H-like ions. We can define multipole components $\mathbf{a}_{LM}^{(p)}(He)$ for the He-like systems:

$$\boldsymbol{\alpha}\mathbf{a}_{LM}^{(p)}(He) = \sum_{a=1,2}\boldsymbol{\alpha}_a\mathbf{a}_{LM}^{(p)}, \tag{3.24}$$

where the H-like multipole components $\mathbf{a}_{LM}^{(p)}$ act on the spacial coordinates of the electron marked by the index a of the Dirac matrix in front of them and we use the expression on the right side of Eq. (3.24).

3.1.2 Time-dependent perturbation theory

The interaction operators (3.9),(3.20),(3.21) we derived in the first part of this chapter could in principle be used as part of the equation of motion of the Dirac theory (2.1) to find time dependent solutions for states emitting or absorbing photons. In practice the derivation of a solution requires a perturbative approach. The transition process is described by means of time-dependent perturbation theory. Such an approach does not only make the evaluation of decay properties relatively easy but also allows to distinguish different experimental phenomena, such as single and multi-photon transitions. I will now briefly introduce the time-dependent perturbation theory to show the basic concepts of this approach.
In time-dependent perturbation theory we assume that the Hamiltonian of the system:

$$H(t) = H_0 + H_{per}(t), \tag{3.25}$$

consists of a large time-independent part H_0 and a small time-dependent perturbation H_{per}. Ideally the time-independent Hamiltonian has a set of known eigenstates $|\nu\rangle$, like the spinors we derived for H-like ions.
In the abstract bra-ket notation these eigenstates are solutions of:

$$H_0 |\nu\rangle = E_\nu |\nu\rangle . \tag{3.26}$$

The eigenstates of the time-independent Hamiltonian are usually known by their time-independent part. For the following discussion we will however need the full time-dependent state. As we showed in Eq. (2.4), such states are simply given by:

$$|\nu, t\rangle = |\nu\rangle e^{-iE_\nu t}. \tag{3.27}$$

To derive the time-dependent perturbation theory, the time dependence of the system arising from H_0 is now transferred from the time-dependent states $|\psi, t\rangle$ to the operators B that operate on these states. We make a transition from the previous so-called Schrödinger picture to the so-called Dirac or interaction picture. The new state and operators in this interaction picture are defined by:

$$|\psi\rangle_{int} = e^{iH_0(t-t_0)} |\psi, t\rangle , \tag{3.28}$$

$$B_{int} = e^{iH_0(t-t_0)} B e^{-iH_0(t-t_0)}. \tag{3.29}$$

Furthermore, there is new set of equations that describes both the time evolution of the states as well as the operators B acting on these states:

$$i\frac{\partial |\psi\rangle_{int}}{\partial t} = H_{per,int} |\psi\rangle_{int} , \tag{3.30}$$

$$i\frac{\partial B_{int}}{\partial t} = [B_{int}, H_0] , \tag{3.31}$$

here $H_{per,int}$ is the time-dependent perturbation operator from Eq. (3.25) transferred into the interaction picture with Eq. (3.29).

Eq. (3.30) allows to define an abstract time evolution operator:

$$U(t,t_0) = e^{-i\int_{t_0}^{t} H_{per,int}(\tau)d\tau}. \tag{3.32}$$

The main idea of the time-dependent perturbation theory is now to develop this time evolution operator as a series in orders of t, c.p. [32, 43]:

$$U(t,t_0) \approx 1 - i\int_{t_0}^{t} d\tau_1 H_{per,int}(\tau_1) - \int_{t_0}^{t} d\tau_1 \int_{t_0}^{\tau_1} d\tau_2 H_{per,int}(\tau_1)H_{per,int}(\tau_2) + \cdots . \tag{3.33}$$

We call the contributions corresponding to a certain order of the time t, the order of the perturbation series n, i.e. in Eq. (3.33) the second and third terms on the right side correspond to the first-($U_1(t,t_0)$) and second-($U_2(t,t_0)$)order of the time evolution operator. With this time evolution operator it is possible to perturbatively study the time evolution of a system, e.g. initially (at t_0) prepared in the eigenstate $|a\rangle$ of H_0. At this time we set $|a\rangle = |a\rangle_{int}$. When we assume that at t_0 the time-dependent perturbation is "switched on" the probability $P(t,t_0)$ to find the system after a time $t-t_0$ in the eigenstate $|b\rangle$ is given by:

$$P(t,t_0) = W(t-t_0) = |\langle b\,|U_1(t,t_0) + U_2(t,t_0)|\,a\rangle|^2\,, \tag{3.34}$$

here we used that the $|a\rangle$ and $|b\rangle$ are orthonormal and the zeroth-order contribution of the time evolution operator vanishes. Furthermore, in many interesting physical cases we can introduce a constant transition rate W, as seen in the second term of Eq. (3.34). Such a rate will be defined for single- and two-photon processes.
In Eq. (3.34) the transition probability depends on the square of matrix elements that will be called the time evolution amplitudes $M_n(t,t_0) = \langle b\,|U_n(t,t_0)|\,a\rangle$. I will now discuss these time evolution amplitudes for the special case of radiative transition between bound states of an ion.

Perturbative description of one- and two-photon processes

In this work we study briefly the first- (and more prominently) the second-order of the perturbation theory. For a perturbative interaction with the quantized electromagnetic field these orders allow us to describe one- and two-photon processes. We discuss the example of one- and two-photon absorption (without loss of generality in H-like ions) in detail and briefly show how these results can be generalized to all one- and two-photon processes. Without loss of generality we choose $t_0 = 0$ and derive the interaction operator for the absorption of circular polarized photons in the Dirac picture from the definitions (3.9), (3.29) and (3.10):

$$H_{per,int} = C \cdot e^{iH_0 t} R^1_\lambda(\mathbf{k}) e^{i\omega_\mathbf{k} t} e^{-iH_0 t}, \tag{3.35}$$

with the numerical constant

$$C = \sqrt{\alpha_S \frac{n_{\mathbf{k}\lambda}+1}{2\omega_\mathbf{k} V}}. \tag{3.36}$$

This interaction operator for photon absorption is very useful if we are not interested in the polarization (or only in circular polarization) of the photon. We use it to evaluate time

evolution amplitudes for circular polarized photons that can also be used to derive the comparable amplitudes for linear polarized photons by means of the polarization expansion parameters (3.18).

We now briefly discuss the behavior of the first- and second-order time evolution amplitudes $M_n(t)$ with the interaction operator (3.35). It is at this point useful to keep in mind that transition probabilities and related properties arise from the square of these amplitudes $|M_n(t)|^2$.

First-order: emission and absorption With the first-order of the time evolution amplitude we describe the absorption of a photon with wave vector $\mathbf{k}$ and the helicity λ. An absorption of such a photon with the energy ω_k by an ion in the eigenstates $|a\rangle$ with an energy E_a leads to a transition into the eigenstate $|b\rangle$ with energy E_b. The time evolution amplitude of such a process is given by:

$$\begin{aligned}\langle b\,|U_1(t,0)|\,a\rangle =& -iC\int_0^t d\tau\,\langle b\,|e^{iE_b\tau}R^1_\lambda(\mathbf{k})e^{-i\omega_k\tau}e^{-iE_a\tau}|\,a\rangle \\ =& C\,\langle b\,|R^1_\lambda(\mathbf{k})|\,a\rangle\cdot(-i)\int_0^t d\tau e^{i(E_b-\omega_k-E_a)\tau}.\end{aligned} \tag{3.37}$$

The evaluation of the time evolution amplitude can be split into evaluating a time-independent matrix element which we will call the transition or more specifically absorption amplitude M_{fi} and an integral over time

$$K(t,E_b-\omega_k-E_a) = -i\int_0^t d\tau e^{i(E_b-\omega_k-E_a)\tau}. \tag{3.38}$$

In first-order calculations it can be shown, e.g. [30, 32], that, if we consider the transition processes after a relatively long time, the time-dependent integral leads to an energy conservation condition in the transition probability. We get $|K(t)|^2 \to const\cdot t\cdot\delta(E_b-\omega_k-E_a)$ for $t\to\infty$. As expected we have fixed frequencies at which one photon absorption is possible: $\omega_k = E_b - E_a$.
Single photon emission can be described in a similar way as single photon absorption by replacing $H_{per,int}$ with $H^\dagger_{per,int}$. For such processes the time integral will look slightly different and lead to an energy conservation relation $E_b = E_a - \omega_k$, in which the final state has less energy than the initial one.

Second-order: two-photon processes The second-order of the time evolution amplitude is slightly more complicated than the first-order amplitude. For two-photon absorption it describes the simultaneous absorption of two photons and contains a product of two interaction Hamiltonians $H_{int,per}$. In order to evaluate such a product, we include a unity operator $I = \sum_\nu |\nu\rangle\langle\nu|$ between the photon-electron operators, where the index ν runs over all states of the ion including the positive and negative continuum. Under the naive

assumption that we can force one of the photons with energy ω_2 to be absorbed "first", the second-order time evolution amplitude is:

$$\begin{aligned}\langle b\,|U_2(t)|\,a\rangle = -\,C^2 \int_0^t d\tau \int_0^\tau d\tau' \sum_\nu \Big(\big\langle b\,\big|e^{-iE_b\tau} R^1_{\lambda_1}(\mathbf{k}_1) e^{-i\omega_1\tau} e^{iE_\nu\tau}\big|\,\nu\big\rangle \\ \times \Big\langle \nu\,\Big|e^{-E_\nu\tau'} R^1_{\lambda_2}(\mathbf{k}_2) e^{-i\omega_2\tau'} e^{-iE_a\tau'}\Big|\,a\Big\rangle\Big),\end{aligned} \tag{3.39}$$

like in the first-order amplitude we can separate the evaluation into time-independent parts and time integrals that can be performed separately.

If we exclude all photon energies ω_2 with $\omega_2 = E_a - E_\nu$, i.e. energies that would lead to a single photon excitation of the state ν, one of the time integrals can be explicitly evaluated and the time-dependent part becomes:

$$K_2(t) = \frac{1}{E_\nu - \omega_2 - E_a} K(t, E_a + \omega_1 + \omega_2 - E_b), \tag{3.40}$$

where $K(t, E_a + \omega_2 + \omega_1 - E_b)$ has the same structure as the time integral (3.38) in the single-photon case.

For such energies the (naive) two-photon absorption matrix can be written as:

$$\langle b\,|U_2(t)|\,a\rangle = K(t, E_a + \omega_1 + \omega_2 - E_b) C^2 \sum_\nu \frac{\big\langle b\,\big|R^1_{\lambda_1}(\mathbf{k}_1)\big|\,\nu\big\rangle \big\langle \nu\,\big|R^1_{\lambda_2}(\mathbf{k}_2)\big|\,a\big\rangle}{E_\nu - \omega_2 - E_a}. \tag{3.41}$$

In this equation we call the non-time dependent sum over ν the (naive) transition matrix amplitude M_{12}. In real physical processes the photons are indistinguishable. Thus the transition amplitude must be symmetrized, i.e. we must include both cases, the one where photon "1" is absorbed "first" (M_{21}) and the one where photon "2" is absorbed "first" (M_{12}). A physical two-photon transition amplitude (or later for photon scattering processes scattering amplitude) M_{fi} is thus given by:

$$M_{fi} = M_{12} + M_{21}, \tag{3.42}$$

M_{21} has the same form as M_{12}, but with the index "1" and "2" in the operators and energies switched.
As it was discussed for the first-order amplitude the time-dependent part of Eq. 3.41 leads to an energy conservation condition. For two-photon absorption it has the following form.

$$E_f = E_i + \omega_1 + \omega_2. \tag{3.43}$$

In contrast to single photon absorption we see that, as long as the sum of the photon energies is equal to the energy difference between the initial and final state, the energy of the transition $E_b - E_a$ can be continuously distributed between the two photons.

Based on the derivation of this two-photon absorption process, different two-photon processes can be modeled by replacing one (photon scattering) or both (two-photon emission) interaction operators for absorption of a photon $H_{int,per}$ by emission operators $H^\dagger_{int,per}$. For such processes there is a energy conservation condition that can be obtained from Eq. (3.43) by changing the signs of the photon energy $\omega_{1/2}$ for the emitted photons.

In the discussion of two-photon processes it is sometimes useful to interpret the transition process seen e.g. in amplitude M_{fi} as a two-step process where we have e.g. first an absorption of one photon which excites the ion into a so-called virtual intermediate state - represented in Eq.3.41 by the expression $\sum_\nu \frac{|\nu\rangle\langle\nu|}{E_i-\omega_1-E_\nu}$. In a second step we have a transition of this virtual intermediate state into the real final state by absorption of a second photon, c.p. Fig. 1.1. Like any simple interpretation we must take this model with a grain of salt and keep in mind that in the two-photon process both photons are absorbed simultaneously and we always need to symmetrize the transition or scattering amplitudes. However, this model allows us to define a parity condition for two-photon transitions. By considering the absorption or emission of the two participating photons as separate interaction processes, we can see from the single photon parity condition (3.16) that only multipole contributions that fulfill:

$$P_a \cdot P_b \cdot (-1)^{L_1+p_1+L_2+p_2} = 1, \tag{3.44}$$

contribute to the two-photon transition amplitude, with P_a, P_b the parities of the initial and final state.

In order to analyze specific two-photon processes the highly non-trivial second-order transition and scattering amplitudes for a number of processes will be evaluated in chapter 4.

3.1.3 Fermi's golden rule and transition probabilities

In the previous section the transition probabilities were discussed for arbitrary short time scales. Especially in highly charged heavy ions atomic processes happen at tremendous speed. Most processes, like the two-photon emission and photon scattering we discuss in this text, are therefore observed long after the actual photon electron interaction has taken place. It is common to describe such processes by means of Fermi's golden rule [30, 31, 32, 43, 47]. In this approach the transition (and for photon scattering also scattering) amplitudes I introduced in the previous sections are used as a building block to evaluate constant transition rates of the processes. These transition rates are the basis for an analysis of all interesting properties of the two-photon processes. In chapter 5 and 6 this approach based on Fermi's golden rule and the transition and scattering amplitudes that will be derived in chapter 4 will be used to evaluate such transition rates directly as well as to derive related properties such as scattering cross-sections.

Fermi's golden rule is obtained from the transition probability (3.34) by considering long time scales i.e. M^2 is considered for $t \to \infty$. It defines a constant transition rate, e.g. for polarized light it is:

$$W_{fi} = 2\pi C^{2n} \left|M_{fi}\right|^2 \delta(E_i + E_{Ph} - E_f)\rho(E_{Ph;sp}), \tag{3.45}$$

with C the prefactor from the interaction Hamiltonian that was removed from the transition amplitudes for convenience, E_i, E_f the energy of the initial and final state, E_{Ph} the total energy of the photon(s), and E_{Ph} the energies of the spontaneously emitted photons. Here we have $n = 1$ for single photon transitions and $n = 2$ for two-photon processes.

As I mentioned before, the energy conservation between the initial and final state (including the total energy of all photons) arises from $K(t)K^*(t)$ for $t \to \infty$. In transition processes in which one or multiple photons are emitted spontaneously, photons are emitted in a continuum of directions. Furthermore, for multi-photon emission the energy of the transition is continually distributed among the photons. It is therefore not sensible to consider the decay into discrete photon states but rather a density of final photon states $\rho(E_{Ph;sp})$ must be defined.
In order to discuss not only total transition rates, but also the angular distributions of the emitted photons, we define state densities $\rho(E_{Ph;sp})$ in an angular differential form. For the spontaneous emission of one or two photons such state densities are given by:

$$\begin{aligned} d\rho_{1Ph}(\omega) =& \frac{\omega V}{2\pi} d\Omega, \\ d\rho_{2Ph}(\omega_1, \omega_2) =& \frac{\omega_1 \omega_2 V^2}{(2\pi)^2} d\Omega_1 d\Omega_2, \end{aligned} \tag{3.46}$$

where the $d\Omega$,Ω_1,Ω_2 are the surface elements of a unit sphere spanned by all possible propagation directions of the emitted photons and $\omega, \omega_1, \omega_2$ their energies. The large but finite volume V will cancel for observable quantities with similar volumes in the denominator of the prefactors (3.36) and in e.g. scattering processes with the volume in the relation between incident photon number and intensity (3.6). This volume is useful to carry along in the calculations as it allows to check if the unit of a certain quantity is correct.

3.2 Ions in static electric fields: time-independent perturbation theory

On top of the influence of dynamic fields we discussed in the first part of this chapter, also external static fields are considered in this thesis. Static electromagnetic fields cause a number of prominent phenomena in atomic physics. Some of the best-known effects are caused by the influence of static external electric fields on the bound electron, and are often called Stark effects. This kind of static electric fields do not only cause shifts in energy levels of ions or atoms, but also changes to the states themselves.

For the Stark effects the external electric fields are much weaker than the typical electric field strength of the nucleus. The effects of such fields can therefore be modeled as small perturbations to the system by means of time-independent perturbation theory.
In this approach we can describe, on the one hand, Stark-induced energy shifts and a splitting of the energies of the states, which occur only for relatively strong electric fields. On the other hand, we have a so-called Stark mixing of the electronic states [48, 49]. The first phenomenon is of no further interest and will only be briefly discussed here (for more details e.g. chapter 14.3 in [36]). My focus lies on the Stark mixing that already plays a role for weaker field strengths. I now introduce its theoretical background, the non-degenerate time-independent perturbation theory.

3.2.1 Time-independent perturbation theory

Time-independent perturbation theory is based on similar assumptions like time-dependent perturbation theory. We decompose the total Hamiltonian of the system into a large part H_0, of which the solutions are known, and a small part λV that depends on some small order parameter λ.

$$H = H_0 + \lambda V. \tag{3.47}$$

The (not normalized) eigenstates of the Hamiltonian H are expressed as a perturbation series $|\psi\rangle = |\psi_0\rangle + \lambda |\psi_1\rangle \cdots$ up to a sufficiently high order of λ.

For example, up to the linear order the perturbed state $|\psi\rangle$ is [30, 32, 36]:

$$|\psi\rangle = |\psi_0\rangle + \sum_{\nu \neq \psi} \frac{\langle \nu | \lambda V | \psi \rangle}{E_\nu - E_\psi} |\nu\rangle , \tag{3.48}$$

where the sum runs over all states $|\nu\rangle$ of the unperturbed system except $|\psi\rangle$.

This so-called non-degenerate approach only works if the energies E_ν of states $|\nu \neq \psi\rangle$ that mix with the original state $|\psi\rangle$ in linear order are different from E_ψ. We can define a condition for the strength of the perturbing Hamiltonian for which such an approach is justified. We only get useful results if:

$$\langle \psi | \lambda V | \nu \rangle < |E_\psi - E_\nu| . \tag{3.49}$$

For stronger perturbations we have to assume that there are some degenerate states with $E_\nu = E_\psi$ and a more complicated perturbation theory for degenerate states has to be used c.p. e.g. [32, 36, 43].

In the non-degenerate theory not only the state but also the eigenenergies of H can be written as a perturbation series $E = E_0 + \lambda E_1 + \cdots$, e.g. the first-order correction to the energy eigenvalues is:

$$\lambda E_1^\psi = \langle \psi | \lambda V | \psi \rangle . \tag{3.50}$$

3.2.2 Ions in static electric fields

We now consider the specific case of perturbation of states of an H-like ion by linear electric fields. With $-\sqrt{\alpha_S}$ the charge of an electron, the perturbation operator for an electric field $\mathbf{F}$ is given by:

$$\lambda V = -\sqrt{\alpha_S} \cdot \mathbf{Fr}. \tag{3.51}$$

In this text we are particularly interested in the effect of relatively weak electric fields on low-lying states of the ion. In order to better define what weak means, we consider the effect of the perturbative contribution on the energy of the states.
For weak fields the energy splitting caused by the Lamb shift are usually enough to fulfill the condition (3.49) and we can use the non-degenerate approach described in the previous section. Under this condition Eq. (3.50) and Eq. (3.51) show that the linear order

perturbation contribution to the energy arises from a matrix element in which parity would not be conserved if it were non-zero. Thus this element must vanish and the energy of the states is in linear order not influenced by the electric field. In this non-degenerate approach the energy perturbation would only become visible in the second order that would lead to a contribution to the energy quadratic in the field strength $\Delta E \propto F^2$. If, however, the electric field were so strong that the condition (3.49) would be broken, we would have the well-known linear F dependence of the energy of the Stark effect known as the linear Stark effect, c.p.[36]. Furthermore, the eigenstates of the ion would need to be replaced by a complete mixture of the degenerate states. In the strong field region the perturbation of the energy of the states has thus a linear F dependence while in the weak field region it is proportional to F^2. I will omit this linear region in the rest of the text and focus on the mixing of the states in the quadratic region.

In the weak field region the dressed states are given by Eq. (3.48). For most unperturbed original states $|\psi\rangle$ of few-electron ions there are usually some other states with very similar energies that contribute to this dressed state. As an example in H-like ions the $2p_{1/2}$ and $2s_{1/2}$ state have the same energy if we describe them by means of relativistic Dirac theory. The energy difference between these states is caused e.g. by Lamb shifts and is usually many orders of magnitude smaller than typical energy differences caused by the fine structure. Since for such states the denominator in Eq. (3.49) becomes very small, the contribution of such a "next neighbor state" $|\psi_{nn}\rangle$ usually dominates Eq. (3.48). As a first estimate it is therefore sufficient to limit the calculation to the next neighbor contribution [48, 49]. In this approach the perturbed states $|\psi_{per}\rangle$ are given by:

$$|\psi_{per}\rangle = |\psi\rangle - \boldsymbol{\eta}\mathbf{F}\,|\psi_{\mathbf{nn}}\rangle\,, \tag{3.52}$$

with the mixing parameter

$$\boldsymbol{\eta} = \frac{\sqrt{\alpha_S}\,\langle\psi_{nn}\,|\mathbf{r}|\,\psi\rangle}{\Delta E_{nn} + i\Gamma/2}. \tag{3.53}$$

Here we used $\Gamma = \Gamma_\psi + \Gamma_{\psi_n n}$ for the combined decay width of the original state and its next neighbor and ΔE_{nn} the difference of their energies which is usually determined by the Lamb shifts of both states.

The unit of the absolute value of the mixing parameter η is the inverse of a field strength. It can thus be used to define a critical field strength F_{max}. At this field strength the condition (3.49) breaks down and the electric field can no longer be considered small. The critical field strength is given by:

$$F_{max} = \left|\frac{\Delta E_{nn} + i\Gamma/2}{\sqrt{\alpha_S}\,\langle\psi_{nn}\,|-\mathbf{r}|\,\psi\rangle}\right|. \tag{3.54}$$

It is very useful as a natural scale for the field strength to discuss the effects caused by the linear field perturbations and it will be used in chapter 5.

To determine the mixing parameter η and the critical field strength for specific states of H- and He-like ions I evaluate in the next section the mixing matrix elements $\langle\psi_{nn}\,|\mathbf{Fr}|\,\psi\rangle$.

The relativistic mixing matrix elements for H- and He-like states

The mixing matrix elements $\langle \psi_{nn} | \mathbf{Fr} | \psi \rangle$ can be most conveniently evaluated in a specific coordinate system in which the electric field $\mathbf{F}$ is parallel to the quantization axis. In this coordinate system it is possible to simplify the field operator:

$$-\mathbf{Fr} = -Fr\sqrt{\frac{4\pi}{3}}Y_{10}(\Omega_{\mathbf{r}}). \tag{3.55}$$

Using this simplified operator for H-like states the mixing matrix element can be easily written as, c.p. [12]:

$$\langle \psi_{nn} | -Fz | \psi \rangle = \langle -\kappa_{\psi_{nn}} | Y_{10} | -\kappa_{\psi} \rangle \cdot K_{ab}^{-} + \langle \kappa_{\psi_{nn}} | Y_{10} | \kappa_{\psi} \rangle \cdot K_{ab}^{+}, \tag{3.56}$$

with angular integrals given by:

$$\begin{aligned}\langle \kappa_{\psi_{nn}} | Y_{10} | \kappa_{\psi} \rangle =& \sqrt{\frac{3(2l_{\psi_{nn}}+1)}{4\pi(2l_{\psi}+1)}} \langle l_{\psi_{nn}} 0, 10 \mid l_{\psi} 0 \rangle \\ & \times \sum_{m_{l_{\psi_{nn}}}, m_{s_{\psi}}} \left\langle l_{\psi_{nn}} m_{l_{\psi_{nn}}}, s_{\psi} m_{s_{\psi}} \mid j_{\psi_{nn}} m_{j_{\psi_{nn}}} \right\rangle \\ & \times \left\langle l_{\psi} m_{l_{\psi}}, s_{\psi} m_{s_{\psi}} \mid j_{\psi} m_{j_{\psi}} \right\rangle \left\langle l_{\psi_{nn}} m_{l_{\psi_{nn}}}, 10 \mid l_{\psi} m_{l_{\psi_{nn}}} \right\rangle, \end{aligned} \tag{3.57}$$

with j, l, s the total angular momentum, the orbital angular momentum, and the spin of the H-like state and the ms their projections on the quantization axis.

The radial parts in Eq. (3.56) are given by:

$$\begin{aligned} K_{ab}^{\pm} = N_b N_a & \sum_{k=0}^{n_b - |\kappa_b|} \sum_{k'=0}^{n_a - |\kappa_a|} c_{b;k}^{\pm} c_{a;k'}^{\pm} \beta_b^{\gamma_b - 1 + k} \beta_a^{\gamma_a - 1 + k'} \\ & \times (\beta_b + \beta_a)^{-\gamma_b - \gamma_a - k - k' - 2} \Gamma(\gamma_b + \gamma_a + k + k' + 2). \end{aligned} \tag{3.58}$$

Here we used the constants of our solution for the H-like states from chapter 2, c.p. Eq. (2.18). The "+"-constants originate from the large part of spinors and "-"-constants from small part.

The angular parts of the mixing matrix element (3.57) show that in our coordinate system only states a,b with $l_a - l_b = \pm 1$, $m_{j_a} - m_{j_b} = 0$, and $m_{s_a} - m_{s_b} = 0$ mix. We also have the (for H-like ions) trivial condition that the spin of the state (and its projection) must not change $s_a - s_b = 0$. Apart from the energy these conditions determine what the relevant "next neighbor" of an unperturbed state is and potentially select the magnetic substate of these next neighbor states.

In the independent particle model the mixing matrix elements for H-like ions can be used as building blocks to construct mixing matrix elements for He-like ions. The He-like matrix element are evaluated by coupling the total angular momentum j_s of the spectator electron with the angular momenta of the unperturbed state j_{ψ} and its next neighbor $j_{\psi_{nn}}$ to get

the total angular momenta J_ψ and $J_{\psi_{nn}}$ of the original He-like state and its next neighbor state:

$$\left\langle \psi_{nn,He} \left| \sum_{i=1,2} -Fz_i \right| \psi_{He} \right\rangle = \sum_{m_1,m_2} \langle j_s m_1, j_\psi m_2 \mid J_\psi M_\psi \rangle \langle j_s m_1, j_{\psi_{nn}} m_2 \mid J_{\psi_{nn}} M_{\psi_{nn}} \rangle \times \langle \psi_{nn} | -Fz | \psi \rangle \,, \tag{3.59}$$

where (because of the indistinguishability of the electrons) we have to include the space operators z_i for both electrons and the Ms are the projections of the total (He-like) angular momenta on the quantization axis. In He-like systems similar conditions on the mixing matrix element for the orbital angular momentum of the acting electron, the projection of the total angular momentum and the total spin of the He-like state are inherited from the H-like case.

In the non-relativistic limit the expression (3.56) for H-like systems coincides with previous results [48, 49]. Furthermore, in this limit Eq. (3.59) also agrees with similar results in [50].

4 Transition amplitudes of two-photon processes

As I showed in chapter 3, atomic processes involving a simultaneous interaction of an ion with two photons can be described by means of second-order perturbation theory. It was presented how the properties of such processes can be traced back to second-order transition or scattering amplitudes. We furthermore showed that it is sufficient to consider such amplitudes under the assumption that the photons that interact with the ion are circularly polarized. Transition rates and scattering cross-sections for other polarizations can be constructed from these elements using the polarization expansion parameters we defined in Eq. (3.17). In this chapter we discuss the derivation of such transition and scattering amplitudes for circularly polarized photons in detail. I focus on the one hand on the amplitude of two-photon decay in which an initial excited state decays into a lower lying state by simultaneous emission of two photons. On the other hand the photon scattering amplitudes that can be used to describe both elastic as well as inelastic scattering are considered.

The amplitudes for all of these processes have a very similar structure. In their evaluation we utilize the definitions of the H- and He-like spinors (2.7) and (2.24) as well as multipole decomposition of the emission and absorption operators for circular polarized photons with helicity λ defined in Eq. (3.10) and Eq. (3.11). With these definitions is is possible to separate the angular dependent parts from the angular independent parts of the amplitudes and to evaluate them separately. In the first part of this chapter we present an approach to perform such a separation previously used, e.g. in [9, 42, 51, 52]. With this method the radial integrations are traced back to the evaluation of the so-called reduced matrix elements of two-photon absorption. In the second part of this chapter I discuss a basic analytic method, c.p. [12], for evaluating these reduced matrix elements in detail. Furthermore, I examine the limitations of this analytic solution and briefly discuss advanced methods [6, 53] that allow us to go beyond these limitations.

4.1 Transition amplitude of two-photon processes

I begin the discussion of the transition amplitudes of two-photon processes by evaluating the matrix elements for two-photon decay. In this calculation I first separate the angular parts of the calculations from the radial parts by means of the Wigner-Eckart theorem. The Wigner-Eckart theorem introduces so-called reduced matrix elements that contain the complex radial integrations and will be discussed in the second part of this chapter. As a second step the angular parts are simplified. Using the symmetry properties of the reduced matrix elements the scattering amplitudes can be described in a similar way.

4.1.1 The two-photon decay amplitude for H-like and He-like ions

The separation of the angular dependent parts has the same structure for two-photon decay in H-like as well as He-like ions. It is therefore very convenient to discuss it in terms of general multi-electron states $|\alpha JM\rangle$. In these states the Js and the Ms are the total angular momenta and their projections, i.e. the J,j and M, m for states of He-like and H-like ions. The α are an abbreviation for the principal quantum number and the orbital angular momentum or the parity of the states , i.e. N, P for states of He-like ions and n,l for states of H-like ions, c.p. chapter 2. Likewise we use the emission $R^{1,2\,\dagger}_{\lambda}(\mathbf{k})$ operators and their multipole components both for single- as well as two-electron systems, c.p. chapter 3. Here λ is the helicity of the emitted photon and $\mathbf{k}$ its wave vector.

In two-photon decay both photons are emitted simultaneously. Since the photons are indistinguishable, the transition amplitude must be symmetric with respect to the photon number, i.e. we need to include both possible decay paths: the one where "first" photon 1 is emitted and then photon 2 and the one where this order is reversed. For a two-photon decay of the initial state $|\alpha_i J_i M_i\rangle$ into the final state $|\alpha_f J_f M_f\rangle$ such an amplitude is given by:

$$\begin{aligned} M_{fi} = &\sum_{\alpha_\nu J_\nu M_\nu} \frac{\left\langle \alpha_f J_f M_f \left| R^{1,2\,\dagger}_{\lambda_1}(\mathbf{k}_1) \right| \alpha_\nu J_\nu M_\nu \right\rangle \left\langle \alpha_\nu J_\nu M_\nu \left| R^{1,2\,\dagger}_{\lambda_2}(\mathbf{k}_2) \right| \alpha_i J_i M_i \right\rangle}{E_i - \omega_2} \\ &+ \sum_{\alpha_\nu J_\nu M_\nu} \frac{\left\langle \alpha_f J_f M_f \left| R^{1,2\,\dagger}_{\lambda_2}(\mathbf{k}_2) \right| \alpha_\nu J_\nu M_\nu \right\rangle \left\langle \alpha_\nu J_\nu M\nu \left| R^{1,2\dagger}_{\lambda_1}(\mathbf{k}_1) \right| \alpha_i J_i M_i \right\rangle}{E_i - \omega_1}. \end{aligned} \tag{4.1}$$

Here E_i is the energy of the initial state and the $\mathbf{k}_{1,2}, \lambda_{1,2}, \omega_{1,2}$ are the wave vectors, helicities, and energies of the photons.

In order to be able to use the Wigner-Eckart theorem, which allows us to separate the direction-dependent parts of the matrix elements of a tensor operator from its direction-independent parts, we must consider matrix elements with an operator that depends on a single angular momentum and its projection. As I showed in chapter 3, the emission operators $R^{1,2\,\dagger}_{\lambda}(\mathbf{k})$ can be expanded into operators of this kind, the multipole components $\mathbf{a}^{(p)}_{LM}$. With the expansion of the interaction operators from Eq. (3.12) the two-photon decay matrix can be written as:

$$\begin{aligned} M_{fi} =& 2\pi \sum_{p_1 L_1 p_2 L_2} \sum_{M_1 M_2} (-i)^{L_1+L_2} (-i\lambda_1)^{p_1} (-i\lambda_2)^{p_2} \left[L_1, L_2\right]^{1/2} D^{L_1\,*}_{M_1 \lambda_1}(\Omega_{\mathbf{k}_1}) D^{L_2\,*}_{M_2 \lambda_2}(\Omega_{\mathbf{k}_2}) \\ &\times \Bigg(\sum_{\alpha_\nu J_\nu M_\nu} \frac{\left\langle \alpha_f J_f M_f \left| \sum_a \boldsymbol{\alpha}_a \mathbf{a}^{\dagger\,(p_1)}_{L_1\,M_1} \right| \alpha_\nu J_\nu M_\nu \right\rangle \left\langle \alpha_\nu J_\nu M_\nu \left| \sum_a \boldsymbol{\alpha}_a \mathbf{a}^{\dagger\,(p_2)}_{L_2\,M_2} \right| \alpha_i J_i M_i \right\rangle}{E_i - \omega_2 - E_\nu} \\ &+ \sum_{\alpha_\nu J_\nu M_\nu} \frac{\left\langle \alpha_f J_f M_f \left| \sum_a \boldsymbol{\alpha}_a \mathbf{a}^{\dagger\,(p_2)}_{L_2\,M_2} \right| \alpha_\nu J_\nu M_\nu \right\rangle \left\langle \alpha_\nu J_\nu M_\nu \left| \sum_a \boldsymbol{\alpha}_a \mathbf{a}^{\dagger\,(p_1)}_{L_1\,M_1} \right| \alpha_i J_i M_i \right\rangle}{E_i - \omega_1 - E_\nu} \Bigg), \end{aligned} \tag{4.2}$$

where we used the abbreviation $[a, b, \cdots] = (2a+1)(2b+1)\cdots$ and the index a is 1 for H-like ions and runs from 1 to 2 for He-like ions and the p, L, $\Omega_{\mathbf{k}}$ are defined like in chapter 3.

At this point the Wigner-Eckart theorem (c.p. A.62 in [35]) can be employed and the matrix elements $\left\langle \alpha_f J_f M_f \left| \sum_a \boldsymbol{\alpha}_a \mathbf{a}^{(p)}_{LM} \right| \alpha_i J_i M_i \right\rangle$ can be written as products of Clebsch-Gordan coefficients and factors that do not depend on a particular reference frame, the so-called reduced transition matrices. In a naive approach evaluating the transition amplitude would require to derive the reduced matrix elements for two-photon decay. Alternatively these reduced matrix elements for two-photon decay can be traced back to the better-known reduced elements for the two-photon absorption. I will show in the second part of this chapter that a reduced two-photon emission matrix element can be written as a product of the corresponding two-photon absorption element and the prefactor $(-1)^{L_1+L_2}$. With this symmetry the final two-photon emission amplitude is given by:

$$\begin{aligned} M_{fi} =& 2\pi \sum_{p_1 L_1 p_2 L_2} \sum_{M_1 M_2} i^{L_1+L_2} (-i\lambda_1)^{p_1} (-i\lambda_2)^{p_2} \left[L_1, L_2\right]^{1/2} D^{L_1\,*}_{M_1\lambda_1}(\Omega_{\mathbf{k}_1}) D^{L_2\,*}_{M_2\lambda_2}(\Omega_{\mathbf{k}_2}) \\ & \times \sum_{J_\nu M_\nu} \left[J_f, J_\nu\right]^{-1/2} \Big(\left\langle J_\nu M_\nu, L_1 M_1 \mid J_f M_f \right\rangle \left\langle J_i M_i, L_2 M_2 \mid J_\nu M_\nu \right\rangle S^{L_1 p_1 L_2 p_2}_{J_\nu}(-\omega_2) \\ & + \left\langle J_\nu M_\nu, L_2 M_2 \mid J_f M_f \right\rangle \left\langle J_i M_i, L_1 M_1 \mid J_\nu M_\nu \right\rangle S^{L_2 p_2 L_1 p_1}_{J_\nu}(-\omega_1) \Big). \end{aligned} \tag{4.3}$$

Here we introduced the reduced matrix elements for two-photon absorption:

$$S^{L_1 p_1 L_2 p_2}_{J_\nu}(-\omega_2) = \sum_{\alpha_\nu} \frac{\left\langle \alpha_f J_f \left|\left| \sum_a \boldsymbol{\alpha}_a \mathbf{a}^{(p_1)}_{L_1} \right|\right| \alpha_\nu J_\nu \right\rangle \left\langle \alpha_\nu J_\nu \left|\left| \sum_a \boldsymbol{\alpha}_a \mathbf{a}^{(p_2)}_{L_2} \right|\right| \alpha_i J_i \right\rangle}{E_i - \omega_2 - E_\nu}. \tag{4.4}$$

In Eq. (4.3) the "virtual intermediate" angular momenta J_ν and their projections M_ν are determined by the well-known triangle rules for angular momenta in Clebsch-Gordan coefficients, c.p. [35]. For a non-zero contribution, e.g. to the first part of the sum in Eq. (4.3), the angular momenta J_ν have to fulfill the condition $|J_f - L_1| \leq J_\nu \leq J_f + L_1$ and $|J_i - L_2| \leq J_\nu \leq J_i + L_2$. In general this internal structure is not well visible in most two-photon processes. In chapter 6 I discuss a case where transitions via intermediate states with specific angular momenta are enhanced and such triangle rules have a visible influence on the transition properties.

4.1.2 Scattering amplitudes

Photon scattering can be described as a second-order process in which simultaneously one photon is absorbed and one is emitted. The scattering amplitudes of such a process can in principle be handled in complete analogy to the preceding paragraph. This approach would however require the evaluation of reduced scattering amplitudes. As the evaluation of such reduced elements is non-trivial, it is more intelligent to use the symmetries of the reduced transition amplitude of single photon transitions to express the scattering amplitude in terms of reduced matrix elements for two-photon absorption. In order to implement such methods, we first discuss the symmetry properties of the reduced matrix elements for single photon transitions. As in this thesis only the scattering of photons by H-like ions is considered, we simplify the calculation by focusing only on such ions. Like in chapter 2 the bound states of such ions are determined by the quantum numbers n, l, j, m and we use the one-electron absorption or emission operators.

Symmetry of single photon reduced matrix elements

For the upcoming calculations we need to understand the behavior of the reduced matrix element for single photon absorption under complex conjugation. It can most easily be determined by considering an explicit solution for such a reduced element. For H-like ions such single-photon reduced matrix elements can be found in the literature [1, 54]. For example an explicit form is [1]:

$$\left\langle n_a l_a j_a \left|\left| \boldsymbol{\alpha} \mathbf{a}_L^{(p)} \right|\right| n_b l_b j_b \right\rangle = \frac{1+(-1)^{l_a+l_b+L+p+1}}{2} \sqrt{2j_a+1}\, \langle j_a 1/2, L0 \mid j_b 1/2\rangle\, \overline{M}^p_{ab}, \quad (4.5)$$

with the quantum numbers for the H-like states $n_{a/b}, j_{a,b}, l_{a,b}$, and $\kappa_{a,b}$ from chapter 2. The L, p, k define the multipole order of the transition and the length of its wave vector.

The expressions $\overline{M}^p_{ab}$ are given by:

$$\overline{M}^{(p=0)}_{ab} = \frac{-i}{\sqrt{4\pi}} \sqrt{\frac{2L+1}{L(L+1)}} (\kappa_a + \kappa_b) I^+_L(k;a,b), \quad (4.6)$$

$$\begin{aligned} \overline{M}^{(p=1)}_{ab} =& \frac{i}{\sqrt{4\pi}} \Big(\sqrt{\frac{L}{(L+1)(2L+1)}} \left[(\kappa_a - \kappa_b) I^+_{L+1}(k;a,b) + (L+1) I^-_{L+1}(k;a,b) \right] \\ & - \sqrt{\frac{L+1}{L(2L+1)}} \left[(\kappa_a - \kappa_b) I^+_{L-1}(k;a,b) - L I^-_{L-1}(k;a,b) \right] \Big), \end{aligned} \quad (4.7)$$

$$(4.8)$$

with the radial integrals:

$$I^\pm_L(k;a,b) = \int_0^\infty \left(g_a(r) f_b(r) \pm g_b(r) f_a(r) \right) j_L(kr) r^2 dr, \quad (4.9)$$

where the $g(r), f(r)$ are the large and small radial parts of the spinor (2.7).

To establish possible symmetries I now explore how the parts of Eq. (4.5) react to complex conjugation. As a first step we see from Eq. (4.8) and Eq. (4.9):

$$\left(\overline{M}^{(p)}_{ab} \right)^* = (-1)^{p+1} \overline{M}^{(p)}_{ba}, \quad (4.10)$$

while the prefactors in Eq. (4.5) do not change.

Finally I use this observation and the symmetry properties of Clebsch-Gordan coefficients (c.p. [35]) and find the following symmetry:

$$\left(\left\langle n_a l_a j_a \left|\left| a^{(p)}_L \right|\right| n_b l_b j_b \right\rangle \right)^* = (-1)^{p+1+j_b-j_a} \left\langle n_b l_b j_b \left|\left| a^{(p)}_L \right|\right| n_a l_a j_a \right\rangle. \quad (4.11)$$

By means of an IPM approach it is not difficult to show that a similar symmetry would be also true in He-like systems.

The scattering amplitude

In a scattering process there is both an absorption of a photon (defined by $\mathbf{k}_1, \lambda_1, \omega_1$) and an emission of a photon (defined by $\mathbf{k}_2, \lambda_2, \omega_2$). I evaluate the scattering amplitude by using the fact that the emission operator is the complex conjugate of the absorption operator. Using the well-known relation between a matrix element of an operator A and the matrix element of its Hermitian adjoined operator $\langle b\,|A|\,a\rangle = (\langle a\,|A^\dagger|\,b\rangle)^*$ the scattering amplitude with an initial state $|n_i l_i j_i m_i\rangle$ and a final state $|n_j l_f j_f m_f\rangle$ can be written in the following form:

$$M_{fi}^{sc} = \sum_{n_\nu l_\nu j_\nu m_\nu} \left(\frac{\left(\langle n_\nu l_\nu j_\nu m_\nu \left| R^1_{\lambda_2}(\mathbf{k}_2)\right| n_f l_f j_f m_f\rangle\right)^* \langle n_\nu l_\nu j_\nu m_\nu \left| R^1_{\lambda_1}(\mathbf{k}_1)\right| n_i l_i j_i m_i\rangle}{E_i + \omega_1 - E_\nu} \right.$$
$$\left. + \frac{\langle n_f l_f j_f m_f \left| R^1_{\lambda_1}(\mathbf{k}_1)\right| n_\nu l_\nu j_\nu m\nu\rangle \left(\langle n_i l_i j_i m_i \left| R^1_{\boldsymbol{\lambda}_2}(\mathbf{k}_2)\right| n_\nu l_\nu j_\nu m_\nu\rangle\right)^*}{E_i - \omega_2 - E_\nu} \right). \tag{4.12}$$

To evaluate this expression it is useful to consider a multipole decomposition of the single photon transition matrices in the Eq. 4.12 by means of (3.12).
With this expansion and the Wigner-Eckart theorem the single photon transition matrix elements are given by:

$$\langle n_\nu l_\nu j_\nu m_\nu \left| R^1_{\lambda_1}(\Omega_{\mathbf{k}_1})\right| n_i l_i j_i m_i\rangle = \frac{\sqrt{2\pi}}{\sqrt{2j_i+1}} \sum_{p_1 L_1 M_1} \sqrt{2L_1+1}\, i^{L_1} (i\lambda_1)^{p_1} D^{L_1}_{M_1 \lambda_1}(\Omega_{\mathbf{k}_1})$$
$$\times \langle j_i m_i, L_1 M_1 \mid j_\nu m_\nu\rangle \left\langle n_\nu l_\nu j_\nu \left|\left| \boldsymbol{\alpha} \mathbf{a}^{(p_1)}_{L_1} \right|\right| n_i l_i j_i \right\rangle. \tag{4.13}$$

This decomposition of the single photon absorption amplitude allows us to rewrite Eq. (4.12) into the following from:

$$M_{fi}^{sc} = 2\pi^2 \sum_{L_1 p_1 L_2 p_2} [L_1, L_2]^{1/2}\, i^{L_1 - L_2} (i\lambda_1)^{p_1} (-i\lambda_2)^{p_2} \sum_{M_1 M_2} D^{L_1}_{M_1 \lambda_1}(\Omega_{\mathbf{k}_1}) D^{L_2\,*}_{M_2 \lambda_2}(\Omega_{\mathbf{k}_2})$$
$$\times \sum_{j_\nu m_\nu} \left((2j_\nu + 1)^{-1} \langle j_i m_i, L_1 M_1 \mid j_\nu m_\nu\rangle \langle j_f m_f, L_2 M_2 \mid j_\nu m_\nu\rangle \right.$$
$$\times \sum_{n_\nu l_\nu} \frac{\left(\left\langle n_\nu l_\nu j_\nu \left|\left| \boldsymbol{\alpha} \mathbf{a}^{(p_2)}_{L_2} \right|\right| n_f l_f j_f \right\rangle\right)^* \left\langle n_\nu l_\nu j_\nu \left|\left| \boldsymbol{\alpha} \mathbf{a}^{(p_1)}_{L_1} \right|\right| n_i l_i j_i \right\rangle}{E_i + \omega_1 - E_\nu}$$
$$+ [j_f, j_i]^{-1/2} \langle j_\nu m_\nu, L_1 M_1 \mid j_f m_f\rangle \langle j_\nu m_\nu, L_2 M_2 \mid j_i m_i\rangle$$
$$\left. \times \sum_{n_\nu l_\nu} \frac{\left\langle n_f l_f j_f \left|\left| \boldsymbol{\alpha} \mathbf{a}^{(p_1)}_{L_1} \right|\right| n_\nu l_\nu j_\nu \right\rangle \left(\left\langle n_i l_i j_i \left|\left| \boldsymbol{\alpha} \mathbf{a}^{(p_2)}_{L_2} \right|\right| n_\nu l_\nu j_\nu \right\rangle\right)^*}{E_i - \omega_2 - E_\nu} \right). \tag{4.14}$$

By using the symmetry of the reduced matrix element under complex conjugations (4.11) the complicated sums of reduced matrix element expressions in Eq. (4.14) can be traced back to the reduced matrix elements of two-photon absorption and we finally have:

$$\begin{aligned} M_{fi}^{sc} =& 2\pi \sum_{p_1 L_1 p_2 L_2} \sum_{M_1 M_2} (-1)^{p_2+1} (-i)^{L_1-L_2} (i\lambda_1)^{p_1} (-i\lambda_2)^{p_2} \\ & \times [L_1, L_2]^{1/2} \, D^{L_1}_{M_1 \lambda_1}(\Omega_{\mathbf{k}_1}) D^{L_2 *}_{M_2 \lambda_2}(\Omega_{\mathbf{k}_2}) \\ & \times \sum_{j_\nu m_\nu} \big((2j_\nu + 1)^{-1} (-1)^{j_f - j_\nu} \langle j_f m_f, L_2 M_2 \mid j_\nu m_\nu \rangle \\ & \times \langle j_i m_i, L_1 M_1 \mid j_\nu m_\nu \rangle \, S^{L_2 p_2 L_1 p_1}_{j_\nu}(+\omega_1) \\ & + [j_f, j_i]^{-1/2} \, (-1)^{j_\nu - j_i} \langle j_\nu m_\nu, L_1 M_1 \mid j_f m_f \rangle \\ & \times \langle j_\nu m_\nu, L_2 M_2 \mid j_i m_i \rangle \, S^{L_1 p_1 L_2 p_2}_{j_\nu}(-\omega_2) \big). \end{aligned} \tag{4.15}$$

This photon scattering amplitude (4.15) has many similarities with the two-photon decay amplitude (4.3). The angular momenta are coupled in the same way and the angular momenta of the intermediate states fulfills similar conditions as the angular momenta of the intermediate states in two-photon decay. However, by comparing the amplitudes we can see that in contrast to the two-photon decay amplitude the scattering amplitude is not symmetric with respect to the photon numbers. The asymmetry is caused by the fact that in the scattering process both photon absorption as well as emission contribute. In the different reduced matrix elements in Eq. (4.15) the photons have therefore energies with an opposite sign.

It should be mentioned that there are other representations of the angular dependent part of such scattering and decay amplitudes. For example, in [55, 56] an approach based on irreducible tensors was used. While such a irreducible tensor representation can be somewhat more compact and it is useful to determine the non-relativistic limit of the scattering amplitude, the approach presented here is better suitable to evaluate numerical approximations of such elements and somewhat easier to understand for an interpretation of the results.

4.2 The reduced matrix elements for two-photon absorption

By introducing the reduced matrix elements in the first part of this chapter, I was able to separate the non-trivial radial integrations from angular and polarization dependent parts. The evaluation of such elements involves a summation over the complete spectrum of the ion, as can be seen from the definition (4.4). This spectrum includes the well-known discrete part I showed in chapter 2, the continuum of states with positive energy that corresponds to unbound electrons and in a relativistic theory also a continuum of states with negative energy. It has been shown that all these contributions play an important role for the second-order amplitude. For example Akhiezer proved [47] that in the non-relativistic limit a separate quadratic electromagnetic interaction operator arises from the contributions of

the negative continuum. This part is sometimes called the Seagull term and is especially important for two-photon processes with the same initial and final state, such as elastic photon scattering.

Over the years a number of methods have been developed to deal with the infinite sum in Eq. (4.4). While in some earlier works [7, 13, 57] direct summation of a finite number of intermediate states and similar finite approximations were popular, nowadays mostly numeric finite base methods [6, 9, 58, 59] and Greens function bases approaches [4, 22, 52] are used. In this thesis I focus mostly on Greens function based methods. Specifically, most results were evaluated using an analytic solution of reduced matrix elements for two-photon absorption in H-like system based on the Sturmian representation of the Dirac-Coulomb-Greens function [56, 60]. I discuss this approach and its limitations in detail.
Following this discussions more advanced Greens function-based methods as well as numerical methods based on a finite number of B-polynomials and B-splines are presented that overcome these limitations. Such reduced matrix elements evaluated by Vladimir Yerokhin were used in our study of the elastic photon scattering process.
Finally I briefly show that these results for H-like ions can be generalized to He-like ions using an independent particle model.

4.2.1 Dirac Coulomb Greens function approach: an analytic solution

The Sturmian representation of the Dirac Coulomb Greens function

In order to evaluate the sum in the definition (4.4), as a first step it is useful to return to the full transition amplitude (4.1). In this amplitude there is a sum over all intermediate states ν. We can combine this sum with all other expressions in Eq. (4.1) that depend on the intermediate states and define a so-called Greens operator. For H-like ions it is:

$$\hat{G}(E) = \sum_{n_\nu l_\nu j_\nu m_\nu} \frac{|n_\nu l_\nu j_\nu m_\nu\rangle \langle n_\nu l_\nu m_\nu j_\nu|}{E - E_\nu}. \tag{4.16}$$

Such Greens operators are best known by the position representation of their matrix elements $G(r, r'; E) = \langle r| \hat{G}(E) |r'\rangle$. This representation is known as the Greens function of the system. It is the solution to a fundamental differential equation that is in the case of a relativistic H-like ion:

$$(H_D - E)G(\mathbf{r}, \mathbf{r}'; E) = \delta(\mathbf{r}, \mathbf{r}'), \tag{4.17}$$

with the Hamilton operator $H_D = \beta + \boldsymbol{\alpha}\mathbf{p} - \frac{Z\alpha_S}{r}$ from Eq. (2.6) and the two space coordinates $\mathbf{r}, \mathbf{r}'$.

For quantum mechanical systems the function $G(r, r'; E)$ has a simple interpretation: It describes the propagation of an electron in the electric field of the nucleus. To derive this propagator we need to solve Eq. (4.17). For relativistic H-like ions with a point-like infinitely heavy nucleus several solutions are known. In all of these solutions the Greens function is

written as a sum of Greens function components that depend only on specific intermediate angular momentum j_ν and its projection m_ν:

$$G(\mathbf{r},\mathbf{r}';E) = \sum_{j_\nu l_\nu m_\nu} G^{m_\nu}_{j_\nu,l_\nu}(\mathbf{r},\mathbf{r}';E). \tag{4.18}$$

Like the spinor for H-like states (2.7), the components $G^{m_\nu}_{j_\nu,l_\nu}$ can be written as four 2x2-component expressions that have radial and angular parts:

$$G^{m_\nu}_{j_\nu,l_\nu}(\mathbf{r},\mathbf{r}';E) = \begin{pmatrix} g^{11}_{\kappa_\nu}(r,r';E)\chi^{m_\nu}_{\kappa_\nu}(\Omega_\mathbf{r})\chi^{m_\nu\,\dagger}_{\kappa_\nu}(\Omega_{\mathbf{r}'}) & ig^{12}_{\kappa_\nu}(r,r';E)\chi^{m_\nu}_{\kappa_\nu}(\Omega_\mathbf{r})\chi^{m_\nu\,\dagger}_{-\kappa_\nu}(\Omega_{\mathbf{r}'}) \\ -ig^{21}_{\kappa_\nu}(r,r';E)\chi^{m_\nu}_{-\kappa_\nu}(\Omega_\mathbf{r})\chi^{m_\nu\,\dagger}_{\kappa_\nu}(\Omega_{\mathbf{r}'}) & g^{22}_{\kappa_\nu}(r,r';E)\chi^{m_\nu}_{-\kappa_\nu}(\Omega_\mathbf{r})\chi^{m_\nu\,\dagger}_{-\kappa_\nu}(\Omega_{\mathbf{r}'}) \end{pmatrix}, \tag{4.19}$$

where we have two of the same two-component angular parts $\chi^{m_\nu}_{\kappa_\nu}(\Omega_\mathbf{r})$ as in Eq. (2.7) and four radial parts $g^{IJ}_{\kappa_\nu}(r,r';E)$ and we reintroduced the $\kappa = \kappa(j,l)$ quantum number from chapter 2 that is connected to the orbital and total angular momentum by Eq. (2.12).

For the radial part several solutions have been found. We here utilized a Sturmian representation of the radial parts, c.p. [34, 61, 62]. These kind of solutions are obtained by first inserting (4.18) and (4.19 into (4.17). By clever algebraic manipulations of the resulting radial equations these equations can be traced back to the so-called Sturm-Lioville differential equation. Thus the radial parts can be constructed from the solutions of this Sturm-Lioville equation. These lengthy derivations go beyond the scope of this thesis and can be found e.g. in [12, 34].

For my purpose it is sufficient to know the results. According to Hylton et. al. [62] the solutions for the radial Greens function are:

$$\begin{aligned} g^{ij}_\kappa(r,r';E) = {} & 2p(2pr2pr')^{\gamma-1}\exp(-p(r+r')) \\ & \times A^{ij}\sum_{n=0}^{\infty}\sum_{q=0}^{3} C^{ij}_{nq} L^{\alpha_q}_n(2pr) L^{\alpha'_q}_n(2pr'). \end{aligned} \tag{4.20}$$

with $L^\alpha_n(x)$ the generalized Laguerre polynomials and the following constants:

$$A^{ij} = \begin{cases} (1+E), i=j \\ \sqrt{1-E^2}, i\neq j \end{cases}, \tag{4.21}$$

$$C^{ij}_{nq} = \begin{cases} \frac{(\kappa+\nu/E)n!}{\Gamma(2\gamma+1+n)(n+\gamma+1-\nu)} & q=0 \\ \frac{(\kappa-\nu/E+(-1)^{j-1}2(\gamma+\nu))n!}{\Gamma(2\gamma+1+n)(n+\gamma-\nu)} & q=1, i=j \\ \frac{(\kappa-\nu/E)n!}{\Gamma(2\gamma+1+n)(n+\gamma-\nu)} & q=1, i\neq j \\ \frac{(-1)^{j-1}n!}{\Gamma(2\gamma+n)(n+\gamma-\nu)} & q=2,3 \end{cases}, \tag{4.22}$$

$$\alpha_2 = \alpha'_3 = 2\gamma-1, \qquad \alpha_q = \alpha'_q = 2\gamma \text{ for all other q.} \tag{4.23}$$

In these expressions the abbreviations $\gamma = \sqrt{\kappa^2-(Z\alpha_S)^2}$, $p = \sqrt{1-E^2}$ and $\nu = Z\alpha_S E/p$ are used.

Analytic solution for the reduced two-photon absorption matrix element

The Sturmian representation of the Dirac-Coulomb Greens function can be used to evaluate an analytic solution for the reduced two-photon absorption matrix elements for H-like ions. As such derivations have been discussed in depth in the literature [4, 12, 52], I will here only show the main steps.
The derivation starts with the two-photon absorption amplitude. By including the definition of the Greens operator (4.16) the amplitude for a transition between the state $|n_i l_i j_i m_i\rangle$ and the state $|n_f l_f j_f m_f\rangle$ can be written in analogy to Eq. (4.1) as:

$$\begin{aligned} M_{fi} = &\left\langle n_f j_f l_f m_f \left| R^1_{\lambda_1}(\mathbf{k}_1) G(E_i + \omega_2) R^1_{\lambda_2}(\mathbf{k}_2) \right| n_i j_i l_i m_i \right\rangle \\ &+ \left\langle n_f j_f l_f m_f \left| R^1_{\lambda_2}(\mathbf{k}_2) G(E_i + \omega_1) R^1_{\lambda_1}(\mathbf{k}_1) \right| n_i j_i l_i m_i \right\rangle . \end{aligned} \tag{4.24}$$

This amplitude models the absorption of two photons with helicities λ_1, λ_2 and wave vectors $\mathbf{k}_1, \mathbf{k}_2$. As I mentioned in the preceding paragraph, between the absorbtions the propagation of the electron is described by a Greens operator (or in its space representation by a Greens function) that depends on the energy of the initial state E_i and the absorbed photons ω_1, ω_2. Like in chapter 3 I call the first matrix element of Eq. (4.24) M_{12} and the second one M_{21}. For symmetry reasons it is here sufficient to discuss the evaluation of M_{12}.

In my discussion in the preceding paragraph I showed that the Greens function can be written as a 2x2 matrix of 2x2-component expressions. In the evaluation of the matrix elements (4.24) there are contributions from the four components of the Greens function that are each combined with one large or small part of spinor of both the initial and final state of the ion. The matrix element M_{12} can be written as a sum of these contributions from the different entries of the two-component matrices (IJ), i.e. we have $M_{12} = M^{11}_{12} + M^{12}_{12} + M^{21}_{12} + M^{22}_{12}$. By utilizing the multipole expansion (3.12) of the photon absorption operators, e.g. the contribution of the small components $f(r)\chi^m_{-\kappa}(\Omega)$ of both the initial and final spinor, c.p. Eq. (2.7), can be written as:

$$\begin{aligned} M^{11}_{12} = &2\pi \sum_{L_1 p_1 L_2 p_2} [L_1, L_2]^{1/2} \, i^{L_1+L_2} (i\lambda_1)^{p_1} (i\lambda_2)^{p_2} \sum_{M_1 M_2} D^{L_1}_{M_1 \lambda_1}(\Omega_{\mathbf{k}_1}) D^{L_2}_{M_2 \lambda_2}(\Omega_{\mathbf{k}_2}) \\ &\times \sum_{\kappa_\nu m_\nu} \int\int f_f(r) \chi^{m_f}_{-\kappa_f}(\Omega_{\mathbf{r}}) \boldsymbol{\sigma} \mathbf{a}^{(p_2)}_{L_2 M_2}(\mathbf{r}) g^{11}_{\kappa_\nu}(r, r'; E_i + \omega_1) \chi^{m_\nu}_{\kappa_\nu}(\Omega_{\mathbf{r}}) \\ &\times \chi^{m_\nu}_{\kappa_\nu}(\Omega_{\mathbf{r}'}) \boldsymbol{\sigma} \mathbf{a}^{(p_1)}_{L_1 M_1}(\mathbf{r}') f_i(r') \chi^{\mu_i}_{\kappa_i}(\Omega_{\mathbf{r}'}) dr' d\Omega_{\mathbf{r}'} dr d\Omega_{\mathbf{r}}. \end{aligned} \tag{4.25}$$

A careful comparison of Eq. (4.25) with similar expressions for the other IJ components reveals that the angular dependent parts of all M^{IJ}_{12} elements have a similar structure. At the beginning of this chapter I showed that in the evaluation of the transition amplitude the angular parts depend only on the total angular momentum and its projections. As the angular parts of the large and the small part of the wave function (as well as the four 2x2-component expressions of the Greens functions) with κ and $-\kappa$ have the same total angular momentum (c.p. Eq. (2.12)), the angular dependent parts in Eq. (4.25) are the same for all four different two-component spinor contributions M^{IJ}_{12}. So all the reduced

matrix element two-component spinor contributions can be combined into a single reduced matrix element for a specific multipole L_1, p_1, L_2, p_2:

$$S_{j_\nu}^{L_1 p_1 L_2 p_2}(-\omega_2) = S_{j_\nu}^{L_1 p_1 L_2 p_2;11} + S_{j_\nu}^{L_1 p_1 L_2 p_2;12} + S_{j_\nu}^{L_1 p_1 L_2 p_2;21} + S_{j_\nu}^{L_1 p_1 L_2 p_2;22}. \tag{4.26}$$

These parts of the reduced matrix element can be explicitly evaluated using the position representation of the spinors (2.7), the radial Greens function (4.20), and an explicit form of the multipole components $\mathbf{a}_{LM}^{(p)}$ from Eq. (3.13). With some analytical effort [12] it can be shown that these parts are given by:

$$\begin{aligned} S_{j_\nu}^{L_1 p_1 L_2 p_2;IJ}(-\omega_2) =& 2p \sum_{l_\nu} \sum_{\Lambda_1 \Lambda_2} A^{IJ} \cdot (2p)^{2(\gamma-1)} \left\langle (-1)^I \kappa_f \left|\left| \boldsymbol{\sigma} \mathbf{Y}_{L_1,\Lambda_1} \right|\right| (-1)^{I+1} \kappa(j_\nu l_\nu) \right\rangle \\ & \times \left\langle (-1)^{J+1} \kappa(j_\nu l_\nu) \left|\left| \boldsymbol{\sigma} \mathbf{Y}_{L_2,\Lambda_2} \right|\right| (-1)^J \kappa_i \right\rangle \\ & \times \sum_{n=0}^{\infty} \sum_q C_{nq}^{IJ} I_{\Lambda_1}^{'I',n}(k_1, p(E_i - \omega_2), \alpha_q)\; I_{\Lambda_2}^{'J',n}(k_2, p(E_i - \omega_2), \alpha_q'), \end{aligned} \tag{4.27}$$

where I used the constants C_{nq}^{IJ}, α_q, and $p(E)$ from the solution of the Dirac Coulomb Greens function (4.23) and κ_i, κ_f as the κ quantum number of the initial and final state. I write $\kappa(j_\nu, l_\nu)$ for the intermediate κ quantum number to emphasize its dependence on the total and orbital angular momenta j_ν, l_ν. I also introduced symbols for reduced matrix elements that depend only on the angular parts of the spinors, Greens function and multipole components. These components were evaluated e.g. by Grant [54, 63] and are given by:

$$\begin{aligned} \left\langle \kappa_a \left|\left| \boldsymbol{\sigma} \mathbf{Y}_{L,\Lambda} \right|\right| \kappa_b \right\rangle =& \left[j_a, j_b, L, \Lambda, l_b\right]^{-1/2} \begin{Bmatrix} l_a & 1/2 & j_a \\ l_b & 1/2 & j_b \\ L & 1 & \Lambda \end{Bmatrix} \\ & \times \sqrt{\frac{3}{2\pi}} \left\langle l_b 0, \Lambda 0 \,|\, l_a 0 \right\rangle, \end{aligned} \tag{4.28}$$

where the 3x3 matrix in curly brackets is the so-called Wigner 9j-Symbol [35].

Finally, in Eq. (4.27) the radial integration can be decomposed into products of two similar integrals here abbreviated by $I_{\Lambda_1}^{'I,n}(k_1, p(E), \alpha_q)$. These integrals can be solved numerically [4] or analytically. For example, in my diploma thesis [12] I found a representation in terms of generalized Laguerre functions $P_b^a(x)$:

$$\begin{aligned} I_{\Lambda_1}^{'I,n}(k_1, p(E), \alpha_q) =& \sum_{k=0}^{n-|\kappa|} \sum_{\chi=0}^{n} N_j c_{j;k}^{\pm} (\beta_n^\kappa)^{k+\gamma_j-1} (2p(E))^\chi \binom{n+\alpha_q}{n-\chi} \\ & \times \frac{(-1)^\chi}{\chi!} \sqrt{\frac{\pi}{2k_1}} \left((\beta_n^\kappa + p(E))^2 + k_1^2 \right)^{-\frac{1}{2}\mu} \\ & \times \Gamma(\Lambda_1 + 1/2 + \mu) P_{\mu-1}^{-\Lambda_1+1/2} \left(\frac{\beta_n^\kappa + p(E)}{\sqrt{(\beta_n^\kappa + p(E))^2 + k_1^2}} \right), \end{aligned} \tag{4.29}$$

here I used the substitution $\mu = \chi + \gamma + k + \gamma_\kappa + 1/2$. The expressions γ, $p(E)$, ν, and α_q are from the definition of the Greens function (4.23) and the γ_κ, β_n^κ and $c_{j;k}^{\pm}$ are from the definition of the wave functions (2.18). The sign of $c_{j;k}^{\pm}$ is $+$ for $I = 2$ and $-$ for $I = 1$.

For a conclusive evaluation of the reduced matrix element the parts (4.27) are integrated into the whole element (4.26).

With such an explicit solution for the reduced matrix elements it is possible to get some insights into the symmetry properties of the reduced matrix elements. Of special interest is the question how the reduced matrix elements for two-photon absorption relate to the reduce matrix elements for two-photon emission. To study this question I take a closer look at the multipole component $\mathbf{a}^{(p)}_{LM}$, c.p. Eq. (3.13). From this definition we see that the difference of the multipole components $\mathbf{a}^{(p)}_{LM}$ for absorption and the multipole components $\mathbf{a}^{(\mathbf{p})\dagger}_{\mathbf{LM}}$ for emission of a photon only lies in their angular parts. The angular part of the emission component is the complex conjugate of the angular part of the absorption component. In the reduced matrix elements these angular parts contribute by means of the expressions (4.28). A close inspection of these expressions by means of angular momentum algebra reveals the following symmetry:

$$\left\langle \kappa_a \left|\left| \left(\boldsymbol{\sigma}\mathbf{Y}_{L,\Lambda}\right)^* \right|\right| \kappa_b \right\rangle = (-1)^L \left\langle \kappa_a \left|\left| \boldsymbol{\sigma}\mathbf{Y}_{L,\Lambda} \right|\right| \kappa_b \right\rangle . \tag{4.30}$$

As I mentioned in the first part of this chapter, we thus have the following symmetry between the reduced matrix elements for two-photon emission and absorption:

$$\begin{aligned} &\sum_\nu \frac{\left\langle n_f l_f j_f \left|\left| \boldsymbol{\alpha}\mathbf{a}^{(p_1)\dagger}_{L_1M_1} \right|\right| n_\nu l_\nu j_\nu \right\rangle \left\langle n_\nu l_\nu j_\nu \left|\left| \boldsymbol{\alpha}\mathbf{a}^{(p_2)\dagger}_{L_2M_2} \right|\right| n_i l_i j_i \right\rangle}{E_i - \omega_2 - E_\nu} \\ = (-1)^{L_1+L_2} &\sum_\nu \frac{\left\langle n_f l_f j_f \left|\left| \boldsymbol{\alpha}\mathbf{a}^{(p_1)}_{L_1M_1} \right|\right| n_\nu l_\nu j_\nu \right\rangle \left\langle n_\nu l_\nu j_\nu \left|\left| \boldsymbol{\alpha}\mathbf{a}^{(p_2)}_{L_2M_2} \right|\right| n_i l_i j_i \right\rangle}{E_i - \omega_2 - E_\nu}. \end{aligned} \tag{4.31}$$

4.2.2 Advanced solutions of the reduced matrix element

While the solutions based on the Sturmian representation of the Dirac Coulomb Greens function are a relatively simple analytical solution, this model has a number of drawbacks. Most importantly, if the intermediate energy e.g. $E_i + \omega_2$ is larger than the ionization threshold of the ion, the sums in the Sturmian representation (4.20) no longer converge and different methods have to be employed. Such energies appear e.g. often in photon scattering processes. In order to describe the elastic scattering of higher energy photons in chapter 6 we therefore used reduced matrix elements obtained by Vladimir Yerokhin, c.p. [53]. He employed a different representation of the Greens function based on so-called Whittaker functions. With such a form of the Greens function the solutions can be continued to intermediate energies that are above the ionization limit. However, this continuation has a branch cut at the real axis. By carefully including small imaginary shifts to the energies of the photons, Yerokhin's method chooses the "right" branch of the function. With such a well-defined Greens function the reduced matrix elements are subsequently evaluated by a numerical integration of the radial integrals.

In both of these Greens function approaches the participating ions are described as electrons in a field of an infinite heavy point-like nucleus. Effects that arise e.g. from a finite shape of the nucleus would have to be included perturbatively into such a system. Furthermore, for

photon energies that come close to so-called resonances, i.e. where the two-photon process could be described as a two-step process via a real intermediate state $|i\rangle \to |\nu\rangle \to |f\rangle$, the precise energies of these states (including e.g. the Lamb shift) and their line width , c.p. [47], become very important. While these issues are beyond the scope of this thesis, it should be mentioned that such effects can be described e.g. by using numerical finite basis set methods, c.p. e.g. [6]. In such models the ion is placed in a finite box, in which both for the bound states and the positive and negative "continuum" the number of states is finite. By reducing the infinite number of states to a finite number the infinite sum in the definition of the reduced matrix element (4.4) becomes finite and can be performed explicitly. In a practical calculation of this kind the states are e.g. expressed in terms of B-splines or B-polynomials.

4.2.3 Reduced matrix elements for He-like systems with IPM

Under the assumption of the independent particle model, i.e. when we can neglect the electron-electron interaction, the reduced matrix elements for two-photon absorption by He-like ions can be straightforwardly expressed in terms of H-like reduced matrix elements. We determine the element by comparing Eq. (4.3) with a similar calculation in which the He-like states are expressed in terms of H-like states by means of the independent particle model (2.24). With some lengthy but trivial angular momentum algebra it can be shown that the He-like elements are:

$$S_{J_\nu}^{He;L_1 p_1 L_2 p_2}(-\omega_2) = \sum_{j_\nu} [J_i, J_f, J_\nu, J_\nu]^{1/2} (-1)^{j_i + j_\nu + L_1 + L_2 - J_\nu - J_f + 1} \times \begin{Bmatrix} j_i & j_1 & J_i \\ J_\nu & L_1 & j_\nu \end{Bmatrix} \begin{Bmatrix} j_\nu & j_1 & J_\nu \\ J_f & L_2 & j_f \end{Bmatrix} S_{j_\nu}^{H;L_1 p_1 L_2 p_2}(-\omega_2), \qquad (4.32)$$

here j_1 is the total angular momentum of the non-interacting spectator electron, j_i, j_ν, j_f are the initial intermediate and final total angular momenta of the H-like state of the "active" electron and the J_i, J_ν, J_f are the total angular momenta of the He-like states.

We see from Eq. 4.32 that the reduced matrix elements for two-photon absorption and emission in He-like ions inherit the symmetry of the H-like reduced matrix elements (4.31). The He-like elements can therefore be used in Eq. (4.3) to evaluate the two-photon decay amplitude. Similar arguments can be given for the relevant symmetries we used in the derivation of the scattering amplitude.

Following the introduction of the theoretical approach I used in my research, I will present the results that originated from these efforts in the next two chapters.

5 Two-photon decay in strong laser fields

Based on the theoretical approach that was developed in chapter 3 and 4, in the following two chapters a number of two-photon processes are examined in detail. These studies demonstrate on the one hand how the relativistic method can be applied to describe such systems. On the other hand they allow to examine how much such two-photon processes can be externally influenced and what kind of interesting effects can be measured in such systems. These questions are motivated by the following considerations.
In two-photon processes a number of interesting quantities can be observed, e.g. in two-photon decay total as well as energy- and angular-differential decay rates can be measured. For some specific decay parameters, e.g. a certain energy sharing of the photons, these quantities are very sensitive to small changes of the physical system. Such configurations can be used to study relativistic and higher multipole effects in detail and might even allow to measure tiny effects caused by QED or even the parity non-conserving (PNC) weak interaction between the nucleus and the electrons. This kind of measurements would require a very precise control of the two-photon process.
One way to control such processes is the use of strong external electric fields usually facilitated by means of lasers. Prominently, there have been some proposals to use two-photon absorption of polarized light to measure PNC effects in heavy few-electron Uranium ions [3, 11]. However it was an open question how the electromagnetic field from strong lasers that would be necessary for such experimental schemes would affect the properties of the two-photon absorption, most importantly if side effects would make such experiments impossible.

To examine these questions I studied here the effects of external electric field on two-photon decay, c.p. Fig. 5.1. In the first part of this chapter I present my study [60] on two-photon decay of H- and He-like ions in a static electric field. Such systems do not only allow to examine the feasibility of PNC measurement schemes [3], but can also serve as a toy model to analyze general effect of perturbations on two-photon processes. This study is based on research I did for my diploma thesis [12], in which I performed a preliminary analysis of the effect of external electric fields on two-photon decay in H-like ions. In additional work as part of my PhD-studies the results of these calculations were analyzed in greater detail, for example the effect of possible single-photon decay was included. Furthermore, new calculations for electric perturbations on the two-photon decay of He-like ions were performed.

Additional to this study I present some of my previously unpublished results on one of the effects of dynamic electromagnetic fields on two-photon decay in the second part of this chapter. Namely in such fields one of the emitted photons of the two-photon transition can be emitted via induced transitions. I examine the properties of this so-called singly

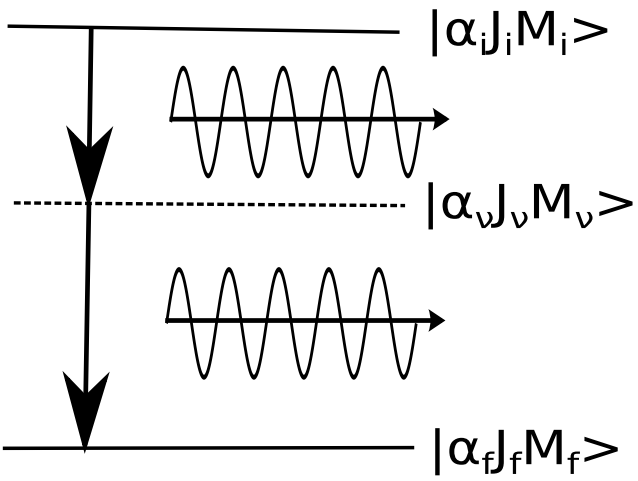

Fig. 5.1: Schematic description of two-photon decay. An initial state $|\alpha_i J_i M_i\rangle$ decays to a final state $|\alpha_f J_f M_f\rangle$ by simultaneous emission of two photons via an virtual intermediate state $|\alpha_\nu J_\nu M_\nu\rangle$. Here I use the notation from chapter 4 for the total angular momentum and its projection J, M and the abbreviation α for the other quantum numbers n, l for H-like ions and N, P for He-like ions.

stimulated or enhanced two-photon decay in highly charged ions and explore the feasibility of its measurement.

5.1 Perturbation of two-photon decay of H- and He-like ions by static electric fields

5.1.1 Introduction

In most of the proposals to employ laser-driven two-photon absorption to measure PNC effects [3] the lasers have a frequency in the optical or infrared regime. The period of such fields is very long in comparison to typical time scales for two-photon transitions in heavy ions. To study the effect of such external perturbations on the ion, we can therefore, as a first approximation, assume their electric fields to be static. Furthermore, I consider relative weak electric fields that are weaker than the critical field (3.54) defined in chapter 3.

In such fields I analyze the decay properties for spontaneous $2s_{1/2} \to 1s_{1/2}$ and $2p_{1/2} \to 1s_{1/2}$ two-photon decay in H-like ions, based on the results from [12], and for $2^1S_0 \to 1^1S_0$ and $2^3P_0 \to 1^1S_0$ decay in He-like ions. Specifically, I discuss the behavior of the total decay rate, the energy distribution of the emitted photons, and the photon-photon angular correlation for photons with a specific energy sharing.

5.1.2 Linear perturbed two-photon decay

In chapter 4 we presented solutions for the two-photon decay amplitude for H-like and heavy He-like ions. These amplitudes allow us to evaluate the two-photon decay rates, the energy distributions of the photons and their angular correlations by means of Fermi's golden rule (3.45).

To study two-photon transitions in external electric fields, a similar decay amplitude for two-photon decay in an external field needs to be derived. The evaluation of such a dressed decay amplitude proceeds in the same way for H-like and He-like systems and is performed only once with the same quantum numbers we used for the evaluation of the two-photon decay amplitudes in H-like and He-like systems in chapter 4.

In general, deriving a solution for the dressed two-photon decay amplitude would require to consider the effect of the electric field on the initial, virtual intermediate and final state of the transition amplitude Eq. (4.1). However, we can greatly simplify these calculations if we follow the discussion in chapter 3. In this chapter it was mentioned that the effect of a "weak" electric field with the field strength F on the states of the ion can be described using non-degenerate time-independent perturbation theory. The perturbed state of the ion includes, on top of the original unperturbed state, mixing contributions from other eigenstates of the ion. We showed in the final part of chapter 3 that in a first approximation it is sufficient to include mixing between states with similar energies, specifically an unperturbed state and its so-called next neighbor state, c.p. Eq. (3.52).
If we consider the decay of the $2s_{1/2}, 2p_{1/2}$ states in H-like ions or the $2^1S_0, 2^3P_0$ states in He-like ions to the ground states, we can further simplify the dressed two-photon transition amplitude. On the one hand, in comparison to the excited initial state, the energy difference between the ground state and any state it could mix with is huge. For the two-photon decay amplitude the contribution from the perturbation of the ground state is therefore insignificant in comparison to the contribution from the initial state and can be neglected. On the other hand, similarly, in the case when energy sharing between the two emitted photons is not too one sided, the energy of the virtual intermediate state, i.e. $E = E_i - \omega_1$, has a huge distance to the energy of any real state of the ion with which it could mix. We can therefore also neglect potential perturbative contributions from the intermediate state. Due to these new results complicated calculation on the perturbative contributions from the ground and intermediate state I assumed to be non-negligible in my earlier work [12] can be avoided. The simple first order result I derived in this work therefore turns out to be a reasonable approximation to describe the two-photon decay amplitude in an electric field. This dressed decay amplitude M'_{fi} consists of the decay amplitude of the unperturbed initial state M_{fi}, evaluated with Eq. (4.3), and a so-called induced decay amplitude $M^{ind}_{fi'}$, which is defined as the two-photon decay amplitude (4.3) for the transition of the "next neighbor" state to the ground state:

$$M'_{fi} = M_{fi} + F\eta \cdot M^{ind}_{fi'} \delta_{M_i, M_{i;ind}} \delta_{l_i, l_{i;ind} \pm 1} \delta_{S_i, S_{i;ind}}, \tag{5.1}$$

with the Stark mixing parameter η which is the projection of the vectorial parameter η from Eq. (3.53) on the quantization axis. I included the conditions on the orbital $(l_i, l_{i;ind})$ angular momenta of the acting electrons of the initial and intermixed next neighbor state

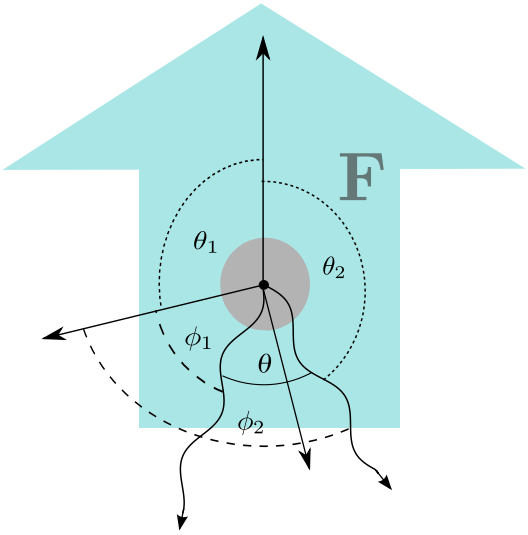

Fig. 5.2: Adopted geometry of two-photon decay in an electric field, with field strength F, directed parallel to the quantization axis.

and the projection of the total angular momenta of these states ($M_i, M_{i;ind}$) and their total spin $S_i, S_{i;ind}$ for Stark mixing between two states from chapter 3 by means of δ symbols. A similar solution was found in my naive approach in [12].

The $M_i = M_{i;ind}$ mixing condition was determined in chapter 3 using a coordinate system in which the electric field is parallel to the quantization axis. I therefore discuss the two-photon decay in electric fields in a spherical coordinate system in which the quantization axis is parallel to the electric field **F** as seen in Fig. 5.2. In such a coordinate system the direction of the electric field can not be easily changed. To study how the direction of the electric field affects the emission of the two-photons I therefore "rotate" the two-photon decay process and observe it for a number of different emission geometries. In these geometries the angle between the emission directions of the photons θ, c.p. Fig. 5.2, is the same, but there are different angles between these directions and the external field. For a good overview of the dependence of the decay properties on the direction this field it is sufficient to define three distinct emission geometries. We have first the "parallel" emission geometry where one of the photons is emitted parallel ($\phi_1 = \phi_2 = 0°, \theta_1 = 0°, \theta_2 = \theta$, c.p. Fig. 5.2) to the quantization axis, second the "antiparallel" emission geometry ($\phi_1 = \phi_2 = 0°, \theta_1 = 180°, \theta_2 = 180° - \theta$) where it is emitted antiparallel and finally the perpendicular emission geometry ($\phi_1 = 0°, \phi_2 = \theta, \theta_1 = 90°, \theta_2 = 90°$) where both photons are emitted perpendicular to the electric field (θ is here the opening angle between the photons).

With this definition of the coordinates system I can now describe the decay properties. As a first step I insert the dressed transition amplitudes (5.1) into Fermi's golden rule (3.45) and include the (differential) state density $d\rho_{2Ph}(\omega_1, \omega_2)$ for two spontaneously emitted photons (3.46). I consider initially unpolarized ions and don't observe the state of the ion after the scattering process. Likewise in this study the polarization of the emitted photons plays no role and it can be summed over these polarizations. Such a system is modeled by averaging over the magnetic quantum number of the initial state M_i and summing over the magnetic quantum number of the final state M_f and the possible projections λ_1, λ_2 of the circular

polarization of both photons. We get a triple differential decay rate, differential in the energy of one of the photons ω_1 and in the propagation directions Ω_1, Ω_2 of both photons:

$$\begin{aligned}\frac{dW}{d\omega_1 d\Omega_1 d\Omega_2} =& \frac{\alpha_S^2 \omega_1 \omega_2}{2\pi(2J_i+1)} \sum_{M_i,M_f} \sum_{\lambda_1,\lambda_2} [M_{fi} M_{fi}^\dagger + \eta\eta^* F^2 M_{fi'}^{ind} M_{fi'}^{ind\,\dagger} \\ &+ \eta F M_{fi'}^{ind} M_{fi}^\dagger + \eta^* F M_{fi} M_{fi'}^{ind\,\dagger}]. \end{aligned} \tag{5.2}$$

Here J_i is the total angular momentum of the initial state and the large but finite volume that was introduced in the definition of the electron-photon interaction operator is canceled by the volumes from the state density $d\rho_{2Ph}(\omega_1, \omega_2)$. This angle-differential rate will be used to discuss angular correlations of the emitted photons. Its behavior is determined by three different parts: First there is the original unperturbed part that is represented by the first expression in the square brackets of Eq. (5.2). Its size does not depend on the strength or direction of the electric field. Then there is the contribution from the newly induced decay channel that can be seen in the second term of the definition. It has a quadratic dependence on the field strength F. Finally there are interference terms between the original and the induced decay channel that can be seen in the two remaining parts of the equation. These contributions depend linearly on F.

The triple-differential rate (5.2) can be used to evaluate other interesting properties such as the continuous energy distribution of the emitted photons. This distribution can be described by means of the energy differential decay rate, i.e. by integrating Eq. (5.2) over the directions Ω_1, Ω_2 of the emitted photons.
It is worthwhile to discuss this integration in more detail. To evaluate the energy distribution of the photons we have to integrate over products of the angular dependent parts of a decay amplitude (4.3) with the complex conjugated angular parts of another possible different decay amplitude. On a basic level this integration can be decomposed into sums over products of two expressions of the type:

$$K_{ang} = \int (-i)^{L-L'} (-i\lambda)^{p-p'} D^{L\,*}_{M\lambda}(\Omega) D^{L}_{M'\lambda}(\Omega) d\Omega, \tag{5.3}$$

with L, L' the multipole order of the contribution M, M' the the transmitted angular momentum projection, and p, p' the parameters that distinguish "magnetic" from "electric" transitions. For symmetry reasons in the decay rate always both summands with K_{ang} and K^*_{ang} will appear.
It is well known, c.p. [35], that for different L, L' the integral over the rotation matrices vanishes. Likewise if $L = L'$ but $p \neq p'$, K_{ang} and its complex conjugate K^*_{ang} cancel each other. Thus the angular integral of different multipole contributions vanishes. The induced and original initial state have a different parity and their two-photon decay processes must proceed by means of different multipole combination, e.g. E1E1 and E1M1. Thus the interference terms between the decay of the original and the induced initial state vanish, c.p. [12]. The energy distribution therefore only consists of an unperturbed and an induced quadratic part.

For future discussions it is at this point useful to introduce a natural scale for the energy of the photons. Such as scale is (for example) given by the amount of the total transition

energy x that is emitted by one of the photons, the continuous so-called energy sharing of the photons:

$$x = \frac{\omega_1}{E_i - E_f}. \tag{5.4}$$

By means of this energy sharing the energy-differential decay rate is:

$$\frac{dW}{dx} = \frac{\alpha_S^2 \omega_1 \omega_2 (E_i - E_f)}{2\pi(2J_i+1)} \sum_{M_i,M_f} \sum_{\lambda_1,\lambda_2} \left[M_{fi} M_{fi}^{\dagger} + \eta\eta^* F^2 M_{fi'}^{ind} M_{fi'}^{ind\,\dagger} \right]. \tag{5.5}$$

Additional to these differential rates I also consider total two-photon decay rates. These rates are essential to estimate the feasibility of experimental schemes employing external fields [3]. They can be evaluated by further integrating Eq. (5.5) over all possible energy sharings x:

$$W_{2ph} = 1/2 \int_0^1 dx \frac{dW}{dx}. \tag{5.6}$$

In these calculations I included the exchange symmetry of the photons by means of the prefactor $1/2$.

The dressed total two-photon decay rate has a similar structure as the energy distribution. As in this total decay rate similarly to Eq. (5.5) only the absolute value of the mixing parameter η plays a role, it is very convenient for the interpretation to replace this parameter with the critical field strength $F_{max} = 1/|\eta|$ I defined in Eq. (3.54). This critical field strength provides a natural scale for the field strength that can be used in the interpretation of the results.

$$W'_{2ph} = W_{2ph} + \frac{F^2}{F_{max}^2} W_{2ph}^{ind}. \tag{5.7}$$

The dressed two-photon rate consists of the original undisturbed two-photon rate W_{2ph} enhanced by an induced two-photon rate W_{2ph}^{ind} (weighted by the strength of the external electric field).

It is evident from Eq. (5.7) that this total rate has two major limitations (not considered in [12]): On the one hand, I assumed in chapter 3 that the mixing parameter is small $(F/F_{max}) \ll 1$ and we do not need to take any steps to assure the normalization of the perturbed initial state. Especially if $F/F_{max} \to 1$, i.e. if our perturbative approach breaks down, we would need to include a normalization constant $N = \frac{1}{1+(F/F_{max})^2}$. Thus for near critical field strengths the total value of dressed two-photon decay rates will depart from its true value. As we are not very interested in precise values of these rates this normalization problem will not be further discussed.

On the other hand, if we want to have a meaningful discussion of the lifetimes of H- and He-like states in an external electric field, we can not limit ourselves to two-photon decay. For most states decay rates from single photon decay of excited states W_{1ph} are at least comparable if not much larger than the two-photon rates. In fact, two-photon decay can usually only be observed for so-called metastable states, i.e. if the leading order single photon decay is not possible due to exchange rules. We can easily extend our model (5.7) to

include the single photon decay of the original (W_{1ph}) and induced (W_{1ph}^{ind}) next neighbor state:

$$W' = (W_{1ph} + W_{2ph}) + \left(\frac{F}{F_{max}}\right)^2 (W_{1ph}^{ind} + W_{2ph}^{ind}). \tag{5.8}$$

With such a model the role of different decay channels of excited ions in an electric field can be estimated much more realistically.

Electric field strengths and laser intensities

I was originally motivated to study two-photon decay under the influence of an external electric field by the desire to determine the feasibility of experimental schemata employing strong lasers. To be able to test such a feasibility it is useful in the discussion to know how the peak electric field strength and the intensity of a laser are related. As I will discuss both field strength as well as intensities in units that are easily understandable, in this paragraph SI units will be used.

The intensity I of a laser can be evaluated from the energy density w of the electromagnetic field:

$$I = wc, \tag{5.9}$$

with c the speed of light.

For a plane wave such an energy density has been shown to be (c.p. Chapter 7 in [64]):

$$w = \frac{\epsilon_0 F^2}{2}, \tag{5.10}$$

with ϵ_0 the electric field constant.
By combining the last two equations the following relation between the peak field strength and the intensity of the laser can be found:

$$I = \sqrt{\frac{\epsilon_0}{\mu_0}}\frac{F^2}{2}, \tag{5.11}$$

with μ_0 the magnetic field constant.

This equation can be used to define a critical intensity I_{max} corresponding to a peak critical field strength F_{max}:

$$I_{max} = \sqrt{\frac{\epsilon_0}{\mu_0}}\frac{F_{max}^2}{2}. \tag{5.12}$$

5.1.3 Results and discussion

I begin the analysis on two-photon decay in external electric fields by clarifying the initial conditions of the system. In this analysis I concentrate on two-photon decay of excited states to the ground state. As a first step the initial conditions of the unperturbed systems need to be specified. To avoid dealing with complications like cascades of transitions, I select suitable initial states in which the excited electron has a principal quantum number of $n = 2$.

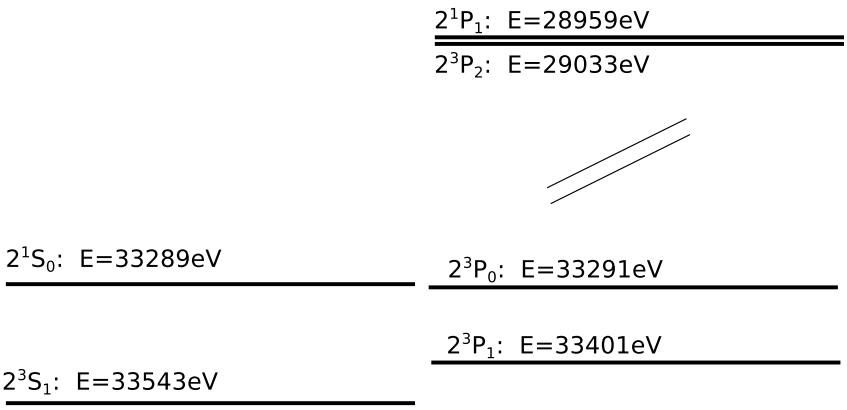

Fig. 5.3: Energies of the N=2 levels in U^{90+} according to [33].

Specifically, I consider for H-like ions as a toy model the $2s_{1/2} \to 1s_{1/2}$ and $2p_{1/2} \to 1s_{1/2}$ two-photon transition, like in [12]. In He-like ions I choose the experimentally relevant decay of the metastable 2^1S_0 and 2^3P_0 states, c.p. [3].

The effect of the external electric field is included by Stark mixing of the initial states with its so-called next neighbor state. This next neighbor state is the state with the smallest energy difference to the initial state that fulfills the conditions in Eq. (5.1). For H-like ions these states are easily found to be the $2p_{1/2}$ state for an initial $2s_{1/2}$ state and vice versa. On the other hand, for He-like ions the situation is not directly evident. To select suitable next neighbor states I show in Fig. 5.3 precise results for the energy levels of all $N = 2$ states in U^{90+} by Artemyev [33]. From the figure and the conditions in Eq. (5.1) we see that the main mixing contribution for an initial 2^1S_0 state arises from the 2^3P_1 state and similarly for an initial 2^3P_0 state arises from the 2^3S_1 state. In a similar way I can show that the same states also dominate the contributions in lighter ions.

With these clarifications it is now possible to determine the critical field strength that is needed to evaluate the decay rates in the electric field. I used Eq. (3.54) with level differences from [30, 33, 38] and lifetimes both directly from [59, 65] for the decay of excited He-like ions and evaluated with the Dirac package [66] for H-like ions, to determine the critical field strength F_{max}. For the upcoming discussion I also include the critical intensity via Eq. (5.12). In table 5.1 I compiled these critical field strengths and intensities for the mixing of all considered initial states with the next relevant neighbor state for neutral hydrogen and U^{91+}, as examples for H-like ions and in Xe^{52+} and U^{90+} as examples for heavy He-like ions. Previous to my research most of these critical field strengths were not published. A comparison was only possible for neutral hydrogen where I found a good agreement with the value of $F_{max} = 475V/cm$ from the non-relativistic calculations [67].

In table 5.1 we see that in general for heavier ions the critical field strength and the intensity become larger. Their detailed Z-dependence is complicated, especially for He-like ions, and depends both on the lifetime of the states but also on all effects that influence the energy difference between the initial state with its next neighbor such as the Lamb shift or, in the case of He-like ions, electron-electron interactions.

Ion/atom	F_{max}	I_{max}
Stark mixing of $2s_{1/2}$ and $2p_{1/2}$ states (H-like ions)		
Hydrogen	$478 V/cm$	$303 W/cm^2$
U^{91+}	$9.72 \cdot 10^{11} V/cm$	$1.25 \cdot 10^{21} W/cm^2$
Stark mixing of 2^1S_0 and 2^3P_1 states (He-like ions)		
Xe^{52+}	$3.35 \cdot 10^{10} V/cm$	$1.49 \cdot 10^{18} W/cm^2$
U^{90+}	$8.71 \cdot 10^{11} V/cm$	$1.01 \cdot 10^{21} W/cm^2$
Stark mixing of 2^3P_0 and 2^3S_1 states (He-like ions)		
Xe^{52+}	$5.17 \cdot 10^{11} V/cm$	$3.55 \cdot 10^{20} W/cm^2$
U^{90+}	$3.15 \cdot 10^{12} V/cm$	$1.32 \cdot 10^{22} W/cm^2$

Tab. 5.1: Critical field strengths and intensities for Stark mixing of the $2s_{1/2}$ and $2p_{1/2}$ states in different H-like ions and the 2^1S_0 and 2^3P_1 as well as the 2^3P_0 and the 2^3S_1 states in different He-like ions.

An examination of the numerical values of the critical intensities shows that even for H-like or He-like uranium such intensities are well within reach of modern high power laser facilities. They are in fact of the same order of magnitude of the fields that would be required in the proposed two-photon absorption schemata, c.p. [3]. It is therefore essential to study the effect of such fields on the decay properties of the excited state to decide on the feasibility of such ideas.

Total decay rates of perturbed H- and He-like states

As a first step to examine the decay properties of two-photon decay in an external electric field the total two-photon decay rates are discussed. To determine the rates I first numerically approximate the reduced two-photon absorption matrix elements (4.26) and (4.32) with the Mathematica computer algebra system. Here I introduced for the calculation of two-photon decay in He-like ions effective charges to include some effects of the electron-electron interaction as I mentioned in chapter 2. For Xe^{52+} an effective charge of $Z_{eff} = 53.333$ and for U^{90+} a charge of $Z_{eff} = 91.208$ was used. The reduced elements are used in Eq. (4.1) to determine the all-multipole two-photon decay amplitudes. We found out that for practical purposes it is sufficient to consider only the multipole contributions up $L = 3$. For H-like ions I used the total decay rates from [12] that were evaluated in a similar way. By means of the definition of the differential decay rate (5.5) I used these amplitudes to determine the total decay rate (5.7).

In table 5.2 I present my results for the total two-photon decay rates of different excited states in the presence of an external electric field. From table 5.2 it can be seen that for field strengths, for which the theoretical approach of this work can be applied, i.e. for $F < F_{max}$, the two-photon decay rate is only noticeably affected by the electric field if the decay rate of the two-photon decay of the next neighbor state has at least a similar size as the decay rate of the unperturbed system. For example, in the currently used model, as it was shown

$W'_{2ph} = W_{2ph} + (F/F_{max})^2 \cdot W^{ind}_{2ph}$				
Transition	Hydrogen		U^{91+}	
	$W_{2ph}[s^{-1}]$	$W^{ind}_{2ph}[s^{-1}]$	$W_{2ph}[s^{-1}]$	$W^{ind}_{2ph}[s^{-1}]$
$2s_{1/2} \to 1s_{1/2}$	8.229	$1.629 \cdot 10^{-5}$	$3.836 \cdot 10^{12}$	$6.255 \cdot 10^{10}$
$2p_{1/2} \to 1s_{1/2}$	$1.629 \cdot 10^{-5}$	8.229	$6.255 \cdot 10^{10}$	$3.836 \cdot 10^{12}$
	Xe^{52+}		U^{90+}	
	$W_{2ph}[s^{-1}]$	$W^{ind}_{2ph}[s^{-1}]$	$W_{2ph}[s^{-1}]$	$W^{ind}_{2ph}[s^{-1}]$
$2^1S_0 \to 1^1S_0$	$3.45 \cdot 10^{11}$	$3.98 \cdot 10^{8}$	$7.23 \cdot 10^{12}$	$2.48 \cdot 10^{10}$
$2^3P_0 \to 1^1S_0$	$7.09 \cdot 10^{6}$	$3.50 \cdot 10^{8}$	$5.29 \cdot 10^{9}$	$4.50 \cdot 10^{10}$

Tab. 5.2: Two-photon decay rate of specific excited states of H-like and He-like ions in an electric field, c.p. Eq. (5.7). The transitions are sorted by their zero-field decay channels and the F_{max} can be found in table 5.1.

in [12], there is no noticeable effect of the electric field on the $2s_{1/2} \to 1s_{1/2}$ two-photon y rate.

The decay rate of the induced transition channel is larger and we see an effect if the original unperturbed initial state has a negative parity. If it has a positive parity, the induced rate is smaller and plays only a minor role. To understand this behavior we remember that in the preceeding section we found that the next neighbors that intermix with the initial states have opposite parities, e.g. P states have S states as next neighbors. Thus for initial states with an even parity there is an induced parity-odd next neighbor and vice versa. Due to the parity conservation in two-photon processes (c.p. Eq. (3.44)), two-photon transitions of parity-odd states into the ground state do not have a E1E1 multipole contribution, that is dominating e.g. $2s_{1/2} \to 1s_{1/2}$ two-photon decay. In leading order they are determined by the E1M1 and E1E2 multipole contributions and therefore, as mentioned in chapter 3, their rate is smaller by a factor $(Z\alpha_S)^2$ in comparison to the decay rates of states with even parity (and an initial total angular momentum of $J_i \leq 2$). We can therefore expect to see the largest effect of the electric field in the $2^3P_0 \to 1^1S_0$ two-photon transition in He-like ions (although in the $2^3S_1 \to 1^1S_0$ decay a spin flip is required thus the E1E1 contribution is suppressed) and in the $2p_{1/2} \to 1s_{1/2}$ decay in H-like ions. Furthermore, for high-Z ions some effects of the electric fields will also be visible for the $2^1S_0 \to 1^1S_0$ process.

Up till now we discussed the effect of external electric fields on two-photon decay rates under the assumption that only such two-photon transitions are possible. In real physical systems other transition processes such as single photon decay are very important and in fact often dominate the lifetimes of specific states. To get a feeling for the different processes in Fig. 5.4 I compiled single- and two-photon decay rates for the relevant initial states for different isoelectric ions from [59, 65, 68] for He-like ions and for H-like ions from [9] combined with single photon decay rates evaluated by means of the DIRAC Package in Mathematica [66]. For comparison my results are added (as crosses) in the figure.

We see from Fig. 5.4 that my two-photon rates are in general in very good agreement with the literature. In the transition rates for the $2^3P_0 \to 1^1S_0$ two-photon decay (dashed line right graph) there are differences between my and Savukovs [59] results. These differences

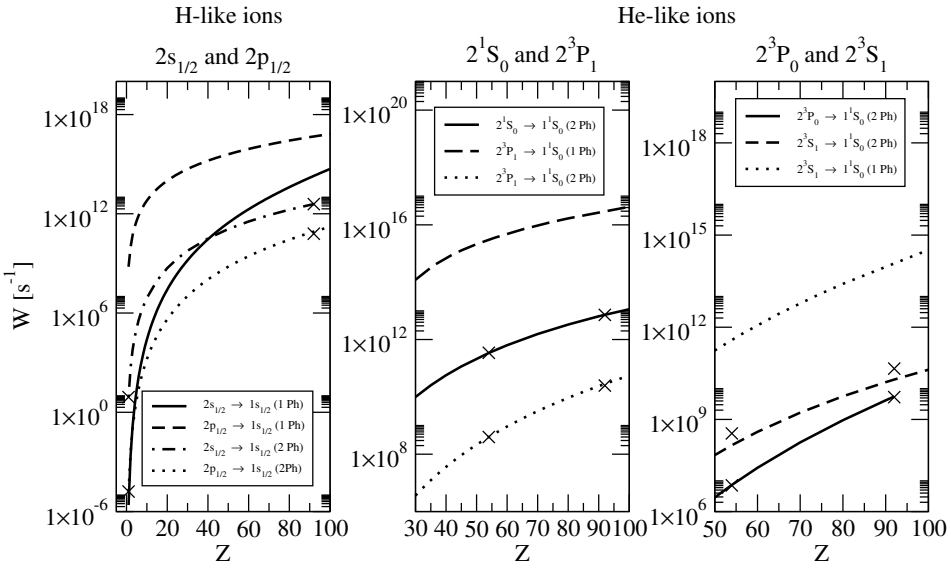

Fig. 5.4: Comparison of single- and two-photon decay rates for different initial states in H-and He-like ions. On the left panel single photon decay rates (DIRAC [66]) are compared to the two-photon $2s_{1/2} \to 1s_{1/2}$ decay rates by [9] and $2p_{1/2} \to 1s_{1/2}$ two-photon decay rates interpolated from the decay rate for hydrogen from [6] (Z^8-scaling comparable to rates in [59]). In the center panel I compare single photon decay of 2^3P_1 state from [65] with two-photon decay of the 2^1S_0 from Derevianko [68] and two-photon decay of the 2^3P_1 state based on our calculation for Z=54 (interpolated using Z^8 scaling). On the right panel finally I compare two-photon decay rates of the decay of 2^3P_0 state [59] (only E1M1) and 2^3S_1 [68] with single photon decay of 2^3S_1 from [65]. Additionally my values are added as black crosses for comparison.

arise from the fact that, in contrast to my calculations, he only included one (E1E2) of the two dominant (E1E2+E1M1) multipole contributions. Furthermore, it is evident that for most initial states the single photon processes have much higher rates and dominate the lifetime of the state. Realistic decay rates in an electric field must therefore consider both the one- and two-photon decay like in Eq. (5.8). In table 5.3 the constituent original and induced single and two-photon decay rates are collected. The single photon decay rates are taken from [65] for He-like states and calculated with the Dirac package [66] for H-like states. For simplicity other radiative or non-radiative transition processes, such as the hyperfine induced decay of the 2^3P_0 state, c.p. [59], are not included.

With Eq. (5.8) table 5.3 shows that if single photon decay plays a role, the decay rate and thus the lifetime of the perturbed state is predominantly determined by it. For field strengths $F \approx F_{max}$ this leads to a very short lifetime of states of the ion that are metastable in the absence of a field. Experimental approaches that irradiate excited metastable states with lasers near the critical intensity c.p. [3, 11] are therefore not feasible as such laser fields will lead to an immediate Stark induced depopulation of the initial state. Furthermore, for all practical purposes the consequences of Stark mixing on two-photon decay is not observable. Nevertheless, we can use this process as a toy model to further study the effect of external perturbation on two-photon processes.

Ion/atom	$W_{1ph}[s^{-1}]$	$W_{2ph}[s^{-1}]$	$W^{ind}_{1ph}[s^{-1}]$	$W^{ind}_{2ph}[s^{-1}]$
		$2s_{1/2} \to 1s_{1/2}$ transition		
Hydrogen	$2.50 \cdot 10^{-5}$	8.229	$6.27 \cdot 10^{8}$	$1.629 \cdot 10^{-5}$
U^{91+}	$1.95 \cdot 10^{14}$	$3.84 \cdot 10^{12}$	$4.73 \cdot 10^{16}$	$6.26 \cdot 10^{10}$
		$2p_{1/2} \to 1s_{1/2}$ transition		
Hydrogen	$6.27 \cdot 10^{8}$	$1.63 \cdot 10^{-5}$	$2.50 \cdot 10^{-5}$	8.229
U^{91+}	$4.73 \cdot 10^{16}$	$6.26 \cdot 10^{10}$	$1.95 \cdot 10^{14}$	$3.84 \cdot 10^{12}$
		$2^1S_0 \to 1^1S_0$ transition		
Xe^{52+}	–	$3.45 \cdot 10^{11}$	$2.88 \cdot 10^{15}$	$3.98 \cdot 10^{8}$
U^{90+}	–	$7.23 \cdot 10^{12}$	$2.94 \cdot 10^{16}$	$2.48 \cdot 10^{10}$
		$2^3P_0 \to 1^1S_0$ transition		
Xe^{52}	–	$7.09 \cdot 10^{6}$	$3.22 \cdot 10^{11}$	$3.50 \cdot 10^{8}$
U^{90+}	–	$5.29 \cdot 10^{9}$	$7.89 \cdot 10^{13}$	$4.50 \cdot 10^{10}$

Tab. 5.3: Constituent original and induced single and two-photon decay rates for the total decay rate (5.8) in an electric field. The two-photon rates for He-like ions (Xe^{52+} and U^{90+}) are taken from my calculation and for H-like ions (Hydrogen and U^{91+}) from [12]. Single photon decay rates are evaluated using the DIRAC package for decay in H-like ions and interpolated from Lins [65] values (with Z^4 dependence for the $2^3P_1 \to 1^1S_0$(E1) and Z^8 dependence for the $2^3S_1 \to 1^1S_0$(M1) decay) for transitions in He-like ions. The transitions are sorted by the original unperturbed decay process at $F = 0$.

Energy distributions

A commonly studied quantity of two-photon decay is the continuous spectral distribution of the emitted photons. In unperturbed systems it has been discussed in detail in the literature, e.g. [69]. I will here only analyze the effect of electric fields on these distributions. For two-photon decay in an electric field such an energy distribution is determined by Eq. (5.5) and can be evaluated by means of the same two-photon decay amplitudes we used in the preceding section.

According to Eq. (5.5) the perturbed distribution can be understood as a weighted overlap of the energy distributions from the original and the induced decay channel. Thus if the shapes of the original and induced energy differential decay rates differ, we can observe that in an electric field the appearance of the spectral distribution becomes field dependent. As an example I show in Fig. 5.5 the energy distribution of the $2p_{1/2} \to 1s_{1/2}$ two-photon decay in electric fields, based on the transition amplitudes from [12]. The general behavior of these energy distributions were discussed in [12]. In this text also a good agreement with different literature values [6, 9] was found.

As I showed in [12] for rising field strengths we observe a slow transition from the shape of the original transition to the shape of induced transition. This transition happens at field strengths for which the original and the induced two-photon rates are comparable, i.e. for $W_{2Ph} \approx (F/F_{max})^2 W^{ind}_{2Ph}$. The type of this deformation is entirely determined by the shape

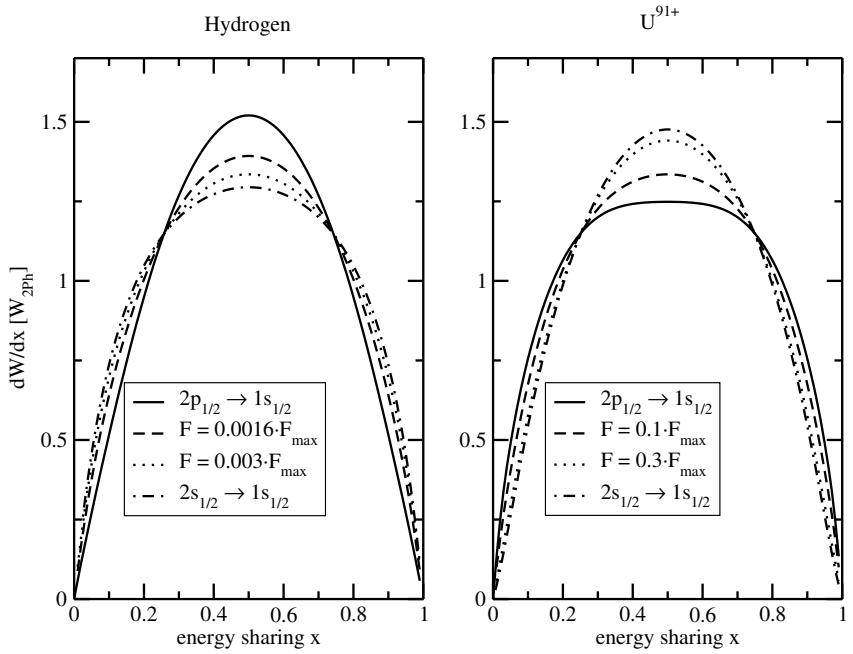

Fig. 5.5: Spectral distribution for $2p_{1/2} \to 1s_{1/2}$ two-photon decay of hydrogen and U^{91+} in an electric field. The field strengths Fs is given in terms of the critical field strength F_{max} (c.p. table 5.1). The energy distributions are normalized to the total decay rate. For comparison the energy distributions of the original and induced two-photon decay channels are shown.

of the original and induced spectral distribution. For example, we observe in Fig. 5.5 that in the decay of neutral hydrogen strong electric fields make the angular shape flatter. On the other hand, in the decay of U^{91+}, due to different Z-scaling of the higher multipole contributions in the original and induced two-photon transitions, for strong fields the shape becomes more pointy.

In He-like ions the difference between the spectral distribution of two-photon decay of the original and the induced next neighbor state can be more prominent and thus the effect of the electric field on the shape can be much more pronounced. As an example I show in Fig. 5.6 the energy distribution of a $2^3P_0 \to 1^1S_0$ two-photon decay in He-like uranium in the presence of an electric field . In this process the spectral distribution of the original transition (solid line) has its maximum for equal energy sharing. However, the distribution of the induced $2^3S_1 \to 1^1S_0$ two-photon decay has a maximum for uneven energy sharing, i.e. at $x \approx 0.05$ and $x = 0.95$. Strong electric fields have therefore a quite drastic effect on the shape of the energy distribution of the emitted photons.

Even though such changes of the spectral distribution are well visible, the required strong perturbations limit the usefulness of this effect. However, studying the energy distribution does allow to select regions of the energy sharing in which the other decay properties such as the angular correlation of the emitted photons are most strongly affected by the external influence.

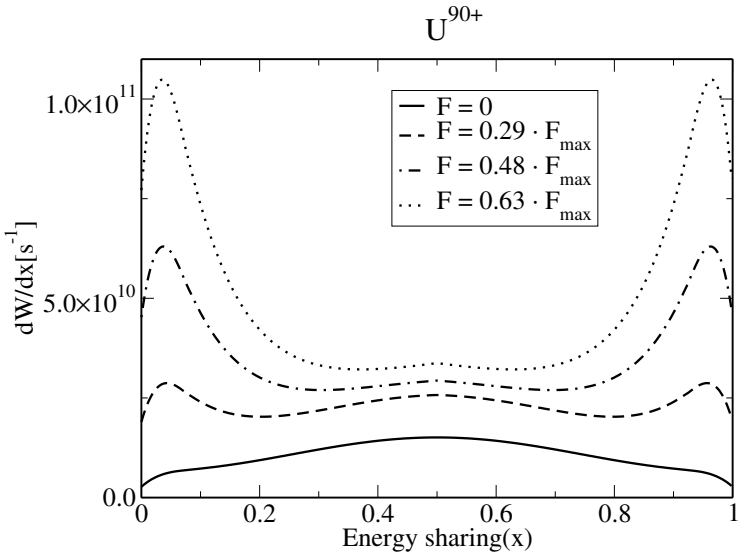

Fig. 5.6: Energy distribution of the emitted photons for a $2^3P_0 \to 1^1S_0$ two-photon decay of U^{90+} in an electric field for different electric field strengths F in units of the critical field strength F_{max}, cp. table 5.1.

Angular correlation and its dependence on the direction of the electric field

Apart from the total decay rate and the spectral distribution of the emitted photons it is nowadays possible to measure the two emitted photons in coincidence. Such measurements allow to study e.g. the dependence of the decay rate on the angle between emitted photons with a specific energy sharing x. Like in the case of the energy distribution of the emitted photons this so-called angular correlation has been studied in detail for unperturbed ions [4, 69] and I will only show the effect of the external field. To evaluate the angular correlation for two-photon transitions in electric fields we employ Eq. (5.2) and the newly evaluated He-like transition amplitudes as well as the similar evaluated H-like transition amplitudes from [12]. This angle-differential decay rate depends both on the angle between the emitted photons as well as the direction of the electric field vector relative to these photons. I study this dependence by considering the angular correlation of different two-photon decay processes in an electric field in the different emission geometries we defined at the beginning of this chapter.

As the first case in Fig. 5.7 the angular correlation for the two-photon $2p_{1/2} \to 1s_{1/2}$ decay in H-like ions in the presence of an electric field of the strength F is shown. For this process I found no dependence of the differential decay rate on the used geometry, i.e. on the direction of the electric field. As I observed in [12] the angular correlation can be described, similar to the energy distribution of the photons, as an overlap of the angular correlations of the original $2p_{1/2} \to 1s_{1/2}$ and the induced $2s_{1/2} \to 1s_{1/2}$ two-photon process, which have been discussed in detail in previous works e.g. [4]. The interference terms in Eq. (5.2) apparently play no role. In this independence of the shape change of the angular correlation on the direction of the emission geometry my relativistic results differ from non-relativistic calculations [67]. These differences can be explained by the fact that in non-relativistic $2s \to 1s$ and $2p \to 1s$ transitions the total angular momenta of the intermixed initial states

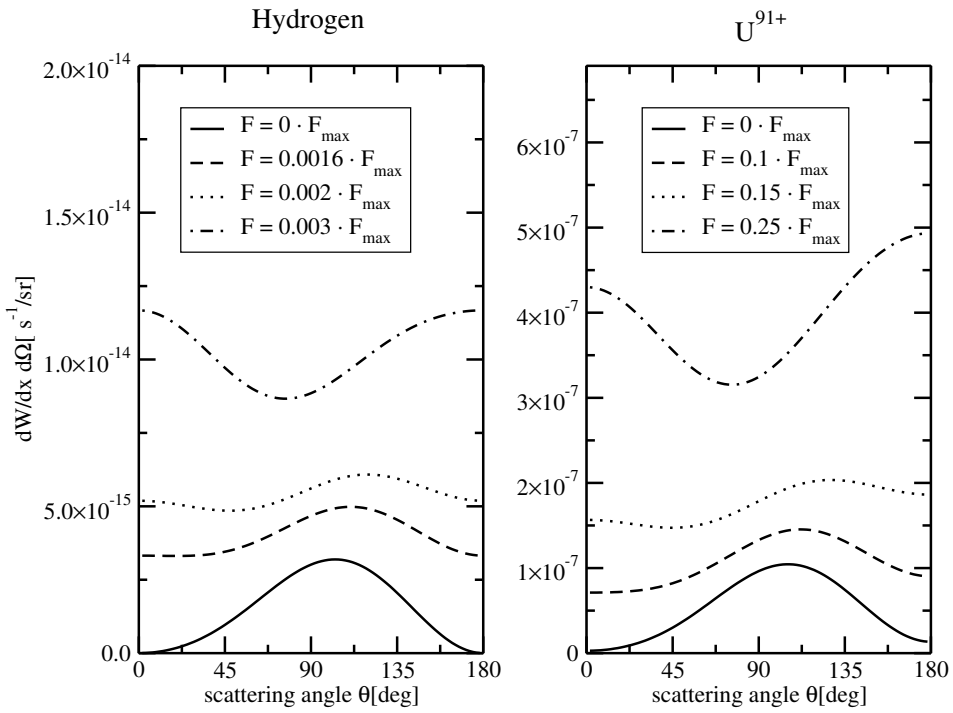

Fig. 5.7: Angle-differential decay rate for $2p_{1/2} \rightarrow 1s_{1/2}$ two-photon decay in neutral hydrogen (left panel) and U^{91+} (right panel) for equal energy sharing of the photons in the presence of an electric field. The field strengths F are given in units of the critical field strengths F_{max} (c.p. table 5.1). The angle differential decay rate does not depend on the direction of the electric field. (I here abbreviate the full triple differential rate (5.2) by $dW/dxd\Omega$)

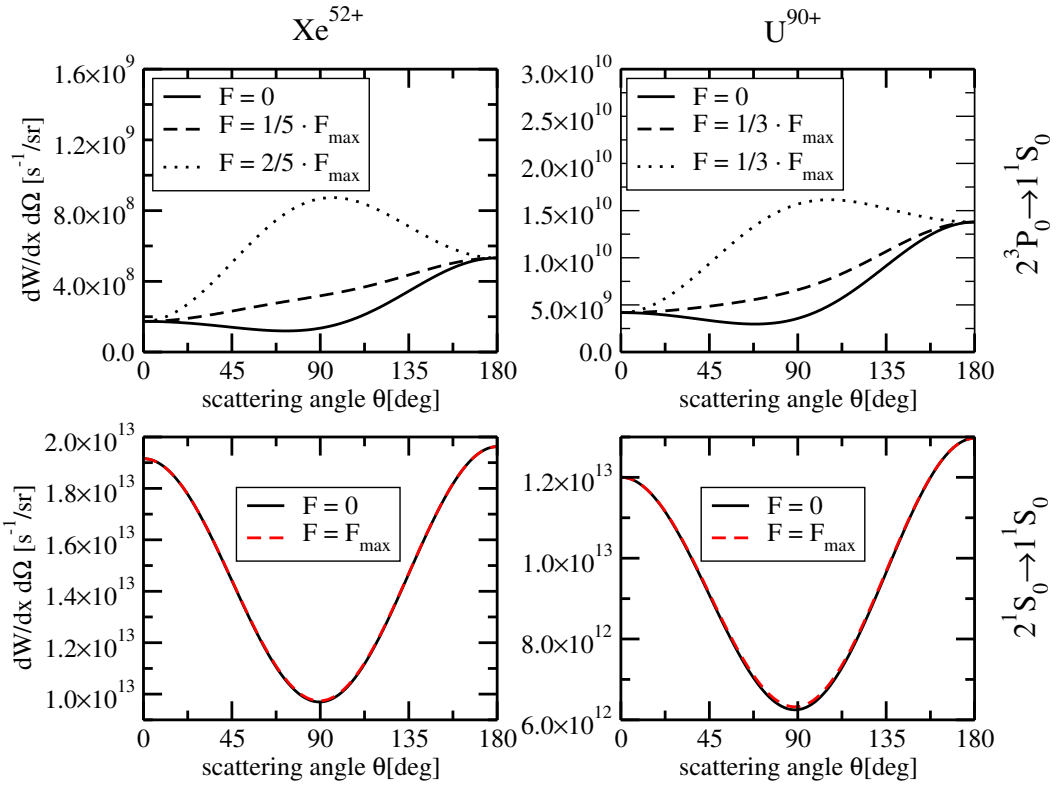

Fig. 5.8: Angular correlation for the $2^3P_0 \to 1^1S_0$ and $2^1S_0 \to 1^1S_0$ two-photon decay of Xe^{52+} and U^{90+} in an external electric field. Both photons are emitted perpendicular to the direction of the electric field and their energy sharing is $x = 1/4$. The electric field strength F is given in units of the critical field which can be found in table 5.1.

differ. Parts of a transition amplitude play a role that would in a relativistic approach correspond to the decay of the $2p_{3/2}$ state. As seen in Fig. 5.7 visible changes of the shape of the angular correlation happen at similar field strengths at which we also observed shape changes in the spectral distributions.

Such a rather simple effect of the electric field only appears in the perturbed $2p_{1/2} \to 1s_{1/2}$ two-photon decay in H-like ions. More interesting phenomena can be seen in the angular correlations of two-photon decay in He-like ions. As a baseline we consider in Fig. 5.8 the angular correlations for both the $2^3P_0 \to 1^1S_0$ and the $2^1S_0 \to 1^1S_0$ two-photon decay processes in Xe^{52+} and U^{90+} for an energy sharing of the photons of $x = 1/4$ and electric fields of different strengths which point perpendicular to the emission directions of the photons. We see from the Fig. 5.8 that for strong fields the shape of the angular correlation of the perturbed $2^3P_0 \to 1^1S_0$ decay process changes drastically both for Xe^{52+} as well as for U^{90+}. On the other hand, in the perturbed $2^1S_0 \to 1^1S_0$ process even in U^{90+} only minimal changes can be observed.

For He-like ions we observe that the effect of the electric field depends on the specific emission geometry, i.e. on its direction with respect to the emitted photons. To study this direction dependence in Fig. 5.9 the differential decay rate of both two-photon processes in U^{90+} is shown for different emission geometries. In the $2^1S_0 \to 1^1S_0$ process only the region around the angle $\theta \approx 90°$ is shown to improve the visibility of the effect of the external field.

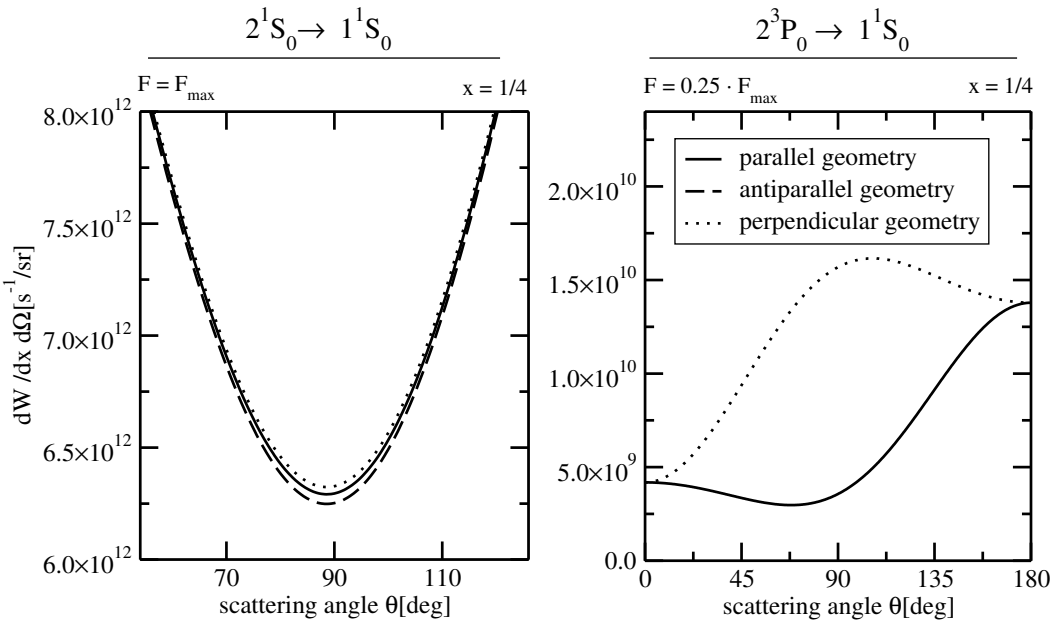

Fig. 5.9: Angular correlation for $2^1S_0 \rightarrow 1^1S_0$ (left panel) and $2^3P_0 \rightarrow 1^1S_0$ (right panel) two-photon decay of U^{90+} in the electric field F for different emission geometries and an energy sharing of the photons of $x = 1/4$. For a better visibility on the left panel only the section around $\theta = 90°$ is shown. The strength of the field F is given in units of the critical field strength F_{max} of each ion c.p. table 5.1.

The different emission geometries can be used to distinguish the perturbative contributions in Eq. 5.2. On the one hand there are interference terms in this equation that are linear in the field strength F. These contributions change their sign when we exchange F with $-F$, i.e. when the direction of the electric field is inverted. By comparing the angular correlation for parallel and antiparallel emission geometries in Fig. 5.9 we see that these interference contributions play a role only for the perturbed $2^1S_0 \rightarrow 1^1S_0$ two-photon decay where they lead to a slight separation of the "parallel" and "antiparallel" curves of the differential decay rates. For the perturbed $2^3P_0 \rightarrow 1^1S_0$ decay process the angular correlations in both the parallel as well as the antiparallel geometry have the same shape with a minimum around $90°$. Interference between the original and the induced two-photon decay channel seems to plays no role for the angular correlation in this process.

On the other hand, due to the quadratic purely induced contribution of Eq. (5.2), the differential decay rate of the $2^3P_0 \rightarrow 1^1S_0$ process has a completely different angular shape when both photons are emitted perpendicularly to the electric field or one photon is emitted (anti-)parallel to it, i.e. for perpendicular and (anti-)parallel emission geometries. Instead of the minimum at $\theta \approx 90°$ in the (anti)-parallel case for a perpendicular geometry there is a maximum at this angle. This dependence on the direction of the electric field arises from the $M_i = M_i^{ind}$ condition for the projections of the total angular momenta of the initial and induced next neighbor state in the Stark mixing coefficients (c.p. Eq. (5.2)). Due to this condition, if we choose a quantization axis along the direction of the electric field, the magnetic quantum number of the induced 2^3S_1 state has to be 0. The two-photon decay of the induced $2^3S_1 : M_i = 0$ state has therefore the angular correlation of the two-photon decay of a so-called "aligned" state. Such angular correlations depend strongly on the specific quantization axis, i.e. in our case on the direction of the electric field. This dependence

explains the differences between the angular correlations of the $2^3P_0 \rightarrow 1^1S_0$ two-photon transition for (anti-) parallel and perpendicular emission geometries. A similar but smaller effect can also be seen in the $2^1S_0 \rightarrow 1^1S_0$ process on the left side of Fig. 5.9.

5.1.4 Conclusion

The effect of external electric fields on spontaneous two-photon decay processes in H-like and heavy He-like ions was studied. The perturbative effect of the field is included by means of mixing the transition amplitude of the original unperturbed two-photon decay of a specific initial state with the two-photon decay amplitude of a state of opposite parity with a small energy difference to the initial state. The mixing coefficient between these contributions is given in terms of a so-called critical field strength that reaches from a small $478V/cm$ for mixing of the $2s_{1/2}$ and the $2p_{1/2}$ states in neutral hydrogen to fields that correspond to laser intensities of the order of $10^{22}W/cm^2$ in H- and He-like Uranium. For field strengths in the order of magnitude of the critical field strength we observe changes of the two-photon decay properties if the induced transition channel has at least a similar decay rate as the original one.

If also the effects of single photon decay are included, we notice that for many original and induced initial states the single photon transition actually dominates the decay process of the ions in the electric field. For strong fields these single photon contributions lead to diminishing lifetimes of the initial states. It is therefore not only difficult to observe the effect of the electric field on the two-photon transition but also some experimental approaches [3, 11] turn out to be not feasible.

Nonetheless, we can use two-photon decay as a useful toy model to study the effects of perturbation on two-photon processes. We find that for quantities that do not depend on the emission angles of the photons, like the energy distributions of the emitted photons, the perturbed system is an overlap of the original and the induced quantity, e.g. the original and induced energy distribution. Differences in these quantities can thus only be seen when e.g. the energy dependences of the two-photon decay of the original and next neighbor state have different shapes. However, in the angular correlation of the emitted photons such an overlap can only be seen for specific transition processes. Especially in two-photon decay of He-like ions I additionally observed interference between the original and induced two-photon decay channels. Furthermore, I found a dependence of the differential decay rate on the direction of the electric field that arises from the fact that if the quantization axis is parallel to the electric field the magnetic substates of the Stark induced "virtual" next neighbor state are fixed by the magnetic substates of the original unperturbed initial state. These leads to a possible virtual "alignment" of the induced next neighbor state that can be seen in the angular correlation.

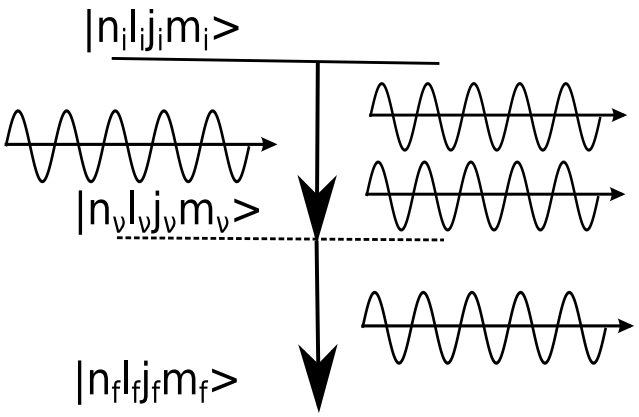

Fig. 5.10: Schematic description of enhanced two-photon decay. The initial state $|n_i l_i j_i m_i\rangle$ decays into the final state $|n_j l_f j_f m_f\rangle$ by simultaneously emitting two photon, one via induced transition (upper photons) and one via spontaneous transition (lower photon). This transition proceeds via the virtual intermediate state $|n_\nu l_\nu j_\nu m_\nu\rangle$. Here the n, l, j, m are the quantum number for the bound states of H-like ions from chapter 2.

5.2 Enhanced two-photon decay

5.2.1 Physics background and motivation

In the first part of this chapter I discussed the effect of static electric fields on two-photon decay. Apart from such static field effects it is interesting to consider the impact of a dynamic electromagnetic field on a two-photon transition process. For the single photon decay it is well known that the transition rates of a decay process can be enhanced by external radiation with a frequency that corresponds to the transition energy of the process. In such an external field the incident photons induce the emission of photons with the same properties. Similar phenomena can also affect the two-photon decay of excited states in an external field. Incident photons with an arbitrary frequency can induce a two-photon process known as singly stimulated or enhanced two-photon decay, c.p. Fig. 5.10. In analogy to the spontaneous two-photon decay this process is a transition of the ion with a simultaneous transmission of two-photons. However, in enhanced two-photon decay only one of the photons is emitted spontaneously. The emission of the other photon is induced by the incident radiation. The properties of this "induced" photon match precisely the properties of the incident photons. Employing singly stimulated two-photon transitions in experiments would therefore allow to control one of the photons in a two-photon process.
In the past enhanced two-photon decay was in light atoms or ions both in theory [13, 14, 57, 70] and experiment [71]. Also possible applications of the process e.g. in plasma physics [72] were discussed. Recently enhanced two-photon decay of highly charged heavy ions have attracted some attention. For example, in 1996 it was proposed by Dunford [11] to use an experimental setup based on singly stimulated two-photon decay to measure PNC violation in the low energy regime.

In order to explore the possibilities for this setup and also of other potential applications of enhanced two-photon decay, I performed a small relativistic study on the enhanced two-photon decay process in different H-like ions. In particular I focused on a potential measurement of the singly stimulated $2s_{1/2} \to 1s_{1/2}$ decay process and the dependence of such a possibility on the nuclear charge of the ion.

5.2.2 Theoretical description of enhanced two-photon decay

Enhanced two-photon decay is modeled in a very similar way as its spontaneous counterpart. The initial state decays to the final state by simultaneously emitting a photon with the energy ω_1 in an induced process and a spontaneously emitted photon with the energy $\omega_2 = E_f - E_i - \omega_1$. In a similar way as in the spontaneous two-photon decay these two photons can be described by means of the so-called energy sharing of the induced photon:

$$x = \frac{\omega_1}{E_i - E_f}. \tag{5.13}$$

The enhanced two-photon decay process is determined by same two-photon decay amplitude (4.3) as the spontaneous two-photon decay. In the evaluation of the enhanced (differential-) decay rate, however, special care must be taken of the photon normalization prefactors (3.8) of the decay operators $R^{1\,\dagger}_{\lambda_{1,2}}(\mathbf{k_{1,2}})$ from the definition of the electron photon interaction operator (3.9). These prefactors contain the factor $\sqrt{n_{\mathbf{k}\lambda}+1}$ that depends on the excitation $n_{\mathbf{k}\lambda}$ of a specific eigenmode of the initial electromagnetic field, with the wave vector $\mathbf{k}$ and the projection of the angular momentum of the mode on the propagation direction λ. For spontaneous decay we have $n_{\mathbf{k_2}\lambda_2} = 0$ and this factor is 1. The additional $n_{\mathbf{k}\lambda}$-dependent part is the origin of the induced or enhanced transition. By including these factors into the normalization constants the transition matrix elements from chapter 4 can be used in combination with Fermi's golden rule (3.45) to evaluate the differential decay rate of singly induced two-photon decay. In these calculations the direction, polarization, and frequency of one of the photons is determined by the incident electromagnetic wave (c.p. Fig. 5.10) and the density of the final state $d\rho_{1Ph}(\omega)$ (3.46) in Eq. (3.45) arises from the one spontaneously emitted photon. Under the assumptions that the incident photons are unpolarized and monochromatic, the magnetic substates of the excited initial state are equally occupied and neither the polarization of the outgoing photons nor the state of the ion after the decay process are measured, I average over the initial magnetic substates and sum over the final magnetic substates and the possible helicities of the photons. The rate is:

$$\frac{dW}{d\Omega_2} = \frac{\omega_2}{\omega_1}\frac{\alpha_S^2}{2j_i+1}\sum_{m_i m_f}\sum_{\lambda_1\lambda_2}\frac{n_{\mathbf{k}\lambda_1}}{V}\left|M_{fi}\right|^2, \tag{5.14}$$

with j_i the total angular momentum of the initial state and $n_{\mathbf{k}\lambda_1}$ the occupation number of the modes of the electromagnetic radiation before the enhanced decay process with polarization λ_1 and a wave vector of $\mathbf{k}$. Ω_2 defines the direction of the spontaneously emitted photon. The decay amplitude M_{fi} is identical to the amplitude I used in the first part of this chapter and can be evaluated by means of Eq. (4.3). At this point the large but finite volume V I introduced in the derivation of the electron-photon interaction operator (3.9) is still present.
Usually both the abstract photon occupation $n_{\mathbf{k}\lambda}$ numbers as well as the abstract "large

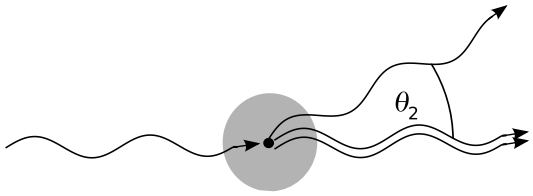

Fig. 5.11: Adopted geometry for a possible experiment on enhanced two-photon decay. The spontaneously emitted photon is observed at an angle θ_2 with respect to the direction of the incident and induced photons.

volume" V are not known. However, these impractical quantities can be expressed in terms of the more physical intensity of the incoming radiation I using Eq. (3.6). For unpolarized radiation we get:

$$\frac{dW}{d\Omega_2} = \frac{\omega_2}{\omega_1^2} \frac{\alpha_S^2}{2(2j_i+1)} I \sum_{m_i m_f} \sum_{\lambda_1 \lambda_2} |M_{fi}|^2 . \tag{5.15}$$

To discuss the enhanced two-photon decay without knowing the intensity of the incident light, it is useful to define a cross-section. Such a cross-section measures the number of spontaneous photons emitted into a specific direction by an enhanced two-photon process per unit of intensity of the incident beam. It is the quotient of the decay rate and the incident photon number intensity (I/ω_1):

$$\frac{d\sigma}{d\Omega_2} = \frac{dW}{d\Omega_2} \frac{\omega_1}{I} = \frac{\omega_2}{\omega_1} \frac{\alpha_S^2}{2(2j_i+1)} \sum_{m_i m_f} \sum_{\lambda_1 \lambda_2} |M_{fi}|^2 . \tag{5.16}$$

To compare enhanced two-photon decay with other decay processes not only such differential decay rates and cross-sections are needed but also the total angular independent transition rate. As we have seen in the first part of this chapter, such a total rate is obtained by an integration of Eq. (5.15) over all angles of the spontaneous emitted photon Ω_2.

5.2.3 Results and discussion

In an experimental study of enhanced two-photon decay excited ions would be irradiated by a laser with a photon energy of ω_1 and a fixed direction. These incident photons would induce the emission of photons with the same energy, direction (and polarization) as the laser. However, the second "spontaneous" photon would be emitted with a certain probability in all directions. To block out the intensity of the laser, such spontaneously emitted photons would therefore be measured at a certain angle θ_2 from the original beam. A schematic description of the geometry is shown in Fig. 5.11. At such an angle the spectrum of the emitted photons would be measured. On top of the well-known energy distribution of the spontaneously emitted photons, c.p. e.g. Fig. 5.5, the enhanced two-photon decay would become visible as an additional peak in the spectrum at an energy of $\omega_2 = (1-x)(E_f - E_i)$. A schematic illustration of such a spectrum is shown in Fig. 5.12.

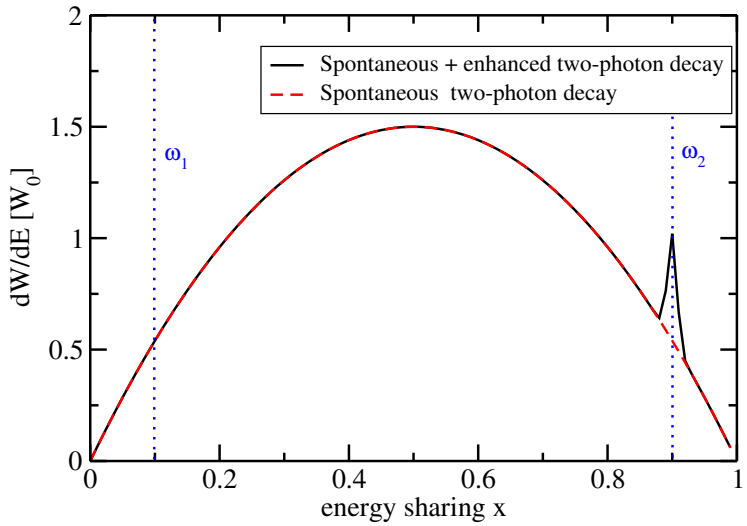

Fig. 5.12: .
Schematic illustration of the expected spectrum for an enhanced two-photon experiment (black solid line) if there is a strong laser whose photons have energies corresponding to an energy sharing of $x = 0.1$ (with some spectral width). For comparison a spectrum without enhanced two-photon decay is shown as a red dashed line.

To examine such a setup I evaluate the cross-sections and decay rates for the $2s_{1/2} \to 1s_{1/2}$ enhanced two-photon decay by means of the same numerical approximations for the two-photon decay amplitudes I used in the first part of this chapter. As the first step in the analysis of the enhanced two-photon decay process it is useful to know how the measuring angle θ_2 affects the cross-section of the process to determine acceptable geometries for such an experiment. This angular dependence needs to be compared to an uniformly spontaneously emitted spectrum as the ions are initially not oriented in our setup. To study this dependency I show in Fig. 5.13 the differential cross-section of the singly stimulated $2s_{1/2} \to 1s_{1/2}$ two-photon transition in neutral hydrogen and U^{91+} for an energy sharing of the induced photon of $x = 0.25$. On the left side of the figure we see that in neutral hydrogen the differential cross-section has a $d\sigma/d\Omega \sim 1 + cos^2(\theta_2)$ angular dependence. Such a behavior is typical for two-photon transitions dominated by electric dipole contributions (c.p. e.g. [4]) and is in perfect agreement with the previous non-relativistic results [13, 14, 57]. Thus while it would be optimal to measure the emitted photons at an angle of $\theta_2 = 180°$, i.e. in opposite direction to the propagation of the laser, even for the worst case of $\theta_2 = 90°$ the cross-section would only be half of the optimal value. The angular distribution of the spontaneously emitted photons arises from the same two-photon emission amplitudes that determine the angular correlations of spontaneous decay. Thus like in the differential decay rate of the spontaneous two-photon decay, we see on the right panel of Fig. 5.13 for heavy highly charged ions like U^{91+} the higher multipole effects slightly break the symmetry in the angular behavior of the differential cross-section. In a similar way a possible polarization dependence of the cross-section would be the same as the polarization sensitivity of the differential decay rate of the corresponding spontaneous two-photon decay process.

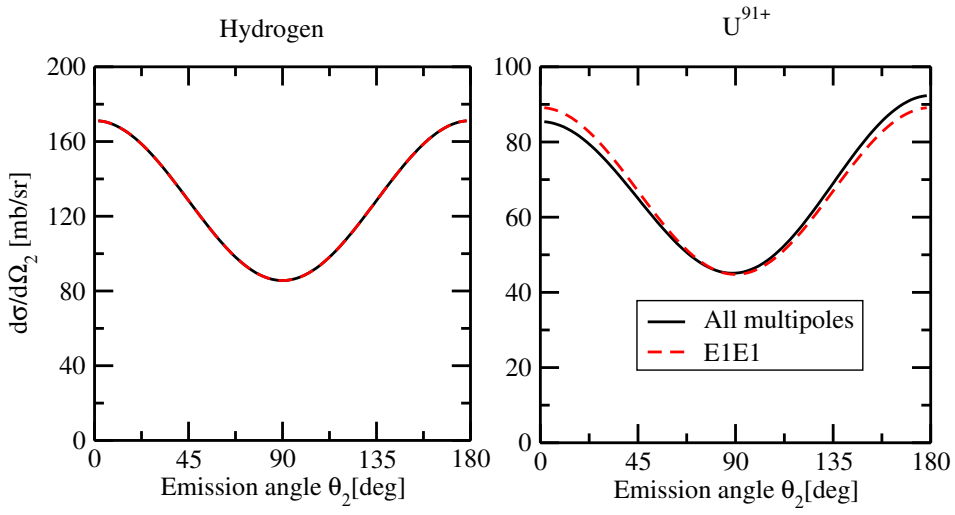

Fig. 5.13: Differential cross-section for $2s_{1/2} \to 1s_{1/2}$ enhanced two-photon decay in neutral hydrogen (left panel) and U^{91+} (right panel). Fully relativistic calculations including all multipole contributions (black solid line) are compared with a dipole-dipole approximation (red dashed line).

We furthermore observe in Fig. 5.13 that the absolute size of the cross-section does not depend strongly on the nuclear charge of the participating ion. For U^{91+} it is actually slightly smaller than for neutral hydrogen. To understand this behavior we notice that for the same energy sharing x the prefactor ω_2/ω_1 is constant and any dependence of the enhanced two-photon cross-section (5.16) on the nuclear charge Z of the ion can only arise from the transition amplitudes. In $2s_{1/2} \to 1s_{1/2}$ two-photon transitions these amplitudes are dominated by the leading order E1E1 multipole contribution. The size of such dipole-dipole amplitudes does not depend, in leading order, on the nuclear charge Z, neither does the cross-section (see also chapter 6.2). The slight reduction of the cross-section in U^{91+} arises from relativistic effects that lead to slightly smaller transition amplitudes for heavy targets in the fully relativistic description when compared to a non-relativistic model; for spontaneous two-photon decay such a behavior was observed e.g. by Goldman [9].

For a potential experiment it is not only important to know the dependence of the cross-section on the emission angle and the nuclear charge of the target, but even more vital is its energy dependence. In Fig. 5.14 I show such an energy dependence of the differential cross-section in neutral hydrogen (black solid line) and U^{91+} (black dashed line). To compare my results with previous non-relativistic calculations by e.g. Heno [14] (red crosses), I consider the cross-section for an angle of $\theta_2 = 90°$ between the induced and spontaneously emitted photons. As we can see from the black solid line and the red crosses in Fig. 5.14, these previous calculations are in perfect agreement with my results for neutral hydrogen. All graphs in Fig. 5.14 show a similar energy dependence of the differential cross-section. It is enhanced if the induced photon carries a small share of the transition energy and more and more suppressed for larger energy sharing x of the induced photon. Such an energy dependence is in strong contrast to the energy shape of the spectral distribution of the emitted photons in spontaneous two-photon decay, c.p. Fig. 5.5. This different behavior arises mainly from the fact that for enhanced two-photon decay the phase space density $d\rho_{1Ph}$ of the spontaneous transition becomes much smaller for smaller spontaneous photon

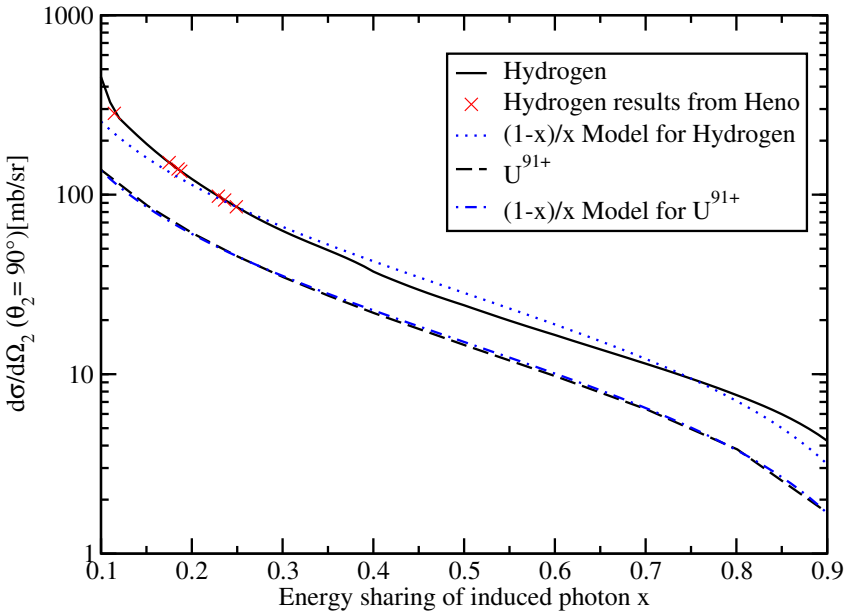

Fig. 5.14: Energy dependence of the differential cross-section for $2s_{1/2} \to 1s_{1/2}$ enhanced two-photon decay at $\theta_2 = 90°$ in neutral hydrogen (black solid line) and U^{91+} (black dashed line). The energy is given in terms of the energy sharing x of the induced photon. For comparison the results of Heno [14] are included as red crosses. Furthermore I compare the evaluated energy distributions with the simple $(1-x)/x$ model derived from the prefactors of Eq. (5.16). This model is normalized to the cross-section of hydrogen (blue dotted line) and U^{91+} (blue dashed dotted line) at $x = 0.25$.

energies while in spontaneous two-photon decay the size of the two-photon phase space density is affected by the energies of both photons. The phase space contribution leads to a ω_2/ω_1 prefactor in the definition of the enhanced two-photon cross-section (5.16). Because of the energy conservation, i.e. $\omega_1 + \omega_2 = E_i - E_f$, for a hypothetical constant transition amplitude, such a prefactor would lead to an energy dependence of the cross-section of the form: $d\sigma/dx \sim (1-x)/x$. A comparison of a simple model based on such an energy dependence (blue dotted and dashed dotted line) with my results shows that for a moderate energy sharing of the induced photon $0.2 < x < 0.8$ this prefactor dominates the energy dependence of the cross-section. This model is an especially good description for the somewhat smaller cross-sections of enhanced two-photon decay in U^{91+}.

As I mentioned in the first part of this section, enhanced two-photon decay has been observed experimentally in neutral hydrogen. To explore the possibility of measuring this process in heavy highly-charged ions, we need to estimate the intensity of a laser required for such an experiment. As a first naive approach I assume that in order to be able to see singly stimulated two-photon decay its transition rate must be of the same order of magnitude as other spontaneous processes that depopulate the initial excited $2s_{1/2}$ state. I evaluate the intensity required to achieve such a rate by comparing the total enhanced two-photon decay rate (the integral of Eq. (5.15 over all angle of the spontaneously emitted photon) with the spontaneous $2s_{1/2} \to 1s_{1/2}$ two-photon decay rate from Goldman [9]. In table 5.4 the required intensities I are shown for different target ions. I here assume that the incident light has a frequency corresponding to $x = 1/4$ of the transition energy of the ion.

	Hydrogen	Ne^{9+}	Fm^{99+}
$I[W/cm^2]$	$9.43 \cdot 10^6$	$9.47 \cdot 10^{14}$	$1.77 \cdot 10^{23}$

Tab. 5.4: Intensities I for which the enhanced and spontaneous $2s_{1/2} \to 1s_{1/2}$ two-photon decay rates have the same size in different ions. The photons of the incident beam have an energy of $\omega_1 = 1/4(E_f - E_i)$ and the spontaneous two-photon rates are taken from [9]

The table shows that the required intensity I grows rapidly with the nuclear charge Z of the decaying ion. As I found that the transition cross-section is only minimally affected by changes in Z this $I \sim Z^8$ proportionally is purely caused by a similar increase of spontaneous $2s_{1/2} \to 1s_{1/2}$ two-photon decay rate. While intensities (as in table 5.4) are easily accessible for light ions, for heavy H-like ions the fields become extremely strong and would affect the structure of the ions as shown in the first part of this chapter. A measurement would be difficult.

Fortunately, methods to lower the very conservative estimate of the required intensity can be imagined. On the one hand I showed that the enhanced two-photon cross-section strongly depends on the frequency of the incident radiation. By lowering the frequency of the laser, e.g. from $x_a = 1/4$ to $x_b = 1/40$, the cross-section increases by $\frac{\sigma_b}{\sigma_a} \approx 10$ and the required intensity becomes smaller by that factor. This method is limited by the fact that in the limit of $x \to 0$ the enhanced two-photon process becomes a Stark induced single photon decay as we discussed in the first part of this chapter.
On the other hand, in a realistic experimental setup the enhanced two-photon decay process would be observed by measuring the spectrum of the combined spontaneous and enhanced two-photon decay. In such a spectrum the spontaneous photon of the singly stimulated transition would be visible as a resonance at an energy sharing of $(1 - x)$, c.p. Fig. 5.12. In such experiments a laser intensity would be sufficient at which the enhanced two-photon decay rate would be comparable to the spontaneous decay rate in that spectral region. With an adequate control of the frequency of the incident laser and a sufficient spectral resolution of the detectors in this approach it might be possible to lower the required intensity by $3 - 5$ orders of magnitude and make a measurement of enhanced two-photon decay in mid-Z H-like ions theoretically feasible with near term x-ray sources. However, to my knowledge there are currently no plans for a facility that would combine such high quality x-ray sources with the ability to create and store enough excited highly charged heavy ions. Such efforts would be further obstructed by the short lifetime of the $2s_{1/2}$ state in highly charged ions. For high-Z ions additional to advances in experiments a more detailed theoretical analysis of side effects of the strong dynamic laser fields, as in the first part of this chapter, would be necessary.

5.2.4 Conclusion

I studied the effect of dynamic electromagnetic fields (or in other words external radiation) on the two-photon decay of H-like ions. In such fields an exotic two-photon process appears in which the emission of one on the two photons is induced by the radiation. I examined the properties of this so-called enhanced two-photon decay with a relativistic approach and

explored a possible measurement. I found that the properties depending on the emission angles (and the polarization) of the photons arise from the two-photon transition amplitude and behave similarly as analogous properties in the spontaneous two-photon decay. As the properties of one of the emitted photons is determined by the incident radiation, singly stimulated two-photon decay offers thus the opportunity to control some parameters of the two-photon decay process. To measure such a process we would look for an additional peak in the spectrum of the measured photons of a two-photon decay that originates from the spontaneously emitted photons of the induced process. For such experiments it is useful to understand the angular and energy dependence of the so-called cross-section of the process, i.e. the probability that an incident photon causes the "spontaneous" emission of a photon in a certain direction. I found that the cross-section changes by the factor of 2 depending on the angle at which the spontaneously emitted photon is measured. The energy dependence of this cross-section is even more pronounced and becomes larger for smaller incident photon energies. Interestingly, the cross-section for such a singly stimulated two-photon process depends only weakly on the nuclear charge of the participating ion. However, in an experiment the competing spontaneous two-photon decay rate rises very fast with the nuclear charge Z of the ion. Thus, even though an observation of enhanced two-photon decay has been possible in neutral hydrogen [71] with the simple lasers of the 1970s, a measurement in mid - and high-Z H-like ions with high power x-ray lasers would be challenging today. In theory, by observing the spectral distribution of two-photon decay in a strong x-ray laser field, it might be possible to observe this effect in such heavy ions. However for a practical realization it might be difficult to provide a facility that is able to produce a sufficient number of ions in the required short-living state in a very strong monochromatic x-ray field.

The photon scattering experiments I discuss in the next chapter offer a similar level of control over the two-photon process, but only require H-like ions in the ground state and are thus more easily experimentally accessible.

6 Scattering of photons by highly charged heavy ions

Two-photon processes can be used to examine interesting but weak physical effects. For such studies it is very useful if the properties of at least one of the photons of the two-photon process can be externally determined. In the previous chapter it was shown that, while external electromagnetic fields can be used to exert some control on two-photon transitions, due to side effects of such fields and the short lifetimes of the excited states an experimental realization may be difficult to accomplish.

The elastic or inelastic scattering of photons by atoms or ions can be theoretically described by means of a similar second-order approach which allows to specify the properties of the incident photon. However, these processes do not require a source of excited ions and very strong radiation and are thus experimentally easier to access than e.g. enhanced two-photon decay. To explore what kind of interesting effects can be measured in such scattering processes, I present in the first part of this chapter results from a theoretical study [55] on elastic Rayleigh scattering of polarized light by H-like heavy ions. This study was performed by a collaboration to which I contributed as part of my doctorate research work. Furthermore, I also consider in the second part of this chapter inelastic Raman scattering in which energy is deposited in the target ion. In this part the results of a relativistic study on inelastic Raman scattering by H-like ions [56] performed by me are presented.

6.1 Polarization transfer in elastic Rayleigh scattering

6.1.1 Physics background and motivation

Rayleigh scattering is the elastic scattering of photons by electrons bound in the field of a nucleus. It has been studied extensively for both light and heavy atoms as targets [15, 16, 17, 18, 19, 20]. Recently, with the availability of polarized x-ray sources like PETRA III and polarization sensitive x-ray detectors, the dependence of the elastic cross-sections on the polarization of the photons has attracted special attention. Previous to our study the topic of a polarization dependence of the elastic cross-section had mostly been examined for scattering by light neutral atoms e.g. [21]. We extended the research on this topic to highly charged heavy ions and analyzed such a polarization sensitivity for elastic Rayleigh scattering on the ground state electrons of heavy H-like ions. In this study we used the relativistic approach introduced in chapter 3 and 4. Special attention was payed to the linear polarization of the scattered photon for a linear polarized incident radiation.

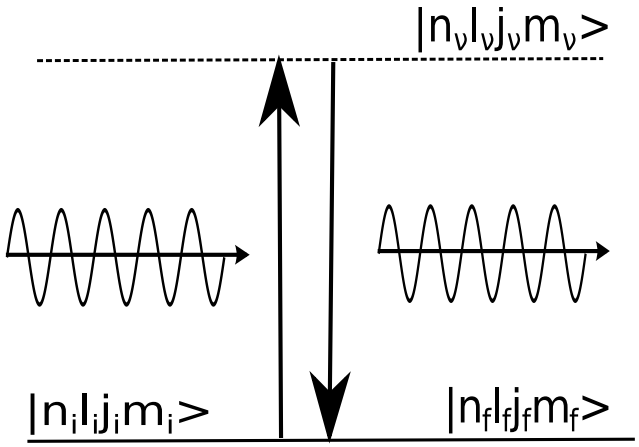

Fig. 6.1: Schematic description of elastic Rayleigh scattering. The scattering process proceeds by the absorption and emission of a photon via a virtual intermediate state $|n_\nu l_\nu j_\nu m_\nu\rangle$. The initial bound state $|n_i l_i j_i m_i\rangle = |n_f j_f l_f m_f\rangle$ is not (energetically) changed in this process. The n, l, j, m are the quantum number for bound states of H-like ions, c.p. chapter 2.

6.1.2 Theoretical description of Rayleigh scattering of linear polarized photons

Elastic scattering of photons by atoms or ions can be theoretically described, like two-photon decay, by means of second-order perturbation theory. Such a scattering process consists of a simultaneous absorption and emission of photons with the same frequency, c.p. Fig. 6.1. As I discussed in chapter 3 and 4, it can be modeled by means of a scattering amplitude. However, with the transition amplitude (4.15) it is only possible to describe circular polarized photons. To be able to study the linear polarization $\boldsymbol{\epsilon}_2$ of photons for incident $\boldsymbol{\epsilon}_1$ linear polarized light, we need to include the polarization expansion parameters ϵ_i^λ that were introduced in Eq. (3.17) and Eq. (3.18). With these parameters and the scattering amplitude (4.15) we can construct a scattering amplitude for linear polarized photons:

$$M_{fi}^{sc;linear} = \sum_{\lambda_1 \lambda_2} \epsilon_1^{\lambda_1} \epsilon_2^{\lambda_2 *} M_{fi}^{sc}, \tag{6.1}$$

Such a scattering amplitude and Fermi's golden rule (3.45) allows us to define a scattering rate for a well-defined incident radiation. In analogy to the derivation of the cross-section for the enhanced two-photon decay (5.16), we carefully consider the $\sqrt{n_{\mathbf{k}\lambda}}$ prefactor of the absorption operator and the abstract volume V. By introducing an intensity of the incident beam and by dividing the transition rate by the photon number intensity we can define the cross-section for the elastic scattering process. Similar to our derivation of the enhanced two-photon decay cross-section, the propagation direction of the incident photon is fixed and the state density in Eq. (3.45) is the density for a spontaneous emission of a single photon (3.46). In contrast to the enhanced two-photon decay, in elastic scattering both the incident as well as the scattered photon have the same energy and the ω_2/ω_1 prefactor does

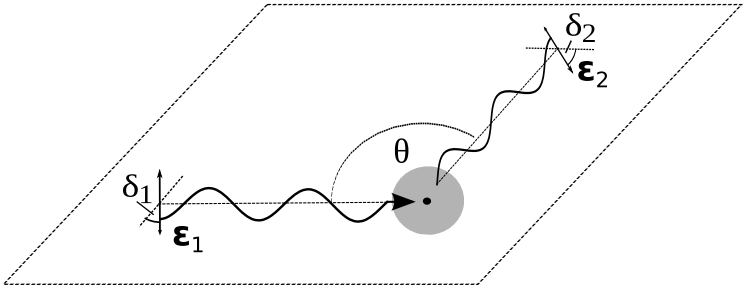

Fig. 6.2: Employed geometry for elastic scattering of a polarized photon by an ion.

not appear. Thus the angle-differential cross-section for elastic scattering of photons with the polarization $\boldsymbol{\epsilon}_1$ into a photon state with polarization $\boldsymbol{\epsilon}_2$ is given by:

$$\frac{d\sigma}{d\Omega} = \frac{\alpha_S^2}{2j_i+1} \sum_{m_i m_f} \left| \sum_{\lambda_1,\lambda_2} \epsilon_1^{\lambda_1} \epsilon_2^{\lambda_2 *} M_{fi}^{sc} \right|^2 , \tag{6.2}$$

with M_{fi}^{sc} the scattering amplitude (4.15) for circular polarized photons with the same initial and final state, $j_i = 1/2$ the total angular momentum of the initial (ground) state, and Ω the direction of propagation of the scattered photon.

In this representation the cross-section depends both on the polarizations of the incident and scattered photons as well as on their scattering angle. On top of such polarization sensitive cross-sections also elastic cross-sections are needed that do not depend on the polarization of the scattered photons. Such cross-sections are evaluated by summing over a set of orthogonal final polarizations. Also we need to consider cross-sections when the incident radiation is not completely polarized. In this case a weighed sum of the cross-sections for orthogonal incident polarizations must be evaluated.

Geometry and Stokes parameters

Here we examine the linear polarization of the incident and scattered photons in an elastic scattering process. For a meaningful discussion of such polarization the setup of the elastic scattering problem must be carefully defined. Our setup is shown Fig. 6.2. Photons with the linear polarization $\boldsymbol{\epsilon}_1$ are scattered by the angle θ. The scattering plane is tilted by the angle δ_1 with respect to the polarization of the incident photon. The polarization of the scattered photon $\boldsymbol{\epsilon}_2$ is measured by means of a detector which is sensitive to polarizations tilted with respect to the scattering plane by the angle δ_2. As an example it is very convenient to define two specific polarization directions: for an angle $\delta_2 = 0°$ or $\delta_1 = 0°$, i.e. when the polarization vector lies in the scattering plane, we talk about coplanar or x-polarized photons. Photons with a polarization vector perpendicular to this plane, i.e. $\delta_2 = 90°$ or $\delta_1 = 90°$, are called y-polarized.

To characterize the polarization of the scattered photons it is useful to introduce the well-known Stokes parameters [35]. These Stokes parameters are a set of numbers ($-1 \leq P_i \leq 1$)

that completely define the polarization of an ensemble of photons. They consist of two parameters that describe the linear polarization with respect to the scattering plane and $45°$ tilted to it

$$P_1 = \frac{w_x - w_y}{w_x + w_y}\,, \tag{6.3}$$

$$P_2 = \frac{w_{45°} - w_{135°}}{w_{45°} + w_{135°}}, \tag{6.4}$$

and one parameter that describes circular polarization

$$P_3 = \frac{w_{+1} - w_{-1}}{w_{+1} + w_{-1}}. \tag{6.5}$$

Here $w_{x,y,45°,135°}$ are the probabilities to measure a photon with a detector only sensitive to a specific linear polarization, e.g. $\delta_2 = 45°$, or a specific circular polarization $w_{\pm 1}$. These parameters also allow to define a degree of polarization $P = \sqrt{P_1^2 + P_2^2 + P_3^2} \leq 1$ and a degree of linear $P_L = \sqrt{P_1^2 + P_2^2}$ polarization.

In the context of x-ray scattering on highly-charged ions an experimental determination of a degree of circular polarization of the scattered photon is not practical. Therefore in this thesis I only consider the linear polarization of the scattered photons, i.e. the Stokes parameters P_1 and P_2. For a photon scattering process these Stokes parameters are determined by cross-sections for elastic scattering into suitable polarized photon states. They are given by:

$$P_1 = \frac{\frac{d\sigma}{d\Omega}_{\delta_2=0°} - \frac{d\sigma}{d\Omega}_{\delta_2=90°}}{\frac{d\sigma}{d\Omega}_{\delta_2=0°} + \frac{d\sigma}{d\Omega}_{\delta_2=90°}}, \tag{6.6}$$

and

$$P_2 = \frac{\frac{d\sigma}{d\Omega}_{\delta_2=45°} - \frac{d\sigma}{d\Omega}_{\delta_2=135°}}{\frac{d\sigma}{d\Omega}_{\delta_2=45°} + \frac{d\sigma}{d\Omega}_{\delta_2=135°}}. \tag{6.7}$$

Non-relativistic approximation of Rayleigh scattering

In the results of our study relativistic and higher multipole effects have a major influence on the polarization of the scattered photons. For comparison it is therefore useful to define a simple non-relativistic dipole model as a baseline. The non-relativistic dependence of the elastic cross-section on the propagation direction and polarization of the incident and scattered radiation was worked out a long time ago in an approach based on classical electrodynamics. In this approach it is assumed that the polarized radiation induces an oscillating electric dipole in the target and the scattered light is the classical electromagnetic far field radiation of this dipole [64]. The results of this classic approach have be proven to remain valid also in a non-relativistic quantum mechanical dipole model [22, 44, 73]. Within these simple dipole models the angular and polarization dependence of the elastic cross-section can be written as, c.p. chapter 10 in [64]:

$$\frac{d\sigma}{d\Omega} \sim \left|\boldsymbol{\epsilon}_1 \boldsymbol{\epsilon}_2\right|^2. \tag{6.8}$$

Here the polarization vectors $\epsilon_{1,2}$ of the incident and scattered photon are defined with respect to some common coordinate system. They specify both the dependence on the polarization of the photons as well as the angle between them.

By including explicit polarization vectors into this equation a non-relativistic (classical) baseline for the angular dependence of the Stokes parameters of the scattered photons can be determined. In the employed geometry we defined in the preceding paragraph, a non-relativistic approximation of the Stokes parameters is given by:

$$P_1^{nr} = \frac{-\sin^2\delta_1 + \cos^2\delta_1\cos^2\theta}{\sin^2\delta_1 + \cos^2\delta_1\cos^2\theta}, \tag{6.9}$$

and

$$P_2^{nr} = \frac{2\sin\delta_1\cos\delta_1\cos\theta}{\sin^2\delta_1 + \cos^2\delta_1\cos^2\theta}. \tag{6.10}$$

The non-relativistic model allows us to define the expected angular behavior of the Stokes parameters. For example, we see from Eq. (6.9) and (6.10) that for coplanar polarization of the incident photons we have $P_1 = 1$, i.e. the scattered photons are also fully polarized within the scattering plane. Small tilts of the incident polarization however can lead to a drop in the polarization of the scattered photon near $\theta = 90°$. For coplanar or y-polarized incident radiation the parameter $P_2 = 0$ vanishes for all angles, i.e. there is no preference of the $\delta_2 = 45°$ polarization over the $\delta_2 = 135°$ polarization. In contrast to this scattering of photons with a polarization in the scattering plane for intermediate tilt angles δ_1 both P_1 and P_2 show a distinct dependence on the scattering angle θ. I now compare these non-relativistic results with our relativistic calculations.

6.1.3 Results and discussion

To begin the analysis of the angular dependence of the polarization of the scattered photons, numerical approximations for the scattering cross-sections were evaluated. These cross-sections are determined by means of reduced matrix elements for two-photon absorption that were evaluated by Vladimir Yerokhin, a member of the collaboration, using his advanced Greens function approach. With these reduced matrix elements Eq. (4.3) was used to determine the scattering amplitudes. Finally, these amplitudes were used to determine the cross-sections using Eq. (6.2). Precise numerical approximations for the scattering of photons with an energy of $1.1E_{ion}$, $5E_{ion}$ and $10E_{ion}$ by ground state electrons in Ne^{9+}, Xe^{53+} and U^{91+} were evaluated. Here I introduced the ionization energy of the ground state E_{ion} of the target ion as a natural energy scale for the photons. We have for Ne^{9+} $E_{ion} \approx 1.36keV$, for Xe^{53+} $E_{ion} \approx 41.35keV$, and for U^{91+} $E_{ion} \approx 132.29keV$. Reasonable results required, especially at high photon energies and heavy targets ions, to include all multipole contributions up to $L = 10$.

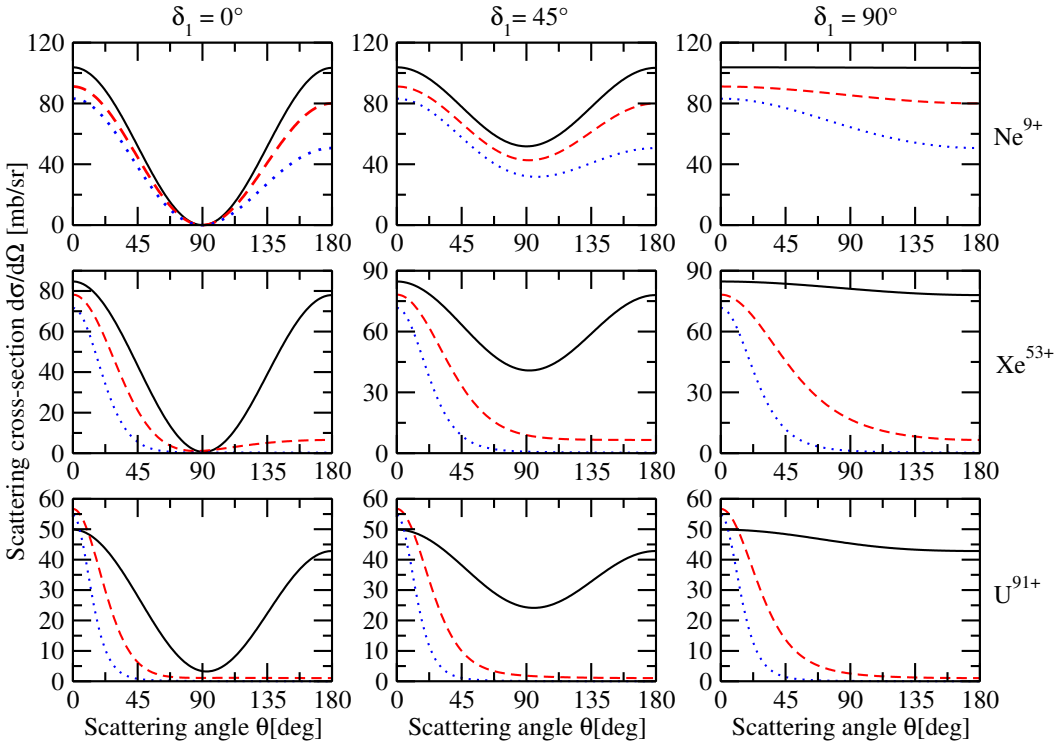

Fig. 6.3: Angular distribution of elastically scattered photons for polarized incident radiation with photon energies of $1.1 \cdot E_{ion}$ (black solid lines), $5 \cdot E_{ion}$ (red dashed line) and $10 \cdot E_{ion}$ (blue dotted lines) and different tilt angles δ_1 between the polarization of the incident photons and the scattering plane (columns) as well as different targets (rows).

Angular distribution of the scattered photons

As a first step in the examination of polarization related effects in Rayleigh scattering the angular-differential cross-sections for elastic scattering of polarized photons is considered. I show in Fig. 6.3 these cross-sections for incident polarized photons. Results are presented for scattering of photons with an energy of $1.1 \cdot E_{ion}$ (black solid line), $5 \cdot E_{ion}$ (red dashed line), and $10 \cdot E_{ion}$ (blue dotted line) by Ne^{9+} (top row), Xe^{53+} (middle row), and U^{91+} (bottom row). Furthermore, the graph shows in its columns calculations for incident photons with linear polarizations tilted by different angles δ_1, namely for a polarization in the scattering plane $\delta_1 = 0°$, perpendicular to it $\delta_1 = 90°$, and in the middle of these two extremes $\delta_1 = 45°$. In Fig. 6.3 we see that for low incident photon energies and light targets (top row black solid line) the angular behavior of the differential cross-section is well described by the non-relativistic dipole model (6.8) that was derived in the previous section. Specifically we see, as this simple model predicts, that for the polarization tilt angle $\delta_1 = 0°$ the angular distributions has a $d\sigma/d\Omega \sim \cos^2\theta$ angular dependence, for $\delta_1 = 45°$ it has a $d\sigma/d\Omega \sim 1 + \cos^2\theta$ dependence, and for $\delta_1 = 90°$ the cross-section does not depend on the scattering angle θ.

For higher energies of the scattering photon and heavier targets relativistic and higher multipole effects become important. As an example we observe in the lower right panels of Fig. 6.3 that due to these effects at low energies the cross-section for $\delta_1 = 0°$ coplanar scattered photons does no longer vanish at a scattering angle of $\theta = 90°$.

For higher photon energies even more drastic changes in the shape of the angular distribution can be seen. The angular shapes become asymmetric as the scattering for low angles is enhanced and backscattering is suppressed. If the photons have a very high energy, especially if they are scattered by heavy highly-charged ions, the differential cross-section is dominated by this higher multipole effects and the minima at $\theta = 90°$ of the non-relativistic model become invisible.
The observed dependence of the angular distribution on the energy of the scattered photons is in good agreement with the results of previous works [15, 16, 17, 18, 19].
I now use the observations of the angular behavior of these cross-section as a basis to discuss the angular behavior of the polarization of the scattered photons.

Polarization correlations in Rayleigh scattering

Modern experiments can not only measure the angular distribution of scattered photons, but also correlations between the polarization of the incident and scattered photons. In this work these correlations are examined by studying the angular dependence of the P_1 and P_2 Stokes parameters of the scattered photons for different linear polarization directions of the incident photons.

To understand the behavior of these Stokes parameters I consider, as a baseline, elastic scattering by light ions. Fig. 6.4 shows the P_1(top row) and P_2(bottom row) Stokes parameters of photons with an energy of $1.1 \cdot E_{ion}$(black solid line) and $10 \cdot E_{ion}$(blue dashed line) elastically scattered by Ne^{9+}. I included the results for different initial polarizations of the photons in the columns of Fig. 6.4. On top of that, for reference, on the top left panel the non-relativistic result (green solid line) from Eq. (6.9) is included.
In the bottom row of Fig. 6.4 we see that the angular shape of the P_2 parameter does not depend on the energy of the incident photon. For scattering of light with a polarization in or perpendicular to the scattering plane it vanishes for all angles θ, i.e. $P_2 = 0$, and in the $\delta_1 = 45°$ case we observe a smooth symmetric transition of P_2 from $P_2 = 1$ at low scattering angles to $P_2 = -1$ at $\theta = 180°$. These angular shapes are in perfect agreement with the non-relativistic result from Eq. (6.10).
In a similar way the results for the P_1 parameter for a tilted ($\delta_1 = 45°$ or $\delta_1 = 90°$) polarization agrees with the non-relativistic results from Eq. (6.9). However, we can see in the top left panel of Fig. 6.4 that for coplanar scattering, i.e. when the incident photons are x-polarized, relativistic solutions do not agree with the simple nonrelativistic results. While, according to the non-relativistic model, we should have $P_1 = 1$ for all possible scattering angles, we observe in our non-relativistic results a depolarization of photons for $\theta \approx 90°$. This depolarization becomes stronger for higher photon energies.

In order to understand this behavior we remember that the Stokes parameters are evaluated from cross-sections for specific initial and final polarizations of the photons (6.6). The angular behavior of P_1 can therefore be traced back to behavior of the elastic cross-section for the scattering of different incident polarized photons into specifically polarized scattered photon states. To examine this behavior I show in Fig. 6.5 the relevant cross-sections for elastic scattering of a photon with an energy of $1.1 \cdot E_{ion}$ by Ne^{9+}. Specifically, these cross-sections are the ones in which the initial polarization of the photon lies either in the

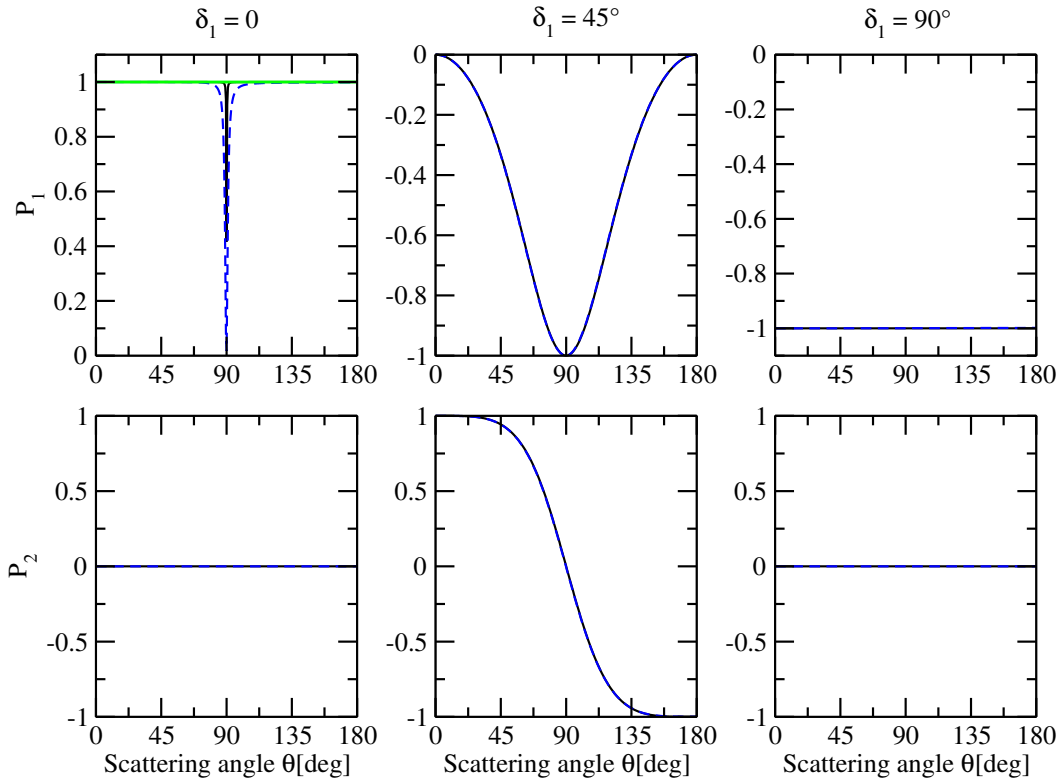

Fig. 6.4: P_1 (top row) and P_2 (bottom row) Stokes parameters for elastic scattering of photons by Ne^{9+} with an energy of $1.1E_{ion}$(black solid line) and $10E_{ion}$(blue dashed line) for different tilt angles δ_1 (columns) of the polarization of the incident photon. On the top left panel the non-relativistic result from Eq. (6.9) is included for reference as a green solid line.

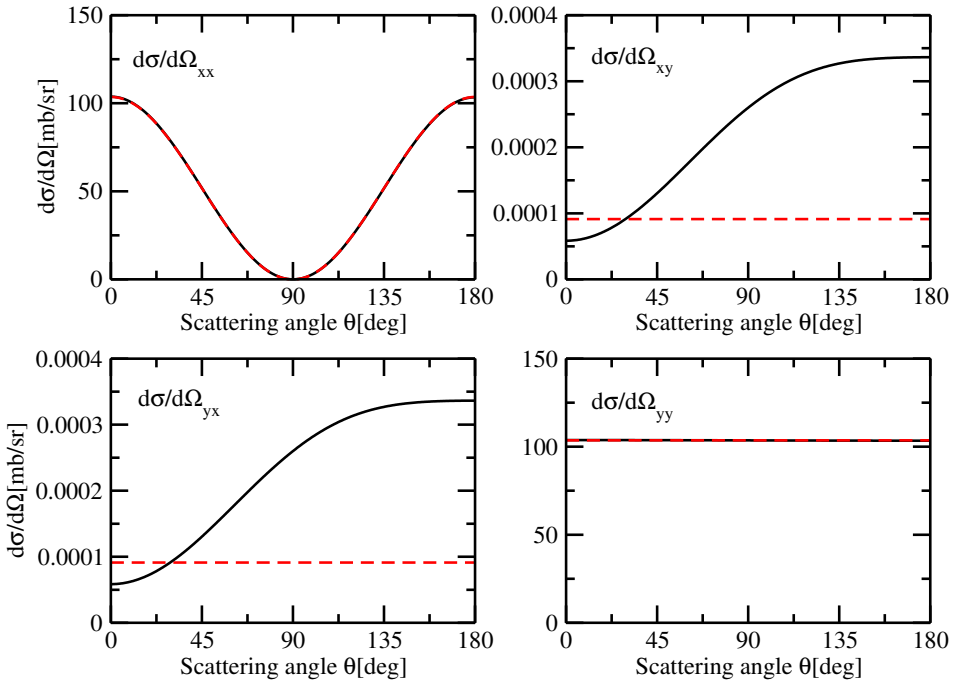

Fig. 6.5: Cross-sections for elastic scattering of photons with the energies of $1.1 \cdot E_{ion}$ by Ne^{9+} and different polarizations of the incident photon (x or in the scattering plane in the top row; y or perpendicular to the scattering plane in the lower row) and the outgoing photon (x in the left column; y in the right column). Calculations involving all multipoles (black solid line) are compared with relativistic E1E1 calculations (red dashed line).

scattering plane (x-polarization) or perpendicular to it (y-polarization) and we observe similar x- or y-polarization of the scattered photons.

Fig. 6.5 shows that for the cross-sections where the incident and scattered photon have the same polarization higher multipole effects play no visible role and their angular behavior can be reasonably well described by the non-relativistic dipole approximation. We have a $d\sigma/d\Omega \sim \cos^2\theta$ behavior when both photons are polarized in the scattering plane and a constant non-zero cross-section if both photons are y-polarized. Additionally, relativistic contributions add to both cross-sections a small non-zero constant that can not be seen at this scale.

In contrast to the non-relativistic description, we observe in the off diagonal panels of Fig. 6.5 angular dependent non-vanishing cross-sections for the observation of e.g. scattered y-polarized photons when the initial photons are x-polarized. These non-zero cross-sections are caused both by relativistic and higher multipole effects and are connected to a spin-flip of the ground state electron. As such spin-flips are not possible in fully occupied electron shells, the "xy"-cross-sections are only non-zero in certain few-electron ions such as H-like ions.

If we now consider elastic scattering of coplanar polarized light, we see that at a scattering angle of $\theta \approx 90°$ the "xx"-cross-section vanishes (up to tiny relativistic and higher multipole contributions) while the size of the "xy"-cross-section remains finite. According to the definition of P_1 (6.6) the scattered photons are therefore not x-polarized at such angles and we have the observed depolarization.

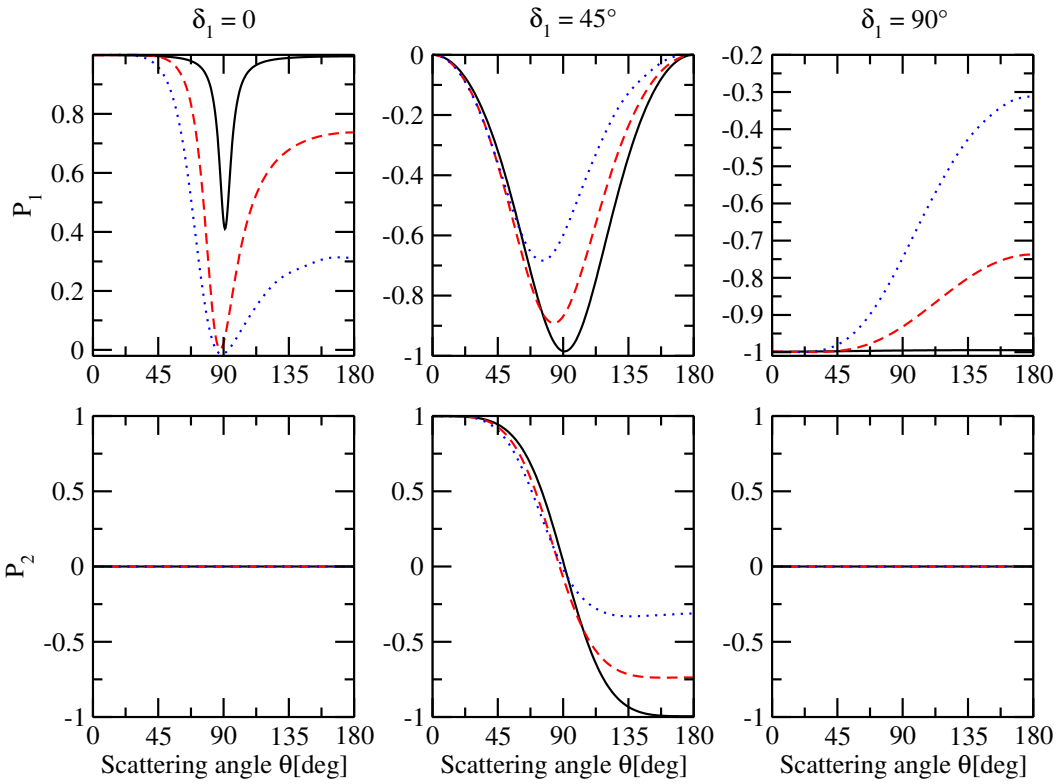

Fig. 6.6: Stokes parameters of scattered photons from the elastic scattering of linear polarized radiation by Xe^{53+}. I present results for photons with an energy $1.1 \cdot E_{ion}$(black solid line), $5 \cdot E_{ion}$(red dashed line), and $10 \cdot E_{ion}$(blue dotted line). Different angles δ_1 between the polarization of the incident radiation and the scattering plane are shown in the columns.

Now that we understand the low energy behavior, it is interesting to examine the Stokes parameters for heavier targets. Analogous to Fig. 6.4 I show in Fig. 6.6 and Fig. 6.7 the P_1 and P_2 parameters for scattering of photons with $1.1 \cdot E_{ion}$, $5 \cdot E_{ion}$ and $10 \cdot E_{ion}$ by Xe^{53+} and U^{91+} for different tilt angles δ_1 between the polarization of the incident radiation and the scattering plane.

A comparison of the new Fig. 6.6 and Fig. 6.7 with Fig. 6.4 shows that the angular shapes of the Stokes parameter for scattering by Ne^{9+} that coincide with the non-relativistic model have the same angular dependence also for heavier targets if the photon energy is relatively small. For higher photon energies, as seen in Fig. 6.6 and especially in Fig. 6.7, the angular shape of all of the Stokes parameters deviate considerably from the dipole approximation. This shows that for such energies the cross-sections become dominated by higher multipole contributions. Interestingly, we can see in Fig. 6.6 and Fig. 6.7 that the P_2 parameter vanishes for all photon energies if the photons are initially polarized within or perpendicular to the scattering plane, c.p. [74]. This symmetry behavior arises from the fact that the projection on final polarization states with $\delta_2 = 45°$ or $\delta_2 = 135°$ get the same contributions from the "xx"-, "xy"-, "yx"-, "yy"-cross-sections we discussed earlier.

In the scattering of high-energy photons by heavy ions the relativistic and higher-multipole effects that lead to a depolarization for coplanar scattering at scattering angles $\theta \approx 90°$ for Ne^{9+} targets become even more prominent. The depolarization dips become wider (low energy photons) and for higher energy photons we also observe that the angular shape

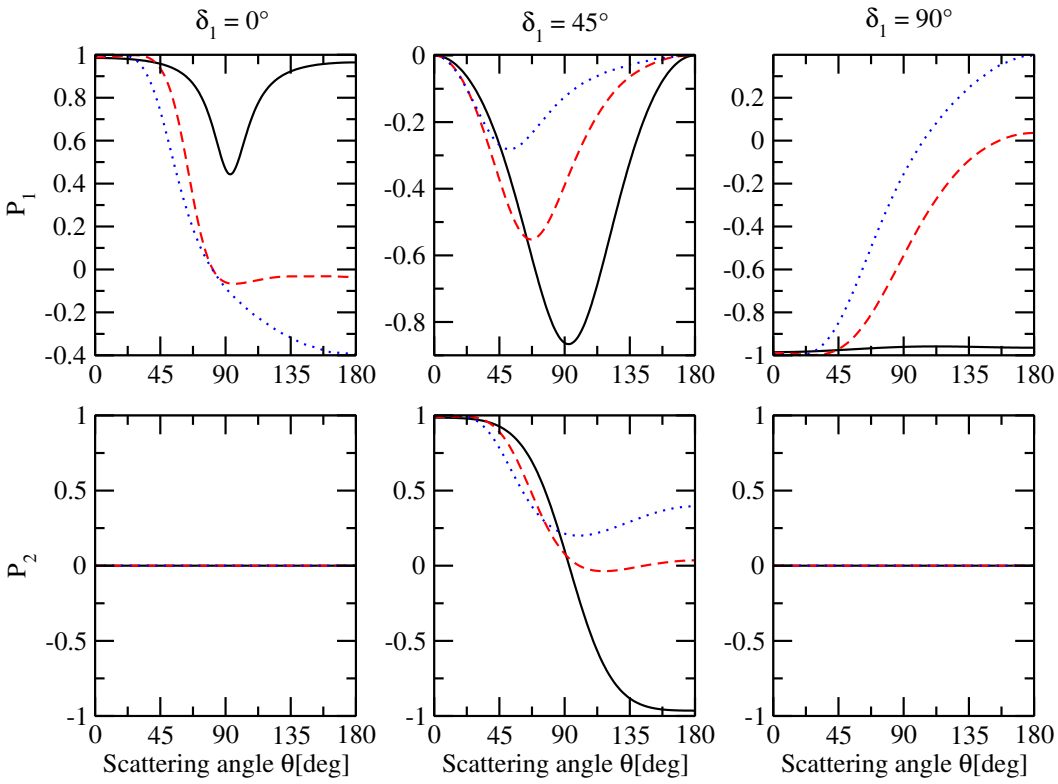

Fig. 6.7: Stokes parameters of scattered photons from the elastic scattering of linear polarized photons by U^{91+}. In this figure the same conventions like in Fig. 6.6 are used.

of P_1 is no longer symmetric with respect to $\theta = 90°$. For the scattering of high energy photons by U^{91+} we can even observe a crossover of the coplanar P_1 parameter at scattering angles $\theta \geq 90°$ as seen in the top left panel of Fig. 6.7. Unfortunately, at these angles the cross-section of the scattering process becomes extremely small (c.p. Fig. 6.3). An experimental measurement of such a crossover might therefore be very challenging.

Stability of the depolarization effect

Up till now I discussed the polarization properties for scattering of completely polarized photons in the case where both the polarization of the incident photons as well as the polarization of the scattered photons could be precisely specified with respect to the scattering plane. At specific polarization and scattering angles we observed an interesting depolarization effect. This depolarization appeared because for these specific scattering angles and polarizations the dominant dipole contribution is strongly suppressed. As a result of the origin of this effect the elastic cross-sections for an observation of photons under these conditions are very low. This leads to the question if this new effect could also be seen in less ideal conditions, e.g. when the initial beam is not perfectly polarized or the incident polarization is slightly tilted with respect to the scattering plane.

To study the stability of the depolarization effect under such non-ideal conditions I first consider the effect of small tilts of the initial polarization. As we have a better understanding

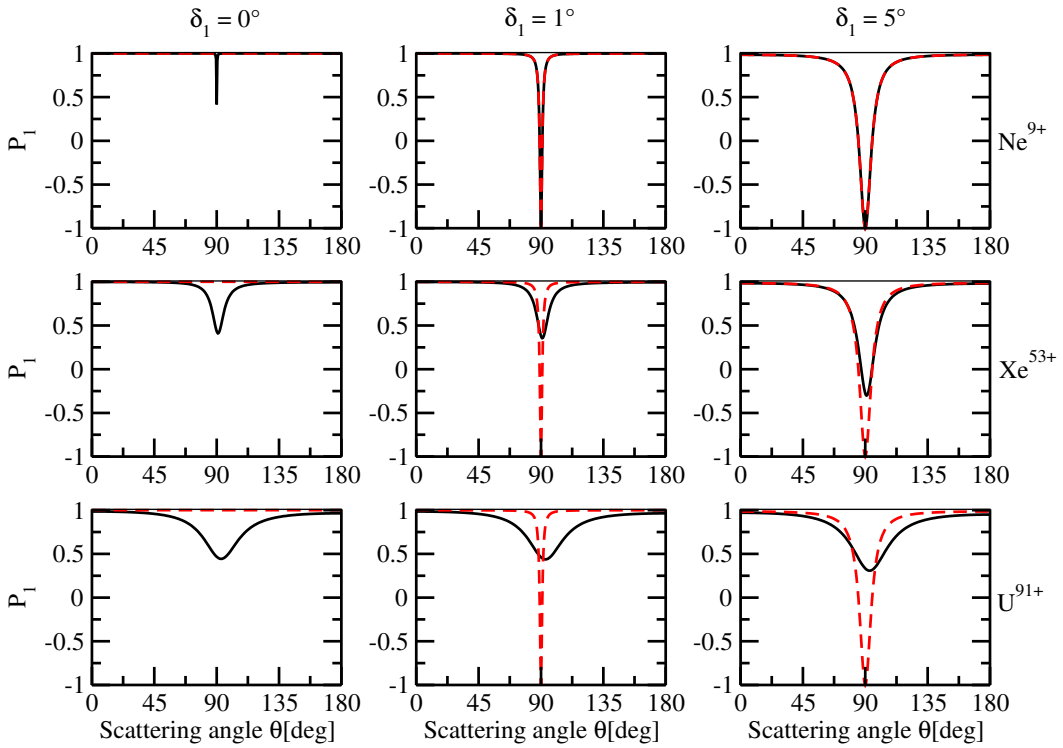

Fig. 6.8: Effects of small tilts δ_1 of the polarization of incident radiation with an energy of $1.1 \cdot E_{ion}$ on the P_1 Stokes parameter of the elastically scattered photons. We consider Ne^{9+}(top row), Xe^{53+}(center row), and U^{91+} targets with no (left column), or small tilts of $\delta_1 = 1\,\mathrm{deg}$ (center column) or $\delta_1 = 5\,\mathrm{deg}$(left column) between the polarization of the incident photons and the scattering plane. Our all multipole results (black solid lines) are compared with the non-relativistic dipole approximation from Eq. (6.9) (red dashed lines).

of the angular behavior of the Stokes parameter for low photon energies I show in Fig. 6.8 the P_1 Stokes parameters of photons with an energy of $1.1 \cdot E_{ion}$ elastically scattered by Ne^{9+}, Xe^{53+}, and U^{91+}. I compare the non-relativistic model (6.9) with the relativistic results for coplanar polarization or small tilts of $\delta_1 = 1°$ and $\delta_1 = 5°$ of the polarization of the incident photons.

We see from Fig. 6.8 that, for a small but non-zero tilt between the incident polarization and the scattering plane, the non-relativistic model predicts a non-relativistic depolarization and even a polarization crossover similar to the spin-flip effect I discussed in the previous section. This non-relativistic depolarization can be easily understood by comparing the "xx"- and the "yy"-cross-section in Fig. 6.5. For a small non-zero tilt of the incident polarization the initial polarization has a small but non-zero projection perpendicular to the scattering plane. Because of this small projection the "yy"-cross-section from Fig. 6.5 has a non-zero contribution to the scattering process. As the "yy"-cross-section has no minimum at $\theta \approx 90°$, at these angles it dominates the scattering process and causes a depolarization dip in the graph. In many cases such a tilt contribution is much larger than the relativistic and higher multipole spin-flip based "xy"-contribution. Therefore, for light scattering targets, unless the polarization angles can be extremely well controlled, the relativistic effects are hidden by the non-relativistic tilt effects, cp. top row of Fig. 6.8.

Fortunately, for heavier targets (center row of Fig. 6.8) the relativistic depolarization is hidden only at larger tilt angles δ_1, c.p. right panel of this row. Thus in the scattering by U^{91+}

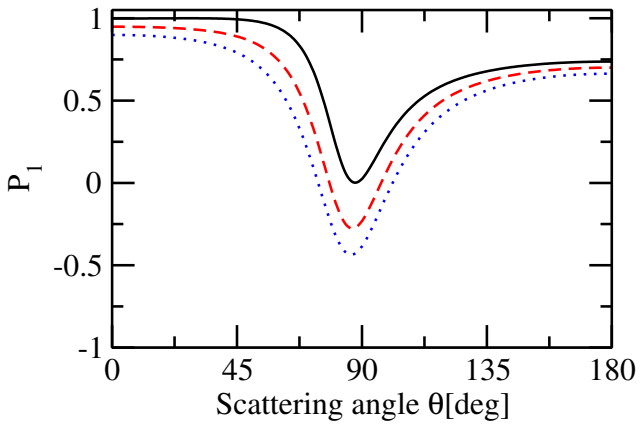

Fig. 6.9: P_1 Stokes parameter of elastically scattering of not fully coplanar polarized incident radiation with a photon energy of $5 \cdot E_{ion}$ for a Xe^{53+} target. I compare radiation fully polarized in the scattering plane (black solid line), with 0.95 (red dashed line) and 0.9 (blue dotted line) polarized light.

(bottom row of Fig. 6.8) the relativistic and higher multipole effects are strong enough to make the relativistic depolarization robust against small tilts of the initial polarization. Even though in such systems a small change of the initial polarization leads to some depolarization of the scattered photons, the relativistic effects remain well visible, c.p. right panel of this row.

I conclude that even small angles between the polarization of the initial photon and the scattering plane have a profound effect on the angular dependence of the linear polarization of the scattered photon. In a possible experimental examination of the polarization properties of elastically scattered photons it is therefore very important to carefully consider how well both the polarization axis of the incident radiation as well as the axis of the scattered photons is known.

Similar effects can also be observed when the incident radiation is not fully polarized. To present the impact of incomplete initial polarization I show in Fig. 6.9 the P_1 Stokes parameter for elastic scattering of an ensemble of photons with different degrees of coplanar polarization and with an energy of $5 \cdot E_{ion}$ by Xe^{53+}. Specifically, I compare the results for photons that are 90%, 95% and 100% polarized. "Not fully polarized" Stokes parameters are evaluated from cross-sections for not fully polarized incident radiation. As mentioned in the theory part these cross-sections for incomplete polarized incident radiation are weighed sums of $\delta_1 = 0°$ and $\delta_1 = 90°$ cross-sections. In order to get the Stokes parameter $P_1 = 0.9$ or $P_1 = 0.95$ for the incident photons, the original δ_1 contribution to the cross-section for incomplete polarized incident photons must be 19, or 39 times greater than the contribution from the $\delta_1 = 90°$ cross-section, c.p. Eq. (6.3).

As we can see from Fig. 6.9, in analogy to the role of small tilts of the polarization of the incident photons, a decrease of the polarization of the incident radiation has a significant effect on the polarization of the scattered photon. Unlike the effects from tilts of the incident polarization, the decrease of polarization of the incident photons lowers the polarization of the scattered photons for all scattering angles.

6.1.4 Conclusion and Outlook

Using a relativistic approach I examined the polarization sensitivity of Rayleigh scattering of photons by ground-state electrons of H-like ions for photon energies above the ionization threshold of the ions. As a first step the elastic cross-section for polarized light was evaluated. For the scattering of photons with a relatively small energy by light ions the angular dependence of such a cross-section can be reasonably described by means of a (classical) non-relativistic dipole approximation. At higher photon energies and for heavier targets we observe a suppression of backscattering due to non-dipole contributions to the scattering process. These cross-sections were used to determine the linear polarization of the scattered photons by means of so-called Stokes parameters under the assumption that the incident photons are linearly polarized.

Like the scattering cross-sections for low photon energies and most angles between the scattering plane and the polarization of the incident and scattered photons these Stokes parameters are well described by the non-relativistic model. At higher photon energies and heavier targets the Stokes parameters can be influenced considerably by higher multipole contributions. However, for all photon energies we observed an exceptional effect in the angular dependence of the P_1 Stokes parameter for coplanar elastic scattering. At a scattering angle of $\theta = 90°$ the scattered photons are depolarized due to spin-flips of the target electrons caused by relativistic and higher multipole effects. Such an effect can only be observed in few-electron ions and has up till now not been described by previous studies. Unfortunately this depolarization effect is only prominent at scattering angles with a small cross-section and requires a very precise control of the scattering parameters. Therefore it might be challenging to observe.

This kind of scattering effect is a nice example how in specifically controlled two-photon processes strong first-order effects can be suppressed to measure small e.g. relativistic or higher multipole contributions. To further explore such possibilities in a system that offers an even greater amount of control over the two-photon process, I studied inelastic Raman scattering by H-like ions.

6.2 Inelastic Raman scattering

6.2.1 Physics background and motivation

When a photon is scattered by a bound electron, energy can be transferred between the photon and the scattering target. This energy transfer can lead to an excitation or de-excitation of the participating target into a different bound state. We call such an inelastic scattering process (Stokes and anti-Stokes) Raman scattering. This kind of process has been extensively studied for solid state and molecular targets in the past and has been applied in measurement techniques such as Raman spectroscopy. For atoms or ions as targets most of the interest on Raman scattering had been up till now focused on scattering by electrons of neutral many-electron atoms. In such systems all of the lower electron states are occupied and it is only possible to excite electrons into high-lying weakly bound states.

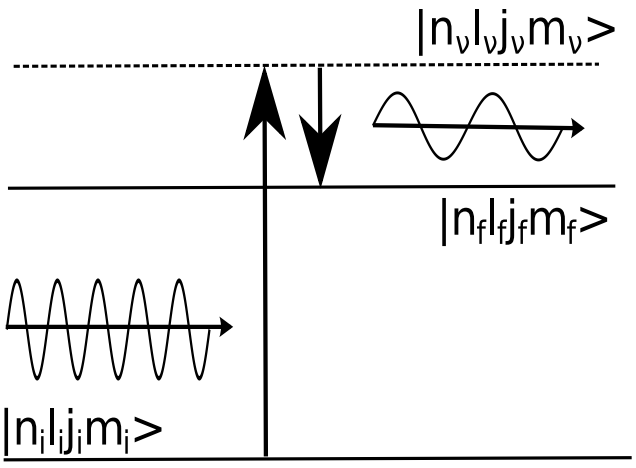

Fig. 6.10: Schematic description of (Stokes) Raman scattering. In the scattering process the initial state $|n_i l_i j_i m_i\rangle$ is excited into the final state $|n_f l_f j_f m_f\rangle$ and the scattering proceeds via a virtual intermediate state $|n_\nu l_\nu j_\nu m_\nu\rangle$. The quantum numbers n, l, j, m were defined in chapter 2.

Inelastic scattering by neutral atoms can therefore only be observed if the incident photons have a sufficient energy, i.e. an energy close to the ionization threshold of the target. At such energies the inelastic scattering process is dominated by resonant scattering via an energetically close real intermediate state. In the last decades this so-called Resonant Raman scattering process has been studied extensively with x-rays scattered by different neutral atoms [27, 28]. However, in such a process only the initial state of a participating electron can be strongly affected by relativistic and strong field effects.

To explore relativistic and strong field phenomena it is therefore interesting to study inelastic Raman scattering of lower energy photons by heavy highly charged few-electron ions. Due to their theoretical simplicity H-like ions are especially interesting targets. In a non-relativistic approximation Raman scattering by light H-like target, e.g. neutral hydrogen, has been studied for many years [14, 22, 23, 24, 25, 26]. These results were e.g. used in the explanation of certain spectral lines in astrophysics [75]. For the inelastic scattering by heavier H-like ions, however, only a preliminary relativistic study [29] exists.
In this part of the chapter I present my more detailed analysis [56] of such systems. I especially focus on so-called Stokes Raman scattering in which the final state is more excited than the initial state, c.p. Fig. 6.10 Using a relativistic approach the inelastic scattering of sub-threshold photons by different H-like ions involving $1s_{1/2} \to 2s_{1/2}$, $1s_{1/2} \to 2p_{1/2}$ and $1s_{1/2} \to 2p_{1/2}$ transition of the ions are studied. Special attention is paid to the energy dependence of the total Raman cross-section and the angular distribution of the scattered photon. Furthermore, for the $1s_{1/2} \to 2p_{3/2}$ process I also consider the occupation of the magnetic substates of the ion after the scattering process.

6.2.2 Raman scattering as a two-photon process

Inelastic Raman scattering can be described in a similar way as elastic scattering and its cross-section is derived in analogy to the derivation of Eq. (6.2). By considering a simultaneous absorption and emission of a photon we have a transition between an initial and a final state via some virtual intermediate state ν. In contrast to the photons in elastic scattering, in the inelastic scattering the energies of the incident (ω_1) and scattered (ω_2) photons are different. Thus a derivation of the differential cross-section for Raman scattering produces a slightly different result. For example, if we assume the incident photons to be unpolarized and do not observe the polarization of the scattered photons, we can describe such a cross-section by averaging over the possible circular incident polarizations and by summing over the (circular) polarizations of the scattered photon:

$$\frac{d\sigma}{d\Omega} = \frac{\alpha_S^2}{2(2j_i+1)} \frac{\omega_2}{\omega_1} \sum_{m_i m_f} \sum_{\lambda_1 \lambda_2} \left| M_{fi}^{sc} \right|^2 , \tag{6.11}$$

with $\lambda_{1,2} = \pm 1$ describing the contributions due to different circular polarization of the incident and scattered photon, j_i is the total angular momentum of the initial state, and M_{fi}^{sc} is the scattering amplitude (4.15). This inelastic cross-section has an additional ω_2/ω_1 prefactor that naturally vanishes in the elastic case (6.2). Here, due to the conservation of energy, the energy of the scattered photon ω_2 can be determined by the energy of the incident photon ω_1 and the energies of the target ion before (E_i) and after (E_f) the scattering process: $\omega_1 + E_i = \omega_2 + E_f$.

For some phenomena of the Raman scattering process the structure of the transition amplitude plays a role. Especially important is the role of different intermediate angular momenta on specific multipole contributions. It is therefore useful to shortly look again at my result from chapter 4 on this topic in the specific situation we have here. Such a structure is best described in a specific coordinate system. In this work, as shown in Fig. 6.11, I assume that the incident photons propagate along the quantization (z-) axis and the scattered photons are observed under a scattering angle θ.

In such a coordinate system the scattering amplitude (4.15) can be written as:

$$\begin{aligned} M_{fi}^{sc} =& 2\pi \sum_{p_1 L_1 p_2 L_2} \sum_{M_2} (-1)^{p_2+1} (-i)^{L_1 - L_2} (i\lambda_1)^{p_1} (-i\lambda_2)^{p_2} \left[L_1, L_2\right]^{1/2} D^{L_2\,*}_{M_2 \lambda_2}(\Omega) \\ & \times \sum_{j_\nu m_\nu} \Big((2j_\nu+1)^{-1} (-1)^{j_f - j_\nu} \left\langle j_f m_f, L_2 M_2 \mid j_\nu m_\nu \right\rangle \\ & \times \left\langle j_i m_i, L_1 \lambda_1 \mid j_\nu m_\nu \right\rangle S_{j_\nu}^{L_2 p_2 L_1 p_1}(\omega_1) \\ & + \left[j_f, j_i\right]^{-1/2} (-1)^{j_\nu - j_i} \left\langle j_\nu m_\nu, L_1 \lambda_1 \mid j_f m_f \right\rangle \\ & \times \left\langle j_\nu m_\nu, L_2 M_2 \mid j_i m_i \right\rangle S_{j_\nu}^{L_1 p_1 L_2 p_2}(-\omega_2) \Big), \end{aligned} \tag{6.12}$$

where we used the usual total angular momenta and projections j, m for the initial (i), virtual intermediate (ν), and final state (f) and the multipole contributions are defined by L_1, p_1 for the absorbed photon and by L_2, p_2 for the emitted one. The M_2 are the projection of the angular momenta transferred by the emitted photon on the quantization axis, and the λ_1, λ_2 the helicities of the photons.

In the equation we see that the Clebsch-Gordan coefficients determine which virtual interme-

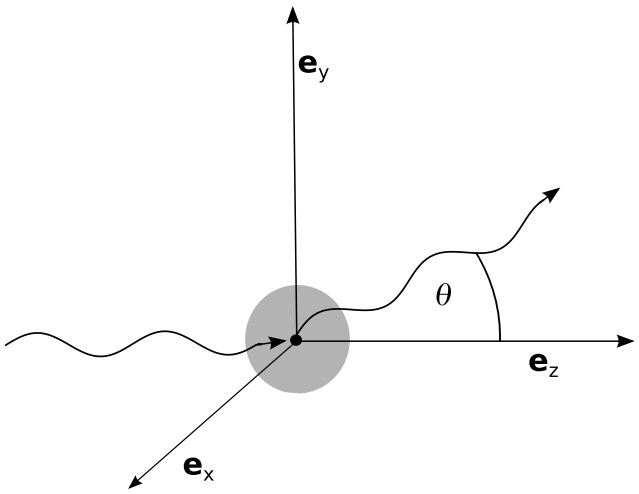

Fig. 6.11: Setup and coordinate system for inelastic Raman scattering of a photon.

diate total angular momenta j_ν and projection on the quantization axis m_μ contribute to the scattering amplitude. Due to the triangle rules of the Clebsch-Gordan coefficients [35] these coefficients are only non-zero when we have $|j_i - L_1| \leq j_\nu \leq j_i + L_1$ and $m_i + \lambda_1 = m_\nu$ or $|j_f - L_1| \leq j_\nu \leq j_f + L_1$ and $m_\nu + \lambda_1 = m_f$.

The differential cross-section (6.11) can be used to determine the absolute inelastic Raman cross-section. By integrating over all angles of the outgoing photon $d\Omega$ we get:

$$\sigma = \frac{\alpha_S^2}{2(2j_i+1)} \frac{\omega_2}{\omega_1} \sum_{m_i m_f} \sum_{\lambda_1 \lambda_2} \int \left| M_{fi}^{sc} \right|^2 d\Omega. \tag{6.13}$$

Alignment of the ions subsequent to the scattering process and its measurement

On top of the differential and total cross-section it is also interesting to examine the occupation of the different magnetic substates of the ions after the inelastic scattering process. As many atomic processes can lead to an unequal occupation of such substates, there exists a common characterization of the occupation in an ensemble of ions. For an ensemble of ions with unequal occupied substates we talk about "polarized" ions, c.p. [35]. Such polarized ions are called "oriented" if the occupation of the magnetic states is not symmetric with respect to the "xy"-plane, i.e. when states with $m_f = m$ are differently occupied than states with $m_f = -m$, and "aligned" when the substates are symmetric but not uniformly filled.

As a first step, my analysis includes an examination of the state of the ions subsequent to an inelastic scattering process in which the direction of the scattered photon is not observed. In such processes, especially for unpolarized incident light, for symmetry reasons the ions are not oriented. It is therefore sufficient to concentrate on the "alignment" of the final state of the system.

Such an alignment of an atomic state is usually described in terms of the so-called alignment parameter A_{20} c.p.[35].

$$A_{20} = \frac{\rho_{20}}{\rho_{00}}, \tag{6.14}$$

where the elements of the statistical tensor

$$\rho_{k0} = \sum_{m,m'} (-1)^{j-m'} \langle jm, j-m' \mid k0 \rangle P(j,m), \tag{6.15}$$

depend on the probability $P(j,m)$ to find an electron in the final state with a total angular momentum j in the substate with magnetic quantum number m. These probabilities are determined for an ensemble of observed ions by the scattering rates or cross-sections of inelastic scattering accompanied by an excitation of the specific magnetic substate.

In this definition, due to the triangle rules of the Clebsch-Gordan coefficient, the alignment parameter vanishes $A_{20} = 0$ if the total angular momentum of the state is $j = 1/2$. Thus for scattering processes with a final angular momentum of $j_f = 1/2$ the alignment is trivial 0. However, subsequent to $1s_{1/2} \rightarrow 2p_{3/2}$ Raman scattering, i.e. for $j_f = 3/2$, the ions can be aligned. In such a system the alignment parameter is given by:

$$A_{20} = \frac{\sigma_{m_f=\pm 3/2} - \sigma_{m_f=\pm 1/2}}{\sigma_{m_f=\pm 3/2} + \sigma_{m_f=\pm 1/2}}, \tag{6.16}$$

where $\sigma_{m_f=m}$ is the Raman cross-section for an excitation of a substate with $m_f = m$:

$$\sigma_{m_f} = \frac{1}{2} \int \frac{\alpha_S^2}{2J_i+1} \frac{\omega_2}{\omega_1} \sum_{\lambda_1,\lambda_2} \sum_{m_i} \left| M_{fi}^{sc} \right|^2 d\Omega. \tag{6.17}$$

It is also possible to derive a general expression, e.g. based on irreducible tensors for the alignment parameter, c.p. [56]: However such an expression is neither useful for a numerical evaluation of this parameter nor helpful in the interpretation of its behavior and will not be presented here.

6.2.3 Results and discussion

Numerical solutions of the differential and total inelastic cross-sections were evaluated by implementing the analytical expression for the reduced two-photon absorption matrix element (4.2.1) I discussed in chapter 4 in the Mathematica computer algebra system. With approximations of these reduced matrix element the scattering amplitudes (6.12) were determined and these building blocks were further used to evaluate the cross-sections (6.11), (6.13), and (6.17). I calculated precise numerical values for the cross-section of Raman scattering by neutral hydrogen, Xe^{53+}, and U^{91+} accompanied by the $1s_{1/2} \rightarrow 2s_{1/2}$, the $1s_{1/2} \rightarrow 2p_{1/2}$, and the $1s_{1/2} \rightarrow 2p_{3/2}$ transitions of the target and for photon energies below the ionization threshold of the target ion. In these calculations it turned out that even for high-Z targets including all multipoles up to L=3 it is sufficient to achieve a good convergence of the result.

Total inelastic scattering cross-sections

The study of total Raman cross-sections, especially their energy dependence, is a good first step to explore the general behavior of such inelastic scattering processes and to estimate the role of relativistic effects in them. I extended previous non-relativistic [14, 22, 23] and relativistic [29] calculations for the $1s \to 2s$ (or $1s_{1/2} \to 2s_{1/2}$) scattering process in neutral hydrogen by not only considering inelastic scattering involving the $1s_{1/2} \to 2s_{1/2}$ transition in different H-like ions, but also the $1s_{1/2} \to 2p_{1/2}$ and $1s_{1/2} \to 2p_{3/2}$ cross-sections. For these processes the cross-sections are shown in Fig. 6.12 as a function of the energy of the incident photon for scattering by neutral hydrogen, Xe^{53+}, and U^{91+}. To be able to compare the energy dependence of the cross-section for the scattering by different ions, it is useful to indicate these incident energies ω_1 in units of the ionization energy of the ground state of these ions E_{1s}. The absolute values of these ground state energies are $|E_{1s}| \approx 13.6eV$ for neutral hydrogen, $|E_{1s}| \approx 41.4keV$ for Xe^{53+}, and $|E_{1s}| \approx 132keV$ for U^{91+}. Furthermore, I include for comparison the non-relativistic results of $1s \to 2s$ scattering by Zon [22] and Sadeghpour [23].

In Fig. 6.12 we observe for all processes a number of resonances in the energy dependence of the cross-sections. These resonances appear at photon energies ω_1 where the energy of the virtual intermediate state $E_\nu = E_i + \omega_1$ in the scattering amplitude (c.p. Eq. (4.12)) corresponds to the energy of a physical eigenstate $|n', j', l', m'\rangle$ of the ion. At such energies inelastic scattering can be understood as a two step process where first the incident photon excites the intermediate state $|n', j', l', m'\rangle$, which then decays to the final state by emitting the "scattered photon", i.e. we have transitions of the form: $1s_{1/2} \to 3p_{1/2} \to 2s_{1/2}$. The resonances can be identified by this real intermediate state and will therefore be called e.g. $3p_{1/2}$ resonances. For light ions the energies of such states are given by Bohr's energy formula (2.20) and resonances are at $\omega_1 = (1 - \frac{1}{n^2})\,|E_{1s}|$. Close to the ionization limit the Raman cross-section is dominated by these resonances and we have the so-called Resonant Raman scattering process. For heavier targets, as we can see in the lower panels of Fig. 6.12, due to the fine structure of the ions, the resonance peaks split into peak multiplets in which each sub-peak corresponds to a different relativistic fine structure level. To illustrate this behavior I mark the energies of the different fine structure levels as vertical blue dotted lines in the figure.

Apart from this resonance behavior, it is also interesting to study the the cross-section for energies where resonances play no major role, i.e. for incident photon energies in the region defined by: $0.8\,|E_{1s}| \leq \omega_1 \leq 0.87\,|E_{1s}|$. In this region it is possible to observe the Z-dependence of Raman scattering involving different transitions of the ion. For example, we see in Fig. 6.12 that for the $1s_{1/2} \to 2s_{1/2}$ process even with high-Z targets the cross-section is in very good agreement with the non-relativistic results for $1s \to 2s$ scattering by neutral hydrogen of Zon [22] (and Sadeghpour [23]). To understand this weak Z-dependence of the cross-section we recall that the transition amplitude for the $1s_{1/2} \to 2s_{1/2}$ scattering process is dominated by the electric dipole(E1E1) , i.e. $L_1 = L_2 = p_1 = p_2 = 1$, multipole contribution. As I showed in chapter 3, the two E1 transition amplitudes in the numerator of the transition amplitude of a two-photon process, c.p. e.g. (4.1), both scale like $Z\alpha_S$ while all energies in the denominator scale in first order like $(Z\alpha_S)^2$, c.p. Eq. (2.20). Thus for equal relative energies in the non-resonant region the Z-dependence of the numerator and denominator cancel each other and the E1E1 scattering amplitude does only weakly depend on the nuclear charge Z (due to additional relativistic effects). As a result for comparable

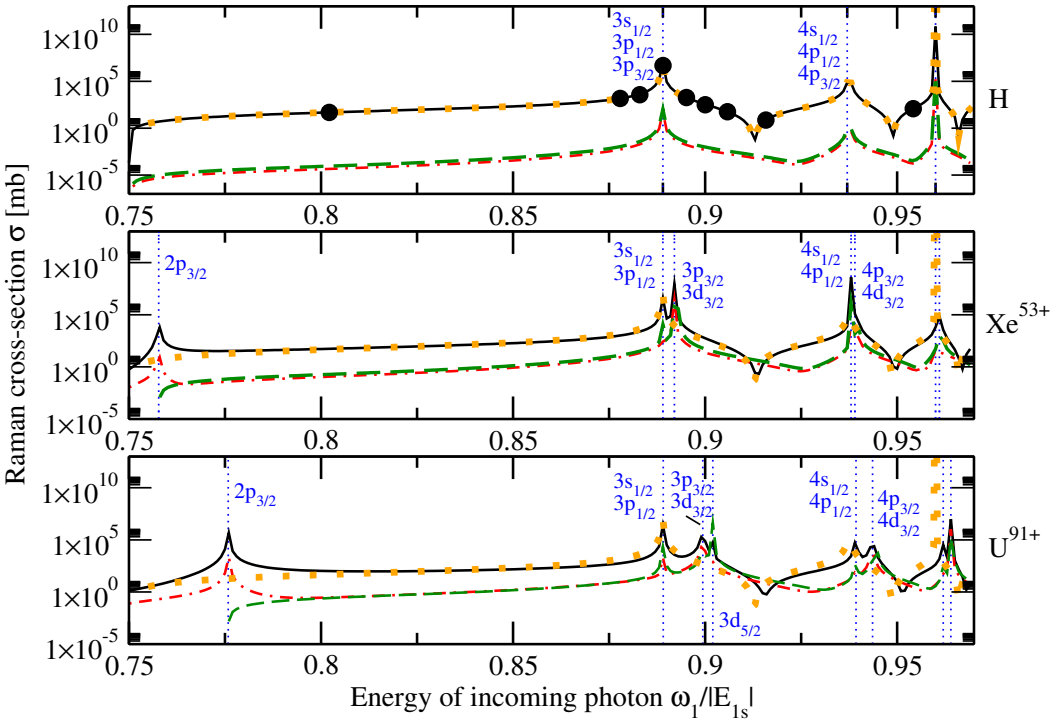

Fig. 6.12: .
Total cross-section for inelastic scattering by neutral hydrogen (top panel), Xe^{53+} (center panel) and U^{91+} (bottom panel) as a function of the energy of the incident photons ω_1. I show Raman scattering involving the $1s_{1/2} \rightarrow 2s_{1/2}$ (black solid line), the $1s_{1/2} \rightarrow 2p_{1/2}$ (red dash-dotted line), and the $1s_{1/2} \rightarrow 2p_{3/2}$(green dashed line) transition of the target. For comparison the non-relativistic results for $1s \rightarrow 2s$ Raman scattering by neutral hydrogen by Zon [22] (orange dotted line) and Sadeghpour [23](black circles) have been included in the graph. The energy of the photons is given in units of the ground state ionization energy E_{1s} of the respective ions. Photon energies that correspond to the excitation energies of specific excited states of the ion have been marked by a vertical blue dotted line.

incident photon energies, i.e. the same ω_2/ω_1 factor in Eq. (6.13), the scattering cross-section (6.13) only has a similar weak Z scaling from higher order multipole contributions and relativistic effects.
In contrast to the $1s_{1/2} \to 2s_{1/2}$ process the cross-sections of $1s_{1/2} \to 2p_{1/2}$ and $1s_{1/2} \to 2p_{3/2}$ Raman scattering become $3-4$ orders of magnitude larger when Z rises from 1 to 92. These $1s \to 2p$ scattering processes have initial and final states with opposite parity. Due to the parity conservation conditions I discussed in chapter 3 and 4, the leading order multipole contributions of the scattering amplitudes are therefore E1M1 and E1E2. These non-electric-dipole leading multipole contributions lead to a $Z\alpha_S$ dependence of the transition amplitude and thus the observed quadratic Z-scaling of the cross-section: $\sigma_{1s_{1/2}\to 2p_{1/2;3/2}} \sim Z^2$.

In a potential future experiment on x-ray scattering by highly charged ions not only inelastic Raman scattering, but also other interaction processes would play a role. To estimate the relative size of the Raman scattering process I compare, for off-resonant photon energies, its inelastic scattering cross-section with the cross-section of the important well-known elastic Rayleigh scattering process. Using the same approach used in the evaluation of the inelastic scattering cross-section, for an incident photon energy of $\omega_1 = 0.8 \cdot E_{1s}$ the elastic cross-section of an elastic $1s_{1/2} \to 1s_{1/2}$ scattering process is evaluated. I found that for scattering by U^{91+} the Rayleigh cross-section is approximately $7200mb$ while the inelastic $1s_{1/2} \to 2s_{1/2}$ cross-section is $105mb$. In other words, in this region the cross-section of the most prominent inelastic process is in the order of 1% of the cross-section for elastic scattering. Thus, to observe Raman scattering a good selection mechanism, like measuring the energy of the scattered photon, is needed. As the detectors in such measurements are usually positioned to measure photons scattered at a specific angle it is very useful to understand the angular-differential cross-section that determines the angular distribution of the scattered photons.

Angular distribution

As we have seen in the elastic scattering process at the beginning of this chapter, the angular shape of differential scattering cross-sections can strongly depend on the energy of the incident photon. To understand such angular shapes, I first define a non-resonant baseline and study the angular distribution of the scattered photons for the different inelastic processes and incident radiation with a photon energy of $\omega_1 = 0.825\,|E_{1s}|$. In Fig. 6.13 the (angle-) differential cross-sections of $1s_{1/2} \to 2s_{1/2}$ (left panels), $1s_{1/2} \to 2p_{1/2}$ (center panels), and $1s_{1/2} \to 2p_{3/2}$ (right panels) Raman scattering by neutral hydrogen (top row), Xe^{53+} (center row), and U^{91+} (bottom row) is shown. To analyze the role of higher multipole effects on these angular shapes I plotted both the results for cross-sections evaluated with all multipole contributions (black solid line) as well as cross-sections evaluated only with the leading order contributions (red dashed line), i.e. for the $1s_{1/2} \to 2s_{1/2}$ scattering I only considered E1E1 scattering and for the $1s_{1/2} \to 2p_{1/2}$ and $1s_{1/2} \to 2p_{3/2}$ processes only scattering contributions from the E1M1 and E1E2 multipoles.
On the left side of Fig. 6.13 we see that the angular distributions for inelastic scattering involving $1s_{1/2} \to 2s_{1/2}$ transitions are, even for scattering by high-Z ions, only minimally affected by non-dipole contributions. For all target ions the angular distribution has typical E1E1 $d\sigma/d\Omega \sim 1 + \cos^2\theta$ shape well known from previous non-relativistic calculations [22]

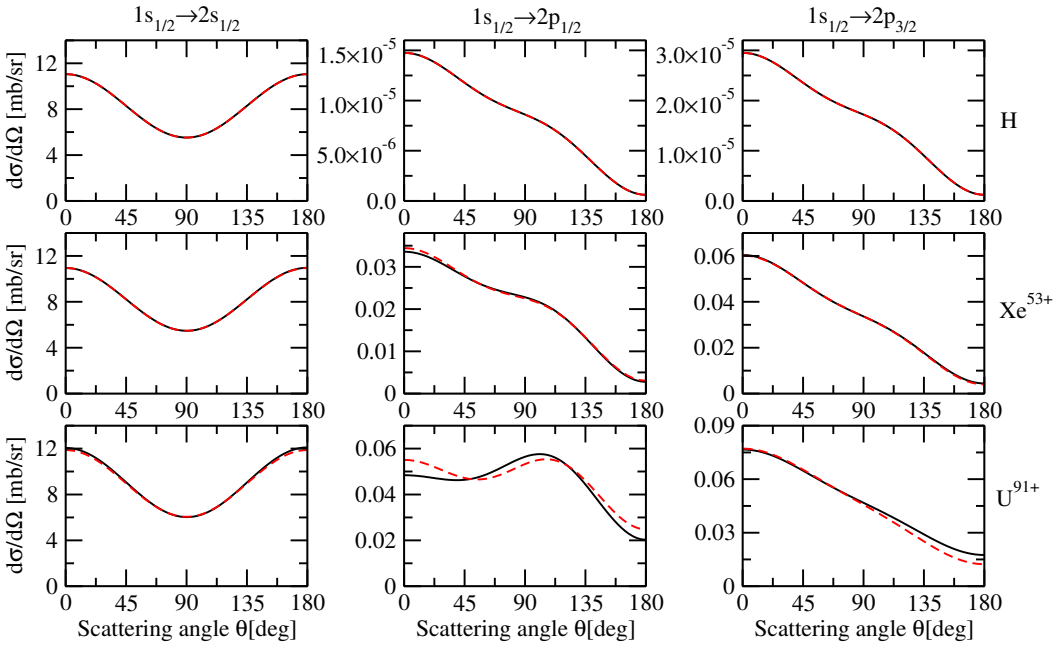

Fig. 6.13: Differential cross-section of $1s_{1/2} \rightarrow 2s_{1/2}$(left panels), $1s_{1/2} \rightarrow 2p_{1/2}$(center panels), and $1s_{1/2} \rightarrow 2p_{3/2}$(right panels) Raman scattering by neural hydrogen (top row), Xe^{53+} (center row), and U^{91+}(bottom row) for an incident photon energy of $0.825\,|E_{1s}|$. I show both calculations including all multipole contributions (black solid line) as well as only the leading multipole contributions (red dashed line) i.e. E1E1 on left panels, E1M1 and E1E2 on the center and right panels.

and other two-photon processes like two-photon decay and elastic scattering.
On the other hand, we see in Fig. 6.13 that in the $1s_{1/2} \rightarrow 2p_{1/2}$ and $1s_{1/2} \rightarrow 2p_{3/2}$ processes the angular shapes of the cross-sections vary for different target ions. For example, for scattering by neutral hydrogen the differential cross-sections of the $1s_{1/2} \rightarrow 2p_{1/2}$ and the $1s_{1/2} \rightarrow 2p_{3/2}$ processes differ only by a constant factor $1/2$ due to the different statistical weight of the final states. In both angular distributions the cross-section is maximal for scattering in forward direction and falls continuously for increasing scattering angles. However, for heavier targets there appears an additional maximum in the differential cross-section of the $1s_{1/2} \rightarrow 2p_{1/2}$ process at around $\theta = 100°$. This new behavior arises partially from a different weight of the leading E1E2 and E1M1 multipole contributions and partially from higher multipole contributions. It is contrasted by the $1s_{1/2} \rightarrow 2p_{3/2}$ angular distributions that remain relatively unchanged even for high-Z target ions. In this scattering process even for scattering by U^{91+} higher multipole contributions play only a minor role.

Based on this investigation of the angular behavior of the differential cross-section for non-resonant photon energies, I now examine how these angular shapes change near the resonances. In my research I observed that near such resonances these shapes can change drastically for slightly different incident photon energies. As a good example, I show in in Fig. 6.14 the angular distribution of photons inelastically scattered by U^{91+} involving a $1s_{1/2} \rightarrow 2s_{1/2}$ transition of the ion for incident photon energies near the $3p_{1/2}$ resonance.
Fig. 6.14 shows an angular distribution with a minimum at $\theta = 90°$ for incident photon energies below the resonance, i.e at $\omega_1 = 0.888\,|E_{1s}|$. For photon energies slightly above

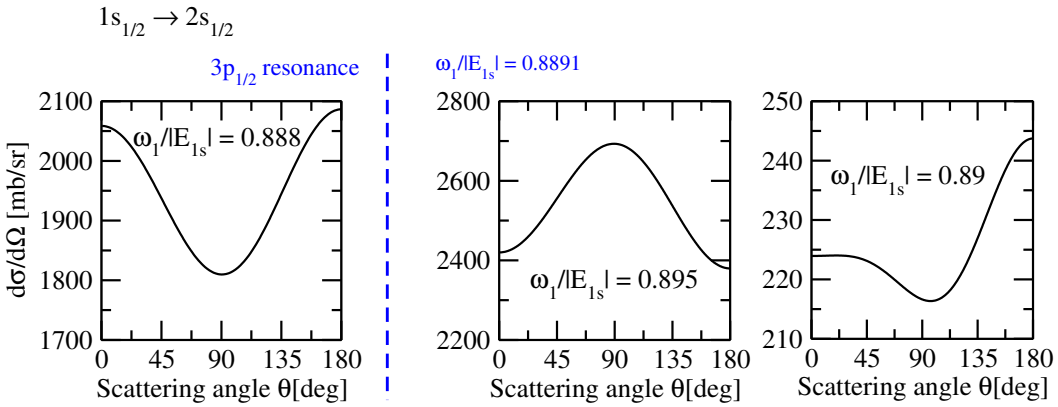

Fig. 6.14: Angle-differential cross-section for Raman scattering by U^{91+} involving the $1s_{1/2} \to 2s_{1/2}$ transition of the ion at photon energies near the resonance corresponding to an excitation of the $3p_{1/2}$ state.

the resonance at $\omega_1 = 0.89\,|E_{1s}|$ the angular shape of the cross-section changes drastically and has a maximum at this angle. At even higher photon energies the "usual" minimum reappears. This profound energy dependence of the angular shape is caused by the behavior of the leading order E1E1 contributions to the scattering process. To understand its origin we need to consider the behavior of the scattering amplitudes (6.12) in detail. The energy dependence of these amplitudes is determined by the reduced two-photon absorption matrix elements in them. Near resonances such reduced matrix elements behave very differently depending on their specific intermediate angular momentum. For example, near the $3p_{1/2}$ resonance the part with $j_\nu = 1/2$ is dominated by the real $3p_{1/2}$ intermediate state and can be approximated by:

$$S^{L_1=p_1=L_2=p_2=1}_{j_\nu=1/2}(\omega_1) \approx \frac{\left\langle 2p_{1/2} \left|\left| \boldsymbol{\alpha} \mathbf{a}^{(p_2)}_{L_2} \right|\right| 3p_{1/2} \right\rangle \left\langle 3p_{1/2} \left|\left| \boldsymbol{\alpha} \mathbf{a}^{(p_1)}_{L_1} \right|\right| 1s_{1/2} \right\rangle}{E_{1s_{1/2}} + \omega_1 - E_{3p_{1/2}}}, \tag{6.18}$$

This reduced matrix element changes its sign at the resonance. On the other hand, as the $3p_{3/2}$ state has a different energy level the $S^{L_1=p_1=L_2=p_2=1}_{j_\nu=3/2}$ element changes only marginally at this energy. Due to interference between the contributions from these two elements, the angular dependence of the differential cross-section behaves near the resonance like:

$$\frac{d\sigma}{d\Omega} \sim C + S_{j_\nu=1/2} \cos^2\theta, \tag{6.19}$$

where C is some arbitrary constant.

The shape change can thus be traced back to this interference. It is important to stress that this behavior only appears when either the $S_{j_\nu=1/2}$ or the $S_{j_\nu=3/2}$ reduced matrix element changes its sign, i.e. it is only visible in relativistic systems in which there is a sizable fine structure splitting between the $3p_{1/2}$ and $3p_{3/2}$ levels. For that reason the shape changes can neither be observed for scattering of photons by light ions nor in scattering processes to higher states, e.g. in $1s_{1/2} \to 5s_{1/2}$ Resonant Raman scattering.

This shape flip effect does not only appear in the $1s_{1/2} \to 2s_{1/2}$ process. As seen in Fig. 6.15, it can e.g. also be observed near the $3s_{1/2}, 3p_{1/2}$ resonance of the $1s_{1/2} \to 2p_{1/2}$ inelastic scattering process.

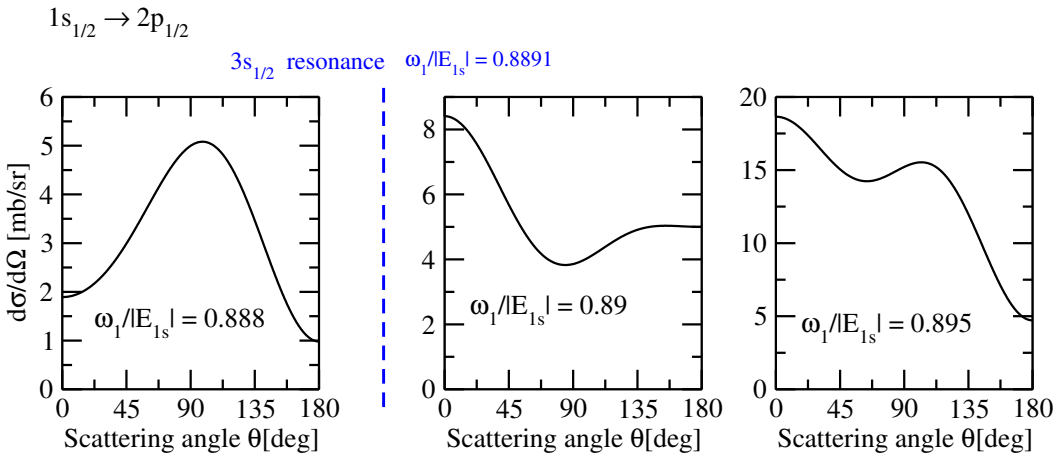

Fig. 6.15: Angle-differential cross-section for Raman scattering by U^{91+} involving the $1s_{1/2} \rightarrow 2p_{1/2}$ transition of the ion at photon energies near the resonance corresponding to an excitation of the $3s_{1/2}$ state

In principle, such an influence of the energy of the incident photons on the angular distribution of the scattered photons should be experimentally accessible in the near future. Brilliant x-ray sources with a sufficiently small spectral width of e.g. 100eV for 100keV photons exist e.g. in the Petra III facility. Modern semiconductor detectors that could be used to measure the scattered photons are also available. To my knowledge it is at the moment unfortunately not possible to use such x-rays in combination with sources of highly charges ions that can produce a sufficiently dense U^{91+} target. If these problems could be overcome, measuring the flip of the angular shape might be an interesting way to probe the structure of the ions in detail.

Alignment of the ions subsequent to the scattering process

In the $1s_{1/2} \rightarrow 2p_{3/2}$ inelastic scattering process it is possible to consider not only the differential and total scattering cross-section but we can also study how the different magnetic substates of the ions are occupied subsequent to the scattering process. To gain some first knowledge on this occupation distribution I studied the alignment of the final state of the system under the assumption that the scattered photons are not observed. Using Eq. (6.16) and the cross-sections (6.17) the alignment parameter A_{20} for $1s_{1/2} \rightarrow 2p_{3/2}$ Raman scattering by neutral hydrogen, Xe^{53+}, and U^{91+} was evaluated. I only consider these parameters for incident photon energies up to $\omega_1 \leq 0.9\,|E_{1s}|$ to be able to ignore the influence of competing atomic processes (that can excite the $2p_{3/2}$ state) on the alignment parameter. Such a process could e.g. be a two-step excitation consisting of an inelastic $1s_{1/2} \rightarrow 3s_{1/2}$ scattering process and a subsequent spontaneous $3s_{1/2} \rightarrow 2p_{3/2}$ decay.
For such incident photon energies I show in Fig. 6.16 the alignment parameter A_{20} of the final state for $1s_{1/2} \rightarrow 2p_{3/2}$ scattering by different target ions. To better understand the origin of the alignment I include both calculations incorporating all multipole contributions (black solid line) as well as leading order (E1M1+E1E2) results (red dashed lines). Fig. 6.16 shows moderate alignment of the final state in the range of $-0.4 \leq A_{20} \leq 0$ for all target ions. In the graphs we can see that the energy dependence of A_{20} can be understood as a

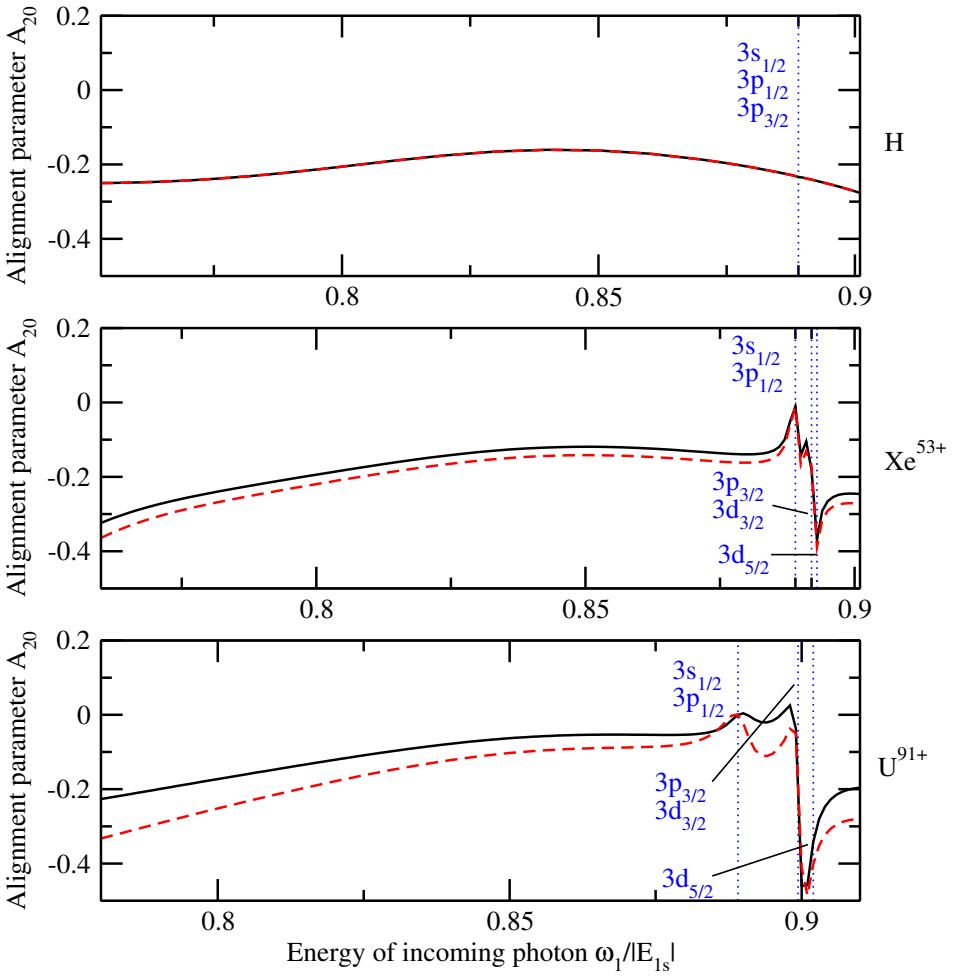

Fig. 6.16: Alignment parameter of the final state of the ions for inelastic scattering by neutral hydrogen (top panel), Xe^{53+}, and U^{91+} involving the $1s_{1/2} \rightarrow 2p_{3/2}$ transition as a function of the incident photon energy ω_1. The photon energy is given in units of the ground state ionization energy E_{1s} of the ion.I compare calculations involving all multipole orders (black solid line) with leading order(E1M1+E1E2) calculations (red dashed line).

weak non-resonant variation (top panel) on top of which, for scattering by Xe^{53+} or U^{91+}, some resonance peaks and dips appear. Both the smooth and the resonant behavior mainly arise from the leading order (E1M1+E1E2) contribution as we can see from Fig. 6.16 by comparing the leading-order with the all multipole results.

Some hints on the origin of this non-zero alignment can be obtained by studying its behavior at the resonances in more detail. The resonant alignment peaks or dips appear at the same photon energies as the resonance peaks of the total decay rate. For high-Z targets these energies therefore correspond to specific fine structure levels. By coupling of the angular momenta of the incident and scattered photons as well as the initial, resonance-dominated virtual intermediate, and final state of the ions it is possible to understand the alignment at these resonances.
The alignment of the ion after the scattering process originates from the different scattering cross-sections into the specific magnetic substates. As evaluation of these cross-sections (6.17) involves an integration over all possible directions of the scattered photon, this scattered photon can not be the source of any direction dependence of the system. Any non-zero alignment must therefore be related to the incident photon whose propagation direction defines the quantization axis.
At the $3s_{1/2}, 3p_{1/2}$ and the $3p_{3/2}, 3d_{3/2}$ resonances the contributions of the virtual intermediate states are dominated by the reduced matrix elements with $j_\nu = 1/2$ or $j_\nu = 3/2$. Following the triangle rules for the angular momentum coupling in Eq. (6.12), it is evident that for an initial magnetic quantum number $m_i = \pm 1/2$ and a projection of the angular momentum of the photon given by its helicity $\lambda_1 = \pm 1$ all intermediate magnetic substates can be evenly occupied. Such virtual intermediate states would therefore have no preferred direction and the alignment of the ions at these resonances vanishes.
On the other hand, at the $3p_{5/2}$ resonance the dominant intermediate angular momentum is $j_\nu = 5/2$. Transitions via such an intermediate state proceed by absorbing an electric quadrupole(E2) photon with $L_1 = 2$ and emitting a magnetic dipole photon. Since along the propagation direction of the photon the projection of the angular momentum is limited by its helicity ($\lambda_1 = \pm 1$), angular momentum coupling does not allow an occupation of the $m_\nu = \pm 5/2$ intermediate substates. The intermediate state is therefore aligned. This alignment can be seen in the alignment parameter of the final state which has a maximum in its absolute values at such energies.

There are a number of methods to measure the alignment parameter I discussed in this section. For example, it is possible to measure the angular distribution of the decay photons of the excited $2p_{3/2}$ state. In dipole approximation the angle-differential decay rate for a $2p_{3/2} \to 1s_{1/2}$ single photon decay of aligned ions has been determined e.g. in Eq. 3.36 in Balashov's book [35] and is:

$$\frac{dW}{d\Omega} = \frac{W_0}{4\pi}\left(1 + \frac{A_{20}}{4}(3\cos^2\theta_E - 1)\right), \tag{6.20}$$

with Ω the propagation direction of the emitted photon in the same coordinate system we used before and W_0 the total decay rate of the process. The emission angle θ_E is defined in the same way as the scattering angle θ.

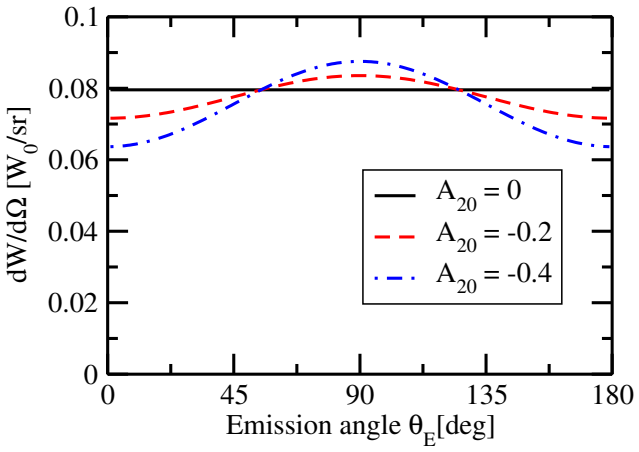

Fig. 6.17: Angular distribution of $2p_{1/2} \rightarrow 1s_{1/2}$ single photon decay for different alignment parameters A_{20} of the initial state. The decay rate is given in units of the total decay rate of the process W_0.

To illustrate this expression in Fig. 6.17 I show how such an angular distribution would be affected by different alignment parameters. An alignment parameter of $A_{20} = 0$ can be found e.g. for photon energies at the $3s_{1/2}, 3p_{1/2}$ and the $3p_{3/2}, 3d_{3/2}$ resonances, c.p. e.g. bottom panel in Fig. 6.16. For such $1s_{1/2} \rightarrow 2p_{3/2}$ Raman scattering by U^{91+} a moderate alignment of $A_{20} = 0.2$ will be found if the incident photons have a relatively low energy of $\omega_1 \approx 0.8E_{1s}$. The maximum alignment of $A_{20} = -0.4$ can be found at the $3d_{5/2}$ resonance, c.p. Fig. 6.16. We see from Fig. 6.17 that these different alignment parameters can be easily distinguished by measuring the angular distribution of the subsequent emitted decay photon. However, a practical realization would run into similar problems as the observation of the angular flip at the resonances: good enough x-ray sources and detectors exist, but it is difficult to procure a suitable target of highly charged ions. As studying the alignment of the ions subsequent to an inelastic scattering process seems to be a promising tool to study the interplay of different transition paths via specific intermediate states, it is to be hoped that these problems will be overcome in the future.

6.2.4 Conclusion

I discussed inelastic Raman scattering by H-like ions involving the $1s_{1/2} \rightarrow 2s_{1/2}$, $1s_{1/2} \rightarrow 2p_{1/2}$, and $1s_{1/2} \rightarrow 2p_{3/2}$ transition of the ion. It was found that the cross-section for $1s_{1/2} \rightarrow 2s_{1/2}$ inelastic scattering depends only weakly on the nuclear charge. However, while for low-Z systems the cross-section of the $1s_{1/2} \rightarrow 2p_{1/2}$ and $1s_{1/2} \rightarrow 2p_{3/2}$ scattering processes can be neglected in comparison to the cross-section of the $1s_{1/2} \rightarrow 2s_{1/2}$ process, due to favorable Z-scaling for heavier targets these $1s_{1/2} \rightarrow 2p_{1/2}$ and $1s_{1/2} \rightarrow 2p_{3/2}$ processes become increasingly important.

For all scattering processes the Raman cross-section has an interesting dependency on the energy of the incident photons with a number of distinct resonance peaks. At these resonances the scattering process proceeds as a two-step process via a real intermediate state that gets excited and decays into the final state. The position of these resonances thus reflects the energy levels of the target ions. The resonances exhibit for high-Z targets a fine

structure splitting into several sub-resonances.
This fine structure splitting of the resonance peaks has an influence on other scattering properties, such as the angular distribution of the scattered photons. Due to an interference of the contributions to the transition amplitude that proceed via intermediate states with different total angular momenta, e.g. near the $3p_{1/2}$ resonance a flip of the angular shape of the $1s_{1/2} \rightarrow 2p_{1/2}$ cross-section is observed.
Apart from these cross-sections, the alignment of the ions subsequent to inelastic scattering of photons involving $1s_{1/2} \rightarrow 2p_{3/2}$ transitions was studied. In this scattering process a moderate alignment was found. While in light ions such an alignment depends smoothly on the energy of the incident photon for high-Z targets, a number of resonance peaks and dips appear. The peaks and dips allow us to gain some insight into the role of different transition paths via virtual intermediate states with specific intermediate angular momenta.
It is therefore worthwhile to explore possibilities for an experimental measurement of such an alignment, e.g. by means of measuring the angular distribution of the photons of the subsequent single photon decay of the $2p_{3/2}$ state.

7 Review and Outlook

In this thesis a relativistic framework was used to study different two-photon processes in heavy H-like and He-like ions. The text began with an introduction of the theoretical basis of these studies. After giving a brief motivation of the topic in chapter 1, I repeated the theoretical basis for a relativistic description of H-like and heavy He-like ions in chapter 2 and introduced some basic concepts needed to discuss the two-photon processes. Following this introduction it was shown in chapter 3 how such few-electron ions interact with electromagnetic fields. Most important, I demonstrated how a perturbative approach to electron-photon interaction can be used to theoretically model the different two-photon processes by means of so-called transition and scattering amplitudes. Then, the effects of static external electric fields on ions was briefly analyzed. Finally, in chapter 4, I introduced a common framework to evaluate the relativistic amplitudes for the different two-photon processes. This framework was used in combination with the results from chapter 3 to model the processes.

Subsequently to this theoretical basis I applied this common framework to study a number of specific two-photon processes in detail. A central theme in these studies was the questions how and to what extent two-photon processes can be externally influenced and what kind of effects appear in such systems. To explore this theme I studied in chapter 5 the effect of external electromagnetic fields on the two-photon decay of excited H-like and He-like ions. By extending a previous study on the effects of static electric fields from my diploma thesis, it was found that such perturbations often lead to a fast de-excitation of the initial state by means of single photon decay and two-photon processes become negligible. Through this observation critical field strengths that correspond to critical laser intensities could be defined, at which the side effects of the external influence on a two-photon process dominate the physical system and make observations of any two-photon transition impossible. These results proved that some previously proposed measurement methods to examine parity non-conservation effects are not feasible. Apart from defining such limits, static perturbations of two-photon decay allow us to gain some general knowledge on perturbed two-photon transitions. For example, I observed that interference between the original and the perturbative contribution of the scattering process can only be observed in some specific transition processes. Even in these processes it only plays a role for observables that depend on the angle between the emission direction of both photons. Furthermore, also independent of such interference effects, the influence of external perturbation can depend strongly on the direction of the perturbation due to effects related to a virtual "alignment" of the ion.

While keeping these static limits in mind, I studied a specific two-photon transition in which external fields are used to fix the direction and polarization of one of the emitted photons, the so-called singly stimulated two-photon decay. While previous studies considered this exotic process only in light ions or atoms, it is shown that it should, at least theoretically, be observable in highly charge heavy ions and allow to exert some control over a two-

photon decay process. However, more practical considerations show that the need to have a reservoir of excited highly charged heavy ions would make an experimental realization very difficult.

To somewhat circumvent these issues I also considered, in chapter 6, the mathematically similar elastic and inelastic photon scattering processes which are experimentally easier to access. These studies consisted on the one hand of an analysis of the polarization properties of photons elastically scattered by heavy H-like ions. For such one-electron ions I showed that under special conditions the dominant dipole effects can be suppressed and weak relativistic and higher multipole contributions dominate the polarization of the scattered photons. For heavy ions these effects are robust enough to be measured experimentally.
On the other hand, apart from such elastic scattering processes, I also examined inelastic Raman scattering by H-like ions involving the $1s_{1/2} \to 2s_{1/2}$, the $1s_{1/2} \to 2p_{1/2}$, and the $1s_{1/2} \to 2p_{3/2}$ transitions in the target ions. This analysis revealed clear resonances in the energy dependence of the inelastic scattering cross-section. The resonant energies correspond to excitation energies of the ions. For heavy ions due to the fine structure of these systems, the resonance peaks are split into several sub-peaks. This splitting not only has an effect on the total cross-section, but also strongly influences the angular distribution of the inelastically scattered photons. Most importantly, due to interference of contributions to the scattering amplitude that are linked to states of the ions with different virtual intermediate angular momenta, the angular shape of e.g. the $1s_{1/2} \to 2s_{1/2}$ process changes drastically for incident photon energies near the $3p_{1/2}$ excitation energy. Additionally to such photon related scattering properties in inelastic Raman scattering processes, the state of the ions after the scattering process can be examined. For example, subsequent to a $1s_{1/2} \to 2p_{3/2}$ Raman scattering process in which the scattered photon is not observed, the participating ion has non-zero alignment. This alignment depends on the energy of the incident photon. For heavy target ions there are resonant incident energies at which we have either sharp minima or maxima of the alignment. Through a detailed study of this alignment it might be possible to gain new insights on angular momentum related phenomena in highly charged ions.

In conclusion, a relativistic framework for describing different two-photon processes was introduced. Using this framework, a number of specific systems were studied. I found that, while external electromagnetic fields allow to control two-photon transition to some extent, side effects caused by the fields an the often difficult preparation of such systems somewhat limit possible experimental schemes employing such fields. As an alternative it is possible to study elastic as well as inelastic photon scattering processes that offer a similar level of control, but are more easily experimentally accessible. In such photon scattering processes a number of interesting effects can be observed. In the future a careful analysis of such effects might lead to new methods to analyze the internal structure of highly charged heavy ions.

In my research I found that the photon scattering, especially inelastic Raman scattering by few electron ions, are the most promising processes to further explore the two-photon processes. As future steps it would thus be interesting to further examine the properties of inelastic scattering in greater detail. The first topic of such studies would be a deeper analysis of the alignment and orientation of the ion after the scattering process. For example, by measuring the scattering angle θ_1 of a scattered photon in coincidence with the emission

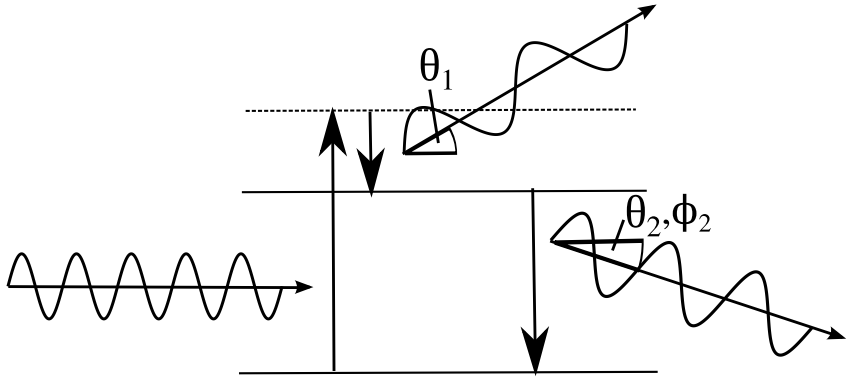

Fig. 7.1: Schematic description of the measurement of an inelastically scattered photon (scattered by θ_1) in coincidence with the subsequent single photon decay of the excited state (with emission angles θ_2, ϕ_2).

angle e.g. θ_2, ϕ_2 of the photon emitted in the subsequent single photon decay, c.p. Fig. 7.1, it should be possible not only to study non-zero alignment of the ion subsequent to the scattering process, but also a possible on-zero orientation of the final state. Similar to the alignment of the final state in such an experiment the behavior of the orientation of the ion after the Raman process should be especially interesting for near-resonant incident photon energies. By means of such an examination, presently open questions on the origin of the alignment (or new ones on the origin of a possible orientation of the ion) can be probed. Most likely specific experimental configurations would be revealed that are very sensitive to small effects, e.g. from relativistic or higher multipole contributions.
Apart from such research on the state of the ion after the scattering process, the properties of the scattered photons from inelastic Raman scattering should be further examined. For example, with little effort the polarization sensitivity of the Raman cross-section could be analyzed in a similarly way as the study of the polarization transfer in elastic Rayleigh scattering in chapter 6.1. Like in the elastic process, in the inelastic scattering of photons with non-resonant photon energies, there should be some specific polarizations and scattering angles under which the strong first order contributions are suppressed and weaker effects, e.g. from higher multipoles or relativistic physics, can be observed. Additional to effects already observed in the elastic scattering process for near-resonant incident photon energies, the polarization of the scattered photon might also be influenced in an interesting way by interferences between the resonant and non-resonant parts similar to the shape changes I observed in the angular distribution of the scattered photons.

For all these inelastic scattering properties, the ones we studied in Chapter 6 as well as the ones that are mentioned in the previous paragraphs, at specific incident photon energies the behavior is dominated by the resonances that I discussed in chapter 6.2. Furthermore, due to its mathematical similarity such resonances might also play a role in elastic Rayleigh scattering of low energy photons by few electron ions. With the theoretical approach that was used in this thesis only a very preliminary study of the influence of these resonances is possible. Therefore, to examine the scattering processes in this region more rigorously, more advanced methods would have to be developed. Such methods must allow to include the precise values of the energy of the resonant intermediate state and, most importantly, its line width. One approach to take these energies and line widths into account is e.g. to

separate the state of the ion that is responsible for the resonance $|\nu_r\rangle$ from the other states in the sum over all states, e.g. in Eq. (4.3):

$$\sum_{\nu} \frac{|\nu\rangle\langle\nu|}{E-E_\nu} = \sum_{\nu\neq\nu_r} \frac{|\nu\rangle\langle\nu|}{E-E_\nu} + \frac{|\nu_r\rangle\langle\nu_r|}{E-E_{\nu_r}-\Delta E+i\Gamma}, \tag{7.1}$$

where the sum on the right side runs over all states ν with the exception of the resonant state $|\nu_r\rangle$ and I included small energy corrections ΔE, e.g. from the Lamb shift and the line width Γ, in the resonant state.
In the Greens function approach I used to evaluate the reduced matrix elements for two-photon absorption such a separation of the sum can be performed analytically. The first term of Eq. (7.1) can be expressed by means of so-called dressed Greens functions that can be evaluated by, c.p. [12, 61]:

$$\widetilde{G}(\mathbf{r},\mathbf{r}';E) = \lim_{E_{\nu_r}\to E}(E-E_{\nu_r})G(\mathbf{r},\mathbf{r}';E). \tag{7.2}$$

With such a dressed Greens function the reduced matrix elements for Raman scattering without the influence of the resonant state could be evaluated using the approach from chapter 4. The resonant part would be evaluated as a simple two step process via the intermediate state $|\nu_r\rangle$. Finally, the non-resonant and the resonant parts would be summed to a total scattering amplitude that would allow to describe the scattering process for near resonant photon energies.
However, as this kind calculation is very complex and prone to error, it might be more economic to use existing numerical methods based on a finite basis, like the ones I mentioned in chapter 4, to include precise energies and line widths of specific states. In such an approach the line widths and precise energies can easily be added to any number of specific summands of the finite sum and used to evaluate the reduced matrix elements near a resonance.

By developing such methods for a precise analysis of the near-resonance behavior in inelastic (and elastic) scattering by few electron ions, it would also be possible to examine the effects of perturbations, e.g. from external electric fields or even the parity violating weak force, on such inelastic (as well as elastic) scattering processes. Such an analysis would not only describe the effects of the perturbation for off-resonant photon energies, but also for photon energies close to the resonances. An examination of the effects of these perturbations on the inelastic photon scattering process could lead to experimental applications of Raman scattering in advanced studies, e.g. in the analysis of parity non-conservation effects in the low-energy regime.

Acknowledgment

Writing a PhD thesis is a large project which is only possible with a lot of support from many people. I would like to acknowledge the help I have received from these persons.
First and foremost I would like to thank my PhD supervisor Priv.Doz. Dr. Andrey Surzhykov, without whose excellent support and motivation this work would not have been possible. Also I would like to thank Prof. Dr. Stephan Fritzsche, the head of my current group, for his constant useful advice and Dr. Kai Schweda, my second supervisor, for his very important moral support during my PhD studies. Furthermore, I would like to thank Priv.Doz. Dr. Zoltán Harman who agreed to become the second reviewer of my thesis.

The study on elastic scattering originated from a collaboration with several colleagues. Apart from my supervisor and the head of my group I would like give special thanks to Dr. Pedro Amaro and Dr. Vladimir Yerokhin for the fruitful cooperation and interesting discussions. For enabling a nice working environment with many interesting discussions my thanks also go to my current and former colleagues Dr. Sean McConnel, Dr. Fillippo Frattini, Dr. Oliver Matula, Zhongwen Wu, Dr. Armen Hayrapeyan, Dr. Anton Artemyev, Rober Müller, Dr. Daniel Seipt, Dr. Lalita Sharma, Dr. Günter Weber, Dr. Renate Märtin, Dr. Valery Serbo, Oleksiy Kovtun, Johan Holmberg, Holger Jörg, Manuel Mai, Shintan Shah, Dr. Stanislav Tashenov, Walter Hahn, Stefan Kraft, Jonas Gunst, Vladimir Zaytsev, Sebastian Stock, Erik Abraham, Marie Scholz-Marggraf, Stefan Tietze, Wilko Middens, and Tobias Bucher.

My thanks also go to the "Heidelberg Graduate School for Fundamental Physics" and the "Helmholtz Graduate School for Hadron and Ion Research" for excellent education opportunities.

Last and most important I want like to thank my family. Without the moral support of my father Dr. Ingo Jahrsetz, my sisters Dr. Judith Jahrsetz and Stefanie Palabiyik, and especially of my mother Renate Himmelmann who also was a great help with the proof reading of this text, finishing this thesis would not have been possible.

List of Tables

List of Figures

Bibliography

[1]A. Surzhykov, S. Fritzsche, and Th. Stölker. In: *J. Phys. B: At. Mol. Opt. Phys.* 35 (2002), p. 3713.

[2]A. Gumberidze, Th. Stöhlker, and D. Banas et al. In: *Hyperfine Int.* 199 (2011), pp. 50–69.

[3]A. Schäfer, G. Soff, P. Indelicato, B. Müller, and W. Greiner. In: *Phys. Rev. A* 40 (1989), pp. 7362–7365.

[4]A. Surzhykov, P. Koval, and S. Fritzsche. In: *Phys. Rev. A* 71 (2005), p. 022509.

[5]C. Szymanowski, V. Veniard, R. Taieb, and A. Maquet. In: *Phys. Rev. A* 56 (1997), p. 700.

[6]P. Amaro, J. P. Santos, F. Parente, A. Surzhykov, and P. Indelicato. In: *Phys.Rev. A* 79 (2009), p. 062504.

[7]M. Göppert-Mayer. In: *Ann. d. Phys.* 401 (1931), pp. 273–294.

[8]B. A. Zon and L.I. Rapoport. In: *JETP Lett.* 7 (1968), p. 52.

[9]S.P. Goldman and G.W.F. Drake. In: *Phys. Rev. A* 24 (1981), pp. 183–191.

[10]P. H. Mokler and R. W. Dunford. In: *Physica Scripta* 69 (2004), pp. C1–C9.

[11]R. W. Dunford. In: *Phys. Rev. A* 54 (1996), pp. 3820–3823.

[12]T. Jahrsetz. „The linear Stark perturbation of two-photon decay in hydrogen-like ions“. MA thesis. Physikalisches Institut, University of Heidelberg, 2011.

[13]W. Zernik. In: *Phys. Rev.* 133 (1964), A117–A120.

[14]Y. Heno, A. Maquet, and R. Schwarcz. In: *J. Appl. Phys.* 51 (1980), pp. 11–14.

[15]L. Kissel, R.H. Pratt, and S. C. Roy. In: *Phys. Rev. A* 22 (1980), pp. 1970–2004.

[16]A. Costescu, Jr. P. M. Bergstrom, C. Dinu, and R.H. Pratt. In: *Phys. Rev. A* 50 (1994), pp. 1390–1398.

[17]S. C. Roy, R. H. Pratt, and L. Kissel. In: *Radiat. Phys. Chem.* 41 (1993), pp. 725–738.

[18]A. Costescu, K. Karim, M. Moldovan, S. Spanulescu, and C. Stoica. In: *J. Phys. B: At. Mol. Opt. Phys.* 44 (2011), p. 045204.

[19]L. Safari, P. Amaro, S. Fritzsche, J. P. Santos, and F. Fratini. In: *Phys. Rev. A* 85 (2012), p. 043406.

[20]V. Florescu, M. Marinescu, and R. H. Pratt. In: *Phys. Rev. A* 42 (1990), pp. 3844–3851.

[21]L. Safari, P. Amaro, S. Fritzsche, J. P. Santos, S. Taschenov, and F. Fratini. In: *Phys. Rev. A* 86 (2012), p. 043405.

[22]B. A. Zon, N. L. Manakov, and L. I. Rapoport. In: *Sov. Phys. JETP* 28 (1969), pp. 480–482.

[23]H. R. Sadeghpour and A. Dalgarno. In: *J.Phys.B: At. Mol. Opt. Phys.* 25 (1992), pp. 4801–4809.

[24]Y. Gontier and M. Trahin. In: *Phys. Rev. A* 4 (1971), pp. 1896–1906.

[25]W. M. Saslow and D. L. Mills. In: *Phys. Rev.* 187 (1969), pp. 1025–1034.

[26]V. Chandrasekharan and B. Silvi. In: *J.Phys.B:At.Mol.Opt.Phys.* 14 (1981), pp. 4327–4333.

[27]J. P. Briant, D. Girard, V. O. Kostroun, P. Chevalier, W. Wohrer, and J. P. Mosse. In: *Phys. Rev. Lett.* 46 (1981), pp. 1625–1628.

[28]P. P. Kane. In: *Phys. Rep.* 218 (1992), pp. 67–139.

[29]N. L. Manakov, A. A. Nekipelov, and A. G. Fainshtein. In: *Sov. J. Nucl. Phys.* 45 (1987), p. 677.

[30]B.H. Bransden and C.J. Joachain. *Physics of Atoms and Molecules*. 2nd. Addison-Wesley, 2003.

[31]M.E. Rose. *Relativistic Electron Theory*. Wiley, New York, 1961.

[32]E. Rebhan. *Theoretische Physik II Quantenmechanik, Quantenfeldtheorie, Elementarteilchentheorie, Thermodynamik und Statistik*. Spektrum Akademischer Verlag, 2005.

[33]A.N. Artemyev, V.M. Shabaev, V.A. Yerokhin, G. Plunien, and G. Soff. In: *Phys. Rev. A* 71 (2005), p. 062104.

[34]R.A. Swainson and G.W.F. Drake. In: *J. Phys. A: Math. Gen.* 24 (1991), pp. 79–94.

[35]V.V. Balashov, A.N. Grum-Grzhimailo, and N.M. Kabachnik. *Polarization and Correlation Phenomena in Atomic Collisions*. Kluwer Academic/Plenum Publishers, 2000.

[36]F. Schwabel. *Quantenmechanik(QM1)*. 7th ed. Springer, 2007.

[37]H. W. Kugel and D. E. Murnick. In: *Rep. Prog. Phys.* 40 (1977), pp. 297–343.

[38]O. Postavaru. private communication. 2011.

[39]R. W. Dunford. In: *Phys. Rev. A* 69 (2004), p. 062502.

[40]G.W.F Drake. In: *Nucl. Instrum. Methods B* 9 (1985), pp. 465–470.

[41]A. Surzhykov, U.D. Jentschura, T. Stöhlker, and S. Fritzsche. In: *Eur. Phys. J. D* 46/1 (2008), pp. 27–36.

[42]A. Surzhykov, A. Volotka, F. Fratini, J.P. Santos, P. Indelicato, G. Plunien, Th. Stöhlker, and S. Fritzsche. In: *Phys. Rev. A* 81 (2010), p. 042510.

[43]W. Heitler. *The Quantum Theory of Radiation*. Dover Publ. Inc., 1984.

[44]N.L. Manakov, A.V. Mermianin, and A.F. Starace. In: *J.Phys. B: At. Mol.Opt. Phys.* 35 (2002), pp. 77–91.

[45]D.A. Varshalovich, A.N. Moskalev, and V.K. Khersonskii. *Quantum Theory of Angular Momemtum*. World Scientific Pub. Co., 1988.

[46]M. Abramowitz and I. A. Stegun. *Handbook of Mathematical Functions with Formulas, Graphs, and Mathematical Tables*. 10th printing. Applied Mathematics Series - 55. National Bureau of Standards, 1972.

[47]A. I. Akhiezer and V. B. Beresteskii. *Quantum Electrodynamics*. Interscience publisheres, 1965.

[48]P. J. Mohr. In: *Phys. Rev. Lett.* 40 (1978), pp. 854–856.

[49]M. Hilley and P.J. Mohr. In: *Phys.Rev. A* 21 (1980), pp. 24–33.

[50]H.A. Bethe and E.E. Salpeter. *Quantum Mechanics of One- and Two-Electron Atoms*. Academic Press Inc., 1957.

[51]A. Surzhykov, P. Indelicato, J.P. Santos, P. Amaro, and S. Fritzsche. In: *Phys. Rev. A* 84 (2011), p. 022511.

[52]H. M. Tetchou Nganso and M. G. Kwato Njock. In: *J.Phys. B: At. Mol. opt. Phys.* 40 (2007), pp. 807–836.

[53]V. A. Yerokhin, V. M. Shabaev, T. Beier, and J. Eichler. In: *Phys. Rev. A* 62 (2000), p. 042712.

[54]I. P. Grant. In: *Adv. i. Phys.* 19 (1970), pp. 747–811.

[55]A. Surzhykov, V. A. Yerokhin, T. Jahrsetz, P. Amaro, Th. Stöhlker, and S. Fritzsche. In: *Phys. Rev. A* 88 (2013), p. 062515.

[56]T. Jahrsetz, S. Fritzsche, and A. Surzhykov. In: *Phys. Rev. A* 89 (2014), p. 042501.

[57]W. Zernik. In: *Phys. Rev.* 132 (1963), pp. 320–323.

[58]J. P. Santos, F. Parente, and P. Indelicato. In: *Eur. Phys. J. D* 3/1 (1998), pp. 43–52.

[59]I. M. Savukov and W. R. Johnson. In: *Phys. Rev. A* 66 (2002), p. 062507.

[60]T. Jahrsetz and A. Surzhykov. In: *Physica Scripta* T156 (2013), p. 014069.

[61]R. Szmytkowski. In: *J. Phys. B: At. Mol. Opt. Phys.* 30 (1997), pp. 825–861.

[62]D. J. Hylton and N. J. Snyderman. In: *Phys. Rev. A* 55 (1997), pp. 2651–2661.

[63]I. P. Grant. In: *J. Phys. B: At. Mol. Opt. Phys.* 7 (1974), p. 1458.

[64]J. D. Jackson. *Classical Electrodynamics*. Third Edition. John Wiley and Sons, 1998.

[65]C. D. Lin, W. R. Johnson, and A. Dalgarno. In: *Phys. Rev. A* 15 (1977), pp. 154–161.

[66]S. McConnel, S. Fritzsche, and A. Surzhykov. In: *Comp. Phys. Comm.* 181 (2010), pp. 711–713.

[67]D. Solovyev, V. Sharipov, L. Labzowsky, and G. Plunien. In: *J. Phys. B: At. Mol. Opt. Phys.* 43 (2010), p. 074005.

[68]A. Derevianko and W. R. Johnson. In: *Phys. Rev. A* 56 (1997), pp. 1288–1294.

[69]F. Frattini. „Polarization and correlation phenomena in the two-photon absorbtion of heavy ions“. PhD thesis. Physikalisches Institut, University of Heidelberg, 2011.

[70]V. L. Jacobs and J. Mizuno. In: *J.Phys. B: At. Mol. Opt. Phys.* 5 (1972), pp. 1155–1159.

[71]P. Bräunlich and P. Lambropoulos. In: *Phys. Rev. Lett.* 25 (1970), pp. 135–138.

[72]A. V. Vinogradov and E. A. Yukov. In: *Kvanto. Elektr.* 2 (1973), pp. 105–107.

[73]N. L. Manakov, A. .V. Mermianin, J. P. J. Carney, and R. H. Pratt. In: *Phys. Rev. A* 61 (2000), p. 032711.

[74]S. C. Roy, B. Sarkar, L. D. Kissel, and R. H. Pratt. In: *Phys.Rev. A* 34 (1986), p. 1178.

[75]H. M. Schmid. In: *Astron. Astrophys.* 211 (1989), pp. L31–L34.

[76]C. Szymanowski, V. Veniard, R. Taieb, and A. Maquet. In: *Europhy. Lett.* 37 (1997), p. 391.

Erklärung

Hiermit erkläre ich, dass ich die beigefügte Dissertation selbstständig verfasst und keine anderen als die angegebenen Hilfsmittel genutzt habe. Alle wörtlich oder inhaltlich übernommenen Stellen habe ich als solche gekennzeichnet. Ich versichere außerdem, dass ich die beigefügte Dissertation nur in diesem und keinem anderen Promotionsverfahren eingereicht habe und dass diesem Promotionsverfahren keine Promotionsverfahren vorausgegangen sind.

Heidelberg, 6.10.2014

Dipl.-Phys. Thorsten Jahrsetz